STUDIA UNIVERSITATIS
BABEŞ-BOLYAI

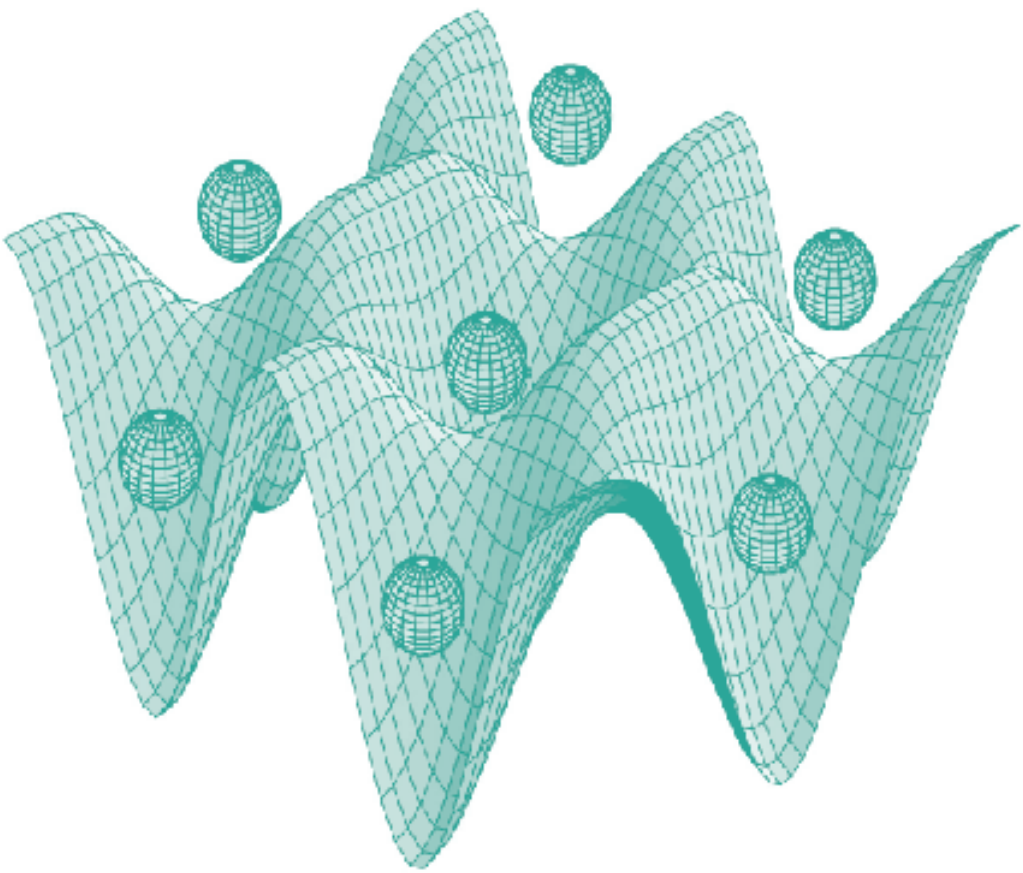

PHYSICA

1/2015

STUDIA
UNIVERSITATIS BABEŞ-BOLYAI
PHYSICA

1/2015

June

EDITORIAL OFFICE OF STUDIA UBB PYSICA:
1, M. Kogălniceanu St., Cluj-Napoca, ROMANIA, Phone: +40 264 405300
http://www.studia.ubbcluj.ro/serii/physica/index_en.html

YEAR **Volume 60 (LX) 2015**
MONTH **JUNE**
ISSUE **1**

S T U D I A
UNIVERSITATIS BABEŞ–BOLYAI

PHYSICA

1

DEDICATED TO
ACADEMICIAN PROFESSOR DR. EMIL BURZO
ON HIS 80TH ANNIVERSARY

STUDIA UBB EDITORIAL OFFICE: B.P. Hasdeu no. 51, 400371 Cluj-Napoca, Romania,
Phone + 40 264 405352

CUPRINS – CONTENT – SOMMAIRE – INHALT

STUDIA UBB PHYSICA, Vol. 60 (LX), 1, 2015, pp. 5-8
(RECOMMENDED CITATION)

ACADEMICIAN PROFESSOR DR. EMIL BURZO ON HIS 80TH ANNIVERSARY

F o r e w o r d

Professor ***Emil Burzo*** was born in 1935, August 30, in Moreni, county Dâmboviţa. He graduated Faculty of Physics from Babeş-Bolyai University Cluj-Napoca in 1959 and in 1958 Faculty of Mechanics from Technical University Cluj-Napoca. Prof. Emil Burzo earned his PhD in Physics at University of Timisoara in 1972, under the guidance of professor A.Cişman and professor P.Lamoth.

Career: engineer at Carbochim plants in Cluj-Napoca (1958-1963); associate engineer and lecturer at Babes-Bolyai University, Cluj-Napoca (1964-1969); Institute of Physics Bucharest (researcher (1969), Senior Researcher III (1971); Senior Researcher II (1978); Senior researcher (1984); Head of Laboratory (1974-1976); Professor at University Babes-Bolyai University (1990 - present), and dean of the Faculty of Physics (1992-2000). Prof. Emil Burzo was Director of the Center of Excellence "Solid State Physics" (certified by MET) and Multi-User Research Base, and PhD superviser in specialities Solid State Physics and Materials Science. As PhD superviser prof. Emil Burzo guided around 40 Ph.D students, including 10 under the co-guardianship with the Universities of Grenoble, Strasbourg and Paris.

Emil Burzo is member of Romanian Academy, and president of the Cluj-Napoca branch of Romanian Academy.

Other professional activities: Associate researcher CNRS-Grenoble, Associate Professor - Carnegie Mellon University, Pittsburgh; Professor cl. I. - J.Fourier Grenoble University. He has presented lectures or invited lessons to over 30 universities in Europe, USA or China. As editor, professor Emil Burzo is responsible for volumes in the field of magnetism, at Publisher Springer Verlag (Germany).

Member in professional organizations: Commission of Physics at the National Council for Attesting Titles, Diplomas and Certificates; Commission of the Romanian National Council of University Research (1997-2003); President of the Romanian Association of Materials Science - ARM; President of the Romanian Society of Magnetic Materials; Member of the Balkan Council of Physics; Chairman of the Section Cluj Romanian Society of Physics (1992-2000); Board Member European Society of Magnetic Materials EMMA (1998 - 2003); member of the Romanian-American Academy, member of the European Physical Society, and the Society of Magnetic Resonance, a member of the Scientific Council ICPE Bucharest (2000), member of the Scientific Council Dubna PAC Solid State Physics.

Scientific activity: Prof. Emil Burzo has a rich scientific activity, with significant original results recognized internationally. The scientific activities of Prof. Emil Burzo were focused on experimental research and modeling of the properties for magnetic and superconducting materials. He elaborated and studied the physical properties of over 150 new alloys systems, intermetallic compounds or superconducting materials and developed models to justify their behavior. These studies led to highlighting the technical applicability of new hard magnetic materials with high specific energy. The results have materialized in the introduction of the Nd-Fe-B and bonded type magnets in manufacturing (in collaboration with ICPE or Sinterom Cluj).

From the large number of original results obtained by Prof. Emil Burzo, we just wish to present the following :

- the developing of a model to justify polarization bands R (5d) considering the presence of both the local exchange interactions 4f-5d and the short-range and 5d 5d-3d-5d;
- justify negative polarization of delocalized states in 3d and 4f compounds cerium and vanadium respectively;
- the contributions of different magnetic interactions wave functions and how the effects of hybridization affect the values of the magnetic moments.
- two models bearing his name;
- the role of electronic concentration of diamagentic matrix in the magnetic behavior of the nickel-based alloys;
- It emphasized that Jaccarino-Walker model used to analyze the magnetic behavior of some solid solutions, appears only as a particular case of a more generally model proposed by prof. Emil Burzo;
- He studied the physical properties of a wide variety of oxide glasses with ions of transition metals 3d and 4f and analyzed valence states of these ions on the matrix composition;
- He emphasized the quasi-amorphous behavior of solid solutions based on V_2O_5 etc.

Prof. Emil Burzo scientific results were published in around 450 papers, 286 in ISI quoted journals (see SCOPUS 2015). He was invited to sustain plenary presentations at many national and international meetings and conferences.

He presented 30 invited lectures at international conferences and that 60 scientific papers published in the proceedings of international conferences. Many scientific articles published are the result of international collaboration with researchers from France, Germany, USA, Netherlands, Austria, Poland, Russia, Moldova, Belgium, Sweden. Acad.prof.univ.dr. Emil Burzo stands by the publication of 21 books or book chapters that have appeared in prestigious foreign publishers (19 books in Springer

Verlag Publishing and one each in North Holland publishing and Institute of Physics, respectively).These are remarkable for their accuracy and scientific level.

Scientific papers and books developed by prof. Emil Burzo are frequently cited in international literature. Thus, according to SCOPUS, quoted in international journals, appearing about **2200** citations.

By understanding the importance of modern directions in material science, Prof. Emil Burzo introduced new courses, related to modern methods in the study of solid state physics. His theoretical and experimental researches, as well as his pedagogic experience were fructified into a series of books focusing on physical properties of solid state. It is distinguished by quality and rigor volumes "Physics of the magnetic phenomena" (3 volumes) and "Permanent magnets" (2 volumes). They are commonly used by students and Romanian researchers.

Awards: Prof. E. Burzo received the Romanian Academy Award, The Excellence Award of Hungarian Academy, Award of Excellence "Opera Omnia" of the Romanian Ministry of Education and Research, Presidential Seal of Honors, USA - MA, Excellence Diploma of Research Institute for Electrical Engineering and several degrees of excellence of the Babes-Bolyai University. He was awarded the National Order "Faithful Service" with the rank of Commander for scientific activity. He was elected to the Institute of Physics Felow (Great Britain). Prof. Emil Burzo is Doctor Honoris Causa of the Universities of Timisoara, Constanta, Technical University of Cluj-Napoca, University Valahia of Targoviste and University Petru Maior of Targu- Mures, etc.

Prof. Emil Burzo is part of the editorial boards of referees for 8 international journals and two national magazines. He is deputy editor for Romanian Journal of Pysics, and section editor for Springer-Verlag Publishing Magnetism Heidelberg - New York.

Today, at the age of 80 years, prof. Emil Burzo can be satisfied that the young researchers supervised by him at the Faculty of Physics, continues his scientific research at the Babes-Bolyai University and in prestigious research institutes from Europe and United States of America and that developed his school of magnetism and established modern research in the field of solid state physics.

Happy Birthday professor Emil Burzo !

Prof.dr. Aurel Pop
Dean - Faculty of Physics

STUDIA UBB PHYSICA, Vol. 60 (LX), 1, 2015, pp. 9-19
(RECOMMENDED CITATION)

Dedicated to Academician Professor Dr. Emil Burzo on His 80th Anniversary

MAGNETIC FLUIDS AND NANOCOMPOSITES: IMPROVING THE MAGNETIC RESPONSE

V. SOCOLIUC[1], R. TURCU[2], D. SUSAN-RESIGA[1], T. BORBÁTH[3], L. VÉKÁS[1*]

ABSTRACT. Magnetic nanofluids, nano-micro composite fluids and polymeric nanocomposites designed for leakage-free rotating magnetofluidic seals and for biomedicine and magnetic separation are reviewed. The synthesis procedures and the magnetic and magnetorheological properties are discussed in terms of achieving the highest volume or mass magnetization of the nanomaterials prepared for specific applications.

Keywords: *magnetic fluids, ferrofluids, magnetic nanocomposites, nano-micro composite fluids, magnetic properties, magnetorheological properties*

INTRODUCTION

Magnetic field control of the motion and positioning of magnetizable fluids (ferrofluids and magnetorheological fluids) and magnetic nanocomposite particles is highly relevant both for engineering and biomedical applications of these nanomaterials [1,2,3]. Magnetic properties, such as volume magnetization of magnetic fluids and mass magnetization or magnetic moment of nanocomposite particles, are determined by the magnetic particle content and are tailored by adequate synthesis procedures [2].

Among the engineering applications, the performances of leakage-free rotating seals with magnetic fluids are fully determined by the magnetic and flow properties of the sealing fluid [4]. The sealed pressure difference is mainly determined by the fluid

[1] *Romanian Academy-Timişoara Branch, Center for Fundamental and Advanced Technical Research, Lab. Magnetic Fluids, 24 M. Viteazu Ave., 300222 Timişoara, Romania*
[2] *National Institute R&D for Isotopic and Molecular Technologies, 67-103 Donat str., 400293 Cluj-Napoca, Romania*
[3] *ROSEAL Co., 5A Nicolae Balcescu str., Odorheiu Secuiesc, Romania*
* *Corresponding author e-mail: vekas@acad-tim.tm.edu.ro, vekas.ladislau@gmail.com*

magnetization and by the highest value of the magnetic induction in the sealing stage. To achieve high magnetization the magnetic content of the ferrofluid has to be increased as much as possible, the saturation magnetization being determined by the volume fraction of magnetic nanoparticles stably dispersed in the carrier liquid. At the same time, the particle volume fraction directly influences the flow properties of the sealing fluid and consequently, the viscous dissipation in the constitutive stages of a rotating seal. The increase of dispersed particle concentration implies an exponential increase of the dynamic viscosity, which limits the saturation magnetization of commercial sealing ferrofluids usually to approx. 600 G [5].

For specific applications in the field of high gradient magnetic separation of biomaterials [6] or in magnetic drug targeting and medical imagistics [7], the nanocomposite particles obtained from magnetic nanoparticle clusters of controlled shape, size, and high magnetic moment in an external magnetic field are of particular interest.

In both kinds of applications, the high magnetic response of the nanomaterials involved is the essential requirement to be considered by the specific synthesis procedures applied. In what follows, some recent results concerning high magnetization sealing fluids and polymeric nanocomposites will be reviewed.

HIGH MAGNETIZATION SEALING FLUIDS

Leakage-free dynamical sealing is among the most important and widely used applications of magnetic fluids [8]. The high vacuum ferrofluidic (FF) rotating seals (FF feedthroughs) and also pressure seals are valuable components of a lot of high-tech equipment [9].

The need to extend the applications to relatively high pressure differences, at the order of tens of bars, requires increasing the saturation magnetization M_s of ferrofluids. In case of magnetite ferrofluids, the upper limit of the solid volume fraction and its influence on the structural and flow properties were discussed in [10]. Transformer oil based magnetic nanofluid samples were prepared applying a previously developed procedure [11,12] involving chemical coprecipitation, followed by steric stabilization of magnetite nanoparticles. The basic procedure was refined and optimized for the synthesis of high concentration magnetic fluids using oleic acid, an unsaturated carboxylic acid, qualified as highly efficient in stabilizing the magnetic nanoparticles in hydrocarbon carriers [13]. Corresponding to the solid volume fraction of 21% the hydrodynamic volume fraction of the most concentrated sample is about 59%, which is close to the maximum random packing fraction of spheres (64%) [10]. This means that practically the upper limit for engineering applications was attained. Indeed, the reduced particle clustering tendency (mean number of particles per cluster estimated to be approx. 1.26) and the dependence of dynamic viscosity on

the magnetic content are still adequate for sealing applications. The dynamic viscosity dependence on the magnetic solid volume fraction (**fig. 1a**) and on the hydrodynamic volume fraction (**fig. 1b**) are well described by the Krieger-Dougherty type function in the operating temperature range of interest for MF seals, up to the highest concentration of surface coated particles close to the maximum random packing. By optimizing the mean particle size (6-7 nm) and the sterical stabilization of nanoparticles by chemisorbed oleic acid monolayer, while eliminating the excess surfactant, the saturation magnetization of ferrofluids attained 1200 G (95 kA/m). The flow properties of transformer oil based ferrofluids show Newtonian behavior up to the highest volume fraction [10] which denotes excellent colloidal stability. This is a basic requirement for rotating seal applications involving long-term stability in strong and very non-uniform magnetic field (B_{max} approx. 1-1.5T; field gradient ~10^9 A/m^2).

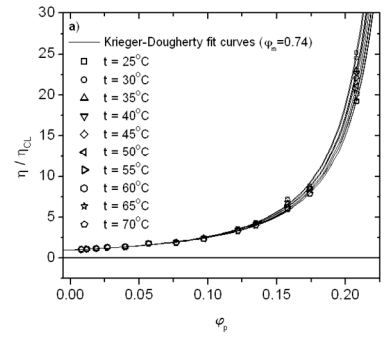

Fig. 1. Composition and temperature dependence of dynamic viscosity
a) solid volume fraction; b) hydrodynamic volume fraction (Reproduced with permission from [10], fig.6; Copyright Elsevier Publ.Co.).

A recent trend to obtain high magnetization ferrofluids involves the synthesis of Co, FeCo and Fe nanoparticles by thermal decomposition of carbonyl precursors in the presence of aluminium organics [14]. Surface coated with Korantin SH (N-oleylsarcosine, AOT (sodium dioctyl sulfosuccinate) or LP4 (fatty acid condensation polymer) after smooth surface oxidation, the procedure yields Co magnetic fluids with very high magnetization (over 1700 G (135 kA/m)) and long-term colloidal stability [14]. The saturation magnetization attained by these Co ferrofluids exceeds with about 35% the magnetization of magnetite ferrofluids discussed above. However, results concerning the behavior of Co ferrofluids in rotating seals are not available.

A possible solution to further increase the saturation magnetization is to consider extremely bidisperse magnetizable fluids, such as ferrofluid based suspensions of carbonyl iron particles of several micrometer sizes [3], i.e. nano-micro composite magnetizable fluids (CMFs). The use of CMFs in rotating seals was thoroughly examined by investigating the magnetic properties [15] and magnetorheological behavior [16,17], the sealing capacity [4,18] and the structural processes [19] involved, depending on the volume fraction of Fe particles dispersed in the concentrated ferrofluid carrier. The behavior of CMFs in non-uniform magnetic field, specific to ferrofluidic rotating seals, was investigated by X-ray microcomputed tomography (XμCT), which allows three-dimensional visualization of microstructures of particles even at a single Fe particle level [19]. In a non-uniform magnetic field the XμCT imaging technique allowed to depict not only the surface deformations of the Rosensweig instability but also the internal Fe particle structures within a nano-micro composite magnetizable fluid spike. This noninvasive technique for the microstructural investigation of magnetizable composite fluid systems evidenced the migration of Fe particles along the gradient of the non-uniform magnetic field, but no particle separation from the FF carrier was observed; this supports the use of CMFs in magnetic fluid rotating seals [4]. In **fig. 2** there are reconstructed tomography images of CMF spikes similar to those first analyzed in [4] (the light yellow–brown colour represents the iron particle and the blue–grey colour shows the magnetic nanofluid carrier liquid), which evidence the migration of Fe particles towards the top of spikes, without separation of the Fe particles from the carrier, which could occur in a conventional magnetorheological fluid.

The saturation magnetization of CMFs shows a linear increase with the volume fraction of Fe particles and attains approx. 700 kA/m for 40% Fe content [17]. However, the use of CMFs in rotating seals is strongly restricted by the orders of magnitude increase of the effective viscosity and yield stress in magnetic field. To exemplify, for sealing applications 10% Fe content gives M_s=2900 G (230 kA/m), improving 2.4 times the sealing capacity corresponding to a high magnetization ferrofluid (1200 G). Higher Fe volume fractions produce significant yield stress increase and pronounced magnetoviscous

effect [17], which limit the use of CMFs to very low rotation speed MF seals. To illustrate the effect of added micrometer size multidomain ferromagnetic (Fe) particles, the dynamic (Bingham) yield stress is plotted versus magnetic flux density in **fig. 3**, for increasing values of the Fe particles volume fraction φ.

Fig. 2. Nano-micro composite fluid (CMF) in non-uniform magnetic field: formation of spikes similar to Rosensweig instabilities in case of ferrofluids

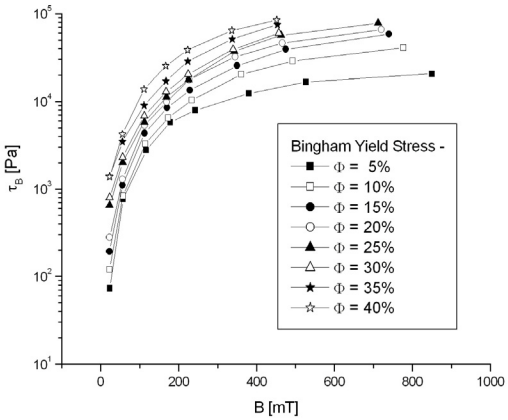

Fig. 3. Bingham yield stress versus magnetic induction-samples with various Fe particle volume fraction φ (using measured data from [17])

For the same set of samples, the magnetoviscous effect (relative increase of effective viscosity) for a moderate shear rate (100 s^{-1}) shows a significant increase due to the added Fe particles (**fig. 4**).

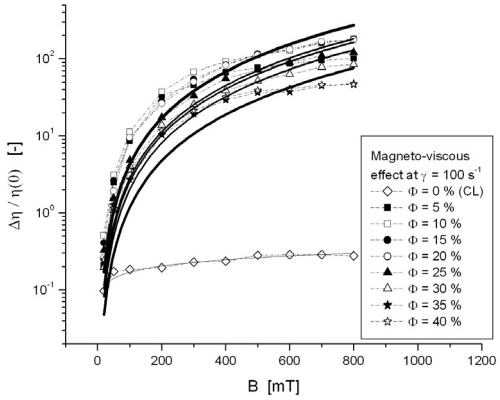

Fig. 4. Magnetoviscous effect for CMFs at 100 s^{-1} shear rate; the influence of Fe volume fraction φ (using measured data from [17])

The measured sealing capacity vs. M_s is given in **fig. 5** for a set of ferrofluids (magnetic nanofluids) and CMFs [4] with increasing saturation magnetization values, the $\Delta p \approx M_s B_{max}$ linear dependence being approximatively respected.

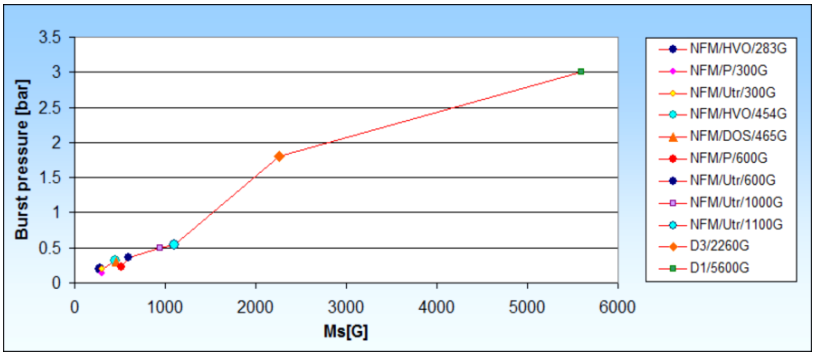

Fig. 5. The burst pressure (sealing capacity) vs. saturation magnetization measured for a single stage MF seal (Ref. [4]).

The very high magnetization nano-micro composite magnetic fluids considerably improve the sealing capacity of MF rotating seals. A 2-3 times increase of the sealed pressure difference may be achieved by using a CMF with moderate (5-15%) volume fraction of Fe particles.

MAGNETIC NANOCOMPOSITES: HIGH MAGNETIZATION CORE-SHELL PARTICLES

A wide variety of synthesis procedures have been reported which exploit the specific composition and property of both the polymeric material and the magnetic nanoparticles used as primary materials, to achieve the required functionalization, morphology and magnetic nanoparticle volume distribution in various types of magnetic beads. Superparamagnetic iron oxide - magnetite and maghemite- nanoparticles are the most used constituents of magnetoresponsive nanosystems-magnetic beads- in the rapidly expanding researches and applications in nanomedicine and biotechnology, including magnetic resonance imaging, magnetic drug delivery systems, magnetic fluid hyperthermia and HGMS separation of cells, proteins and other valuable bio-compounds [6,20,21]. The high magnetic moment of the functionalized carriers is among the most important requirements for successful applications in biomedicine and biotechnology [22,23]. To fulfil this, the optimal localization and amount of magnetic nanoparticles in the magnetic-nonmagnetic material structure, which are essential for the overall magnetic response, favour the magnetic core-organic shell type nanostructures [24]. In the ideal case, densely packed clusters of surface-coated superparamagnetic nanoparticles 5–20 nm in size form the magnetic core of polymeric particles. The requirements for the organic functional shell are determined by the particular application, such as magnetic drug targeting [21,22] or magnetic separation [6]. For both applications the resultant magnetic moment of the core-shell type magnetizable beads in an applied magnetic field is a key property, controlled by the magnetic moment density and the size of particles. Indeed, in the absence of an external magnetic field, the resultant magnetic moment of the nanocomposite particles is zero, while in a nonzero field, the permanent magnetic moments of the constituent nanoparticles align along the field direction, resulting in a net magnetic moment of the particles. Concerning the preparation of magnetic core–polymeric shell-type particles, the ferrofluid-based techniques proved to be efficient, providing a highly reproducible manufacturing procedure [25,26]. This involves controlled clusterization of surface-coated magnetic nanoparticles (MNPs) [27] of a light hydrocarbon based ferrofluid, using the oil-in-water miniemulsion method [28]. The saturation magnetization of these colloidal clusters (NPCs) is dependent on the mean size of the MNPs, packing density and organic (non-magnetic) content. The synthesis procedure for NPCs coated with the surfactants SLS or CTAB is highly reproducible and is suitable for upscaling [28]. The hydrophilic NPCs obtained (**fig. 6**) were further used for encapsulation into polymers. Such densely packed magnetic nanoparticle clusters in polymer shell (**fig. 7**) provided high magnetization spherical particles, promising for both magnetic drug delivery [29] and magnetic separation [30]. The saturation magnetization M_S of NPCs has relatively high values: M_S=63.9 A·m^2/kg for NPCs stabilized with SLS; M_S=76.7 A·m^2/kg for NPCs stabilized with CTAB (**fig. 8**). After polymer coating of NPCs stabilized with

SLS and CTAB, the magnetization of the microgels decrease: M_S=46.8 A·m^2/kg for *M1-pAAc*; M_S=43 A·m^2/kg for *M2-pNIPA-pAAc*; M_S=55 A·m^2/kg for *M3-pAPTAC* (**fig. 8**).

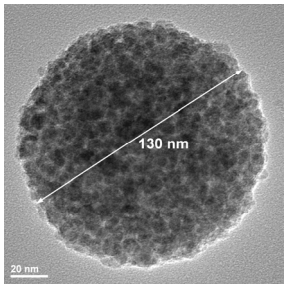

Fig. 6. Magnetic nanoparticle cluster obtained by ferrofluid miniemulsion procedure (reproduced from fig.2, Ref. [30])

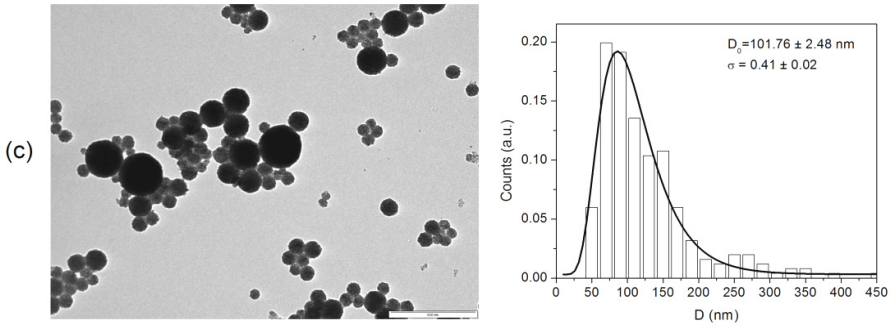

Fig. 7. TEM images of magnetic microgels and their size distributions: sample M3-pAPTAC (reproduced from fig.2, Ref. [30])

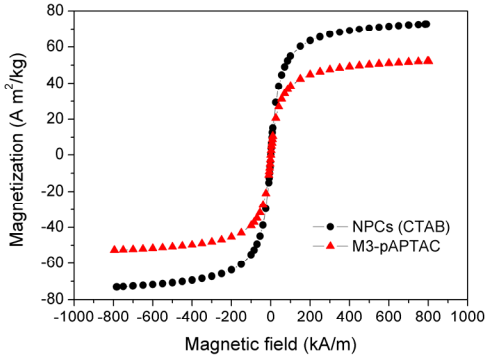

Fig. 8. Magnetization curves for magnetic nanoparticle clusters (NPC) and magnetic microgels (pAPTAC) (reproduced from fig.6, Ref. [30])

Magnetic nanoparticle clusters entrapped into nano-(or micro) gels are promising magnetic carriers in magnetic drug targeting or magnetic separation. The applicability of the aqueous dispersions of magnetic nanocomposite particles depends on their colloidal stability under the influence of various factors like temperature, external magnetic field, concentration and dispersion medium pH. Due to their high induced magnetic moment in applied magnetic field, the magnetic microgel suspensions are susceptible to magnetically induced aggregation [31], a basic process to be considered both in biomedical and biotechnology applications.

CONCLUSIONS

Optimizing the synthesis procedure of magnetite ferrofluids the saturation magnetization of sealing nanofluids attains 100 kA/m. Concentrated ferrofluid based nano-micro composite fluids further increase the saturation magnetization to 700 kA/m, implying also the order of magnitudes increase of the yield stress and magnetoviscous effect of nano-micro composite fluids, which strongly restrict their use for sealing applications. The ferrofluid based mini-emulsion procedure proved to be efficient and reproducible in manufacturing high magnetization hydrophilic nanoclusters (77 emu/g) and polymeric nanocomposites (microgels) (55 emu/g) designed for biomedical and biotechnology applications.

ACKNOWLEDGMENTS

This work was supported by the CCTFA-LLM research program (2012-2015) of the Romanian Academy. The support given in the framework of the projects *MagNanoMicroSeal* (ctr.nr.157/2012) and *HighSpeedNanoMagSeal* (ctr.nr.97/2014) financed by ANCS-UEFISCDI (Romania) is gratefully acknowledged.

REFERENCES

1. S. Odenbach (Ed.), Colloidal Magnetic Fluids. Basics, Development and Application of Ferrofluids, Lecture Notes in Physics 763, Springer, Berlin, Heidelberg, 2009, 430p.
2. L. Vékás, M.V. Avdeev, D. Bica, Magnetic nanofluids: synthesis and structure, in: D. Shi (Ed.), Nanoscience in Biomedicine, Springer, Berlin, Heidelberg, 2009: pp. 650–720.
3. G.Bossis, O.Volkova, S.Lacis, A.Meunier, Magnetorheology: Fluids, Structures and Rheology, in: S. Odenbach (Editor), Ferrofluids: Magnetically controllable fluids and their applications, Lecture Notes in Physics, Springer-Verlag, **594**, 202–232 (2002)

4. T.Borbáth, D.Bica, I.Potencz, I.Borbáth, T.Boros, L.Vékás, Leakage-free Rotating Seal Systems with Magnetic Nanofluids and Magnetic Composite Fluids Designed for Various Applications, *International Journal of Fluid Machinery and Systems* 4 1,67-75(2011)
5. *Liquids Research Co.: http://www.liquidsresearch.com/en-GB/for_sealing_applications-52.aspx*
6. A. Meyer, D.B. Hansen, C.S. Gomes, T.J. Hobley, O.R. Thomas, M. Franzreb, Demonstration of a Strategy for Product Purification by High-Gradient Magnetic Fishing: Recovery of Superoxide Dismutase from Unconditioned Whey, *Biotechnol. Progr*., 21(2005)244-254.
7. K.M. Krishnan, Biomedical nanomagnetics: a spin through possibilities in imaging, diagnostics, and therapy, *IEEE Trans. Magn*. 46 (2010) 2523–2558
8. K.Raj, R.Moskowitz, Commercial applications of ferrofluids, *J.Magn.Magn.Mater*., **85**, 233-245 (1990)
9. K.Raj, B.Moskowitz, R.Casciari, Advances in ferrofluid technology, *J.Magn.Magn.Mater.,* **149**, 174-180 (1995)
10. D.Susan-Resiga, V.Socoliuc, T. Boros, T.Borbáth, O.Marinică, A.Han, L.Vékás, The influence of particle clustering on the rheological properties of highly concentrated magnetic nanofluids, *J. Coll. Interface Sci.,* 373, 110-115 (2012)
11. D.Bica, Preparation of magnetic fluids for various applications, *Romanian Reports in Physics*, **47**(3-5) 265-672 (1995)
12. D.Bica, I.Potencz , L.Vékás, G.Giula, F.Potra, Procedeu de obţinere a unor fluide magnetice pentru etanşări, *Brevet* RO 115533 B1 (2000)
13. R.Tadmor, R.E.Rosensweig, J.Frey, J.Klein, Resolving the puzzle of ferrofluid dispersants, *Langmuir*, **16**, 9117-9120 (2000)
14. S.Behrens, H.Bönnemann, N.Matoussevitch, H.Modrow, V.Kempter, W.Riehemann, A.Wiedenmann, S.Odenbach, S.Will, D.Eberbeck, R.Hergt, R.Müller, K.Landfester, A.Schmidt, D.Schüler, R.Hempelmann, Synthesis and Characterization, in: Odenbach S., (Ed.) Colloidal Magnetic Fluids. Basic, Development and Application of Ferrofluids, Lecture Notes in Physics **763** (Springer Verlag, Berlin Heidelberg) pp.1 – 82 (2009)
15. T. Borbáth, PhD Thesis, UP Bucharest, 2012
16. D.Susan-Resiga, D.Bica, L.Vékás, Flow behaviour of extremely bidisperse magnetizable fluid, *J.Magn.Magn.Mater*., **322**, 3166-3172 (2010)
17. D.Susan-Resiga, L.Vékás, Yield stress and flow behavior of concentrated ferrofluid-based magnetorheological fluids: the influence of composition, *Rheol Acta*, 53,645–653(2014)
18. I.Borbáth, Z.Kacsó, L.Dávid, I.Potencz, D.Bica, O.Marinică, L.Vékás, Applications of magnetic nanofluids in rotating seals, în: Convergence of micro-nano-biotechnologies, Series Micro- and Nanoengineering, Romanian Academy Publ. House, Bucharest, 200-215 (2006)
19. T Borbáth, I Borbáth, S Günther, O Marinica, L Vékás, S Odenbach, Three-dimensional microstructural investigation of high magnetization nano–micro composite fluids using x-ray microcomputed tomography, *Smart Mater. Struct*. 23 (2014) 055018 (10pp)
20. L.H. Reddy, J.L. Arias, J. Nicolas, P. Couvreur, Magnetic nanoparticles: Design and Characterization, toxicity and biocompatibility, pharmaceutical and biomedical applications, *Chem. Rev*. 112 (2012) 5818–5878.

21. M. Colombo, S. Carregal-Romero, M.F. Casula, L. Gutiérrez, M.P. Morales, I.B. Böhm, J.T. Heverhagen, D. Prosperi, W.J. Parak, Biological applications of magnetic nanoparticles, *Chem. Soc. Rev*. 41 (2012) 4306–4334
22. S. Dürr, C. Janko, S. Lyer, P. Tripal, M. Schwarz, Z. Jan, R. Tietze, C. Alexiou, Magnetic Nanoparticles for Cancer Therapy, *Nanotechnol Rev*. 2 (2013) 395–409
23. S. Laurent, A.A. Saei, S. Behzadi, A. Panahifar, M. Mahmoudi, Superparamagnetic iron oxide nanoparticles for delivery of therapeutic agents: opportunities and challenges., Expert Opin. *Drug Deliv*. 11 (2014) 1–22
24. M. Laurenti, P. Guardia, R. Contreras-Cáceres, J. Pérez-Juste, A. Fernandez-Barbero, E. Lopez-Cabarcos, J. Rubio-Retama, Synthesis of thermosensitive microgels with a tunable magnetic core, *Langmuir*. 27 (2011) 10484–10491
25. P. Qiu, C. Jensen, N. Charity, R. Towner, C. Mao, Oil phase evaporation-induced self-assembly of hydrophobic nanoparticles into spherical clusters with controlled surface chemistry in an oil-in-water dispersion and comparison of behaviors of individual and clustered iron oxide nanoparticles*, J. Am. Chem. Soc.* 132 (2010) 17724–17732
26. V. Lobaz, R.N. Klupp Taylor, W. Peukert, Highly magnetizable superparamagnetic colloidal aggregates with narrowed size distribution from ferrofluid emulsion, *J. Colloid Interface Sci.* 374 (2012) 102–110
27. V. Socoliuc, L. Vekas, Hydrophobic and hydrophilic magnetite nanoparticles: synthesis by chemical coprecipitation and physico-chemical characterization, in: H. Nirschl, K. Keller (Eds), Upscaling of bio-nano-processes, Springer (2014) pp.39-56
28. R. Turcu, I. Craciunescu, A. Nan, Magnetic microgels: synthesis and characterization, in: H. Nirschl, K. Keller (Eds), Upscaling of bio-nano-processes, Springer (2014) pp.57-76
29. R. Turcu, I. Craciunescu, V.M. Garamus, C. Janko, S. Lyer, R. Tietze, C. Alexiou, L. Vékás, Magnetic microgels for drug targeting applications: Physical–chemical properties and cytotoxicity evaluation, *J. Magn. Magn. Mater.* 380 (2015) 307–314
30. R. Turcu, V. Socoliuc, I. Craciunescu, A. Petran, A. Paulus, M. Franzreb, E. Vasile, L. Vékás, Magnetic microgels, a promising candidate for enhanced magnetic adsorbent particles in bioseparation: synthesis, physicochemical characterization, and separation performance, *Soft Matter.* 11 (2015) 1008–1018
31. V. Socoliuc, L. Vékás, R. Turcu, Magnetically induced phase condensation in an aqueous dispersion of magnetic nanogels, *Soft Matter*. 9 (2013) 3098–3105.

STUDIA UBB PHYSICA, Vol. 60 (LX), 1, 2015, pp. 21-30
(RECOMMENDED CITATION)

Dedicated to Academician Professor Dr. Emil Burzo on His 80th Anniversary

STRUCTURAL, MAGNETIC AND ELECTRONIC PROPERTIES OF THE INTERMETALLIC COMPOUNDS FROM THE TERNARY SYSTEM Ce – Co – Mn

R. DUDRIC[1], A. POPESCU[1], O. ISNARD[2], M. NEUMANN[3], V. POP[1*], M. COLDEA[1]

ABSTRACT. XRD, magnetic and XPS measurements of the three classes of intermetallic compounds with different crystallographic structures are reported. XPS spectra of $Ce_2Co_{15}Mn_3$, $CeCo_7Mn_5$ and $CeCo_8Mn_4$ compounds pointed out the intermediate valence state of Ce atoms and that both Co and Mn atoms carry magnetic moments. The complex magnetic structure is determined by the competition between the ferromagnetic (Co–Co pairs) and antiferromagnetic (Co–Mn and Mn–Mn pairs) interactions. In CeCoMn, $Ce_3Co_3Mn_4$ and Ce_3Co_6Mn compounds both Ce and Co atoms are non-magnetic like in the isostructural compound $CeCo_2$. Magnetic behavior is mostly due to the Mn moments and depends essentially on the Mn - Mn distances.

Keywords: *Mn-Co-Ce intermetallics, XPS, local moments, intermediate valence*

INTRODUCTION

The problem of local moments confined to the transition metals (T) sites, i.e., localized behavior in some aspects of itinerant electrons, is one of the most important issues in the physics of the magnetic alloys and intermetallic compounds [1–3]. The electronic 3d band of the transition metals is determined by the overlap between the d orbitals of adjacent atoms and depends on the number of nearest-

[1] *Babes-Bolyai University, Faculty of Physics, 400084 Cluj-Napoca, Romania*
[2] *Institut Néel du CNRS, Université J. Fourier, 38042 Grenoble Cedex 9, France*
[3] *Universität Osnabrück, Fachbereich Physik, 49069 Osnabrück, Germany*
* *Corresponding author e-mail: viorel.pop@phys.ubbcluj.ro*

neighbors and on the hopping integral, which is very sensitive to the T–T distances [4]. The Mn-based alloys and compounds are assumed to exhibit a strong dependence of Mn-Mn exchange interaction as a function of distance between the nearest neighbor Mn atoms. It is well known that the Mn-Mn interaction is antiferromagnetic when the distance d_{Mn-Mn} is smaller than 2.8 Å [5].

On the other hand, in a large number of intermetallic compounds based on Ce and 3d-transition elements was observed a variety of anomalous behaviors in the lattice constants and magnetic properties due to the intermediate valence state of Ce ions [6–11]. Furthermore, the reported experimental data have shown the $CeCo_2$ compound is an exchange-enhanced Pauli paramagnet with a spin fluctuation temperature T_{sf} higher than room temperature and this is consistent with the almost temperature independent magnetic susceptibility below room temperature, indicating that in this compound both Ce and Co atoms are non-magnetic. [12-14].

In the ternary metallic system Ce–Co–Mn, many intermetallic compounds with different crystallographic structures are reported [15]. The aim of this paper is to study the magnetic state of Ce, Co and Mn atoms, the nature and the intensity of the magnetic interactions in the six compounds from this intermetallic system and how these interactions depend on the number of magnetic ions in the unit cell by correlating the results obtained from XRD data, magnetic measurements and XPS spectra. Results on the individual classes of these compounds were published elsewhere [16-18]

EXPERIMENTAL

The intermetallic compounds $Ce_2Co_{15}Mn_3$, $CeCo_8Mn_4$, $CeCo_7Mn_5$, CeCoMn, $Ce_3Co_3Mn_4$ and Ce_3Co_6Mn were prepared in a cold crucible induction furnace under a purified argon atmosphere. The samples were melted repeatedly in the same atmosphere to ensure homogeneity. The purity of the starting materials was 99.9% for all the constituent elements. The crystalline structure of the samples was analyzed at room temperature by using a D 5000 Brücker Bragg-Brentano diffractometer with Cu Ka radiation. The XPS spectra were recorded using a PHI 5600ci ESCA spectrometer with monochromatized Al Ka radiation at room temperature. The magnetic measurements were performed in the temperature range 4 - 550 K and in magnetic field up to 12 T using a vibrating sample magnetometer or by extraction method.

RESULTS AND DISCUSSION

X-Ray diffraction (XRD) measurements showed that all the investigated compounds are single phases. The crystalline structure and the lattice parameters are as follows: $Ce_2Co_{15}Mn_3$ - Th_2Zn_{17} structure type, a = 8.410 Å, c = 12.328 Å, $CeCo_7Mn_5$

and $CeCo_8Mn_4$ - the $ThMn_{12}$ structure type, a = 8.496 Å, c = 4.748 Å and a= 8.464 Å, c = 4.743 Å, respectively and CeCoMn, $Ce_3Co_3Mn_4$ (or $CeCoMn_{1.33}$) and Ce_3Co_6Mn (or $CeCo_2Mn_{0.33}$) - the $MgCu_2$ structure type, a = 7.30 Å, a= 7.33 Å and a= 7.16 Å, respectively, the last three compounds being isostructural with the parent compound $CeCo_2$ with lattice parameter a = 7.16 Å. By the Rietveld refinement one took into account that the atomic sites with a larger Wigner Seitz volume are expected to be preferentially occupied by Mn atoms, since the atomic radius of Mn atoms is larger than that of Co atoms (1.307 Å and 1.252 Å, respectively). For example, the 18h and 6c sites in $Ce_2Co_{15}Mn_3$ and the 8i sites in $CeCo_7Mn_5$ and $CeCo_8Mn_4$ are occupied by the Mn atoms. The majority of the distances $d_{Co\text{-}Co}$ between Co atoms in all analyzed compounds are very close to those between the Co atoms in pure Co metal, namely 2.50 Å. It is to note that in all compounds, except the compound $CeCo_2Mn_{0.33}$, there are positions occupied by Mn atoms for which the distance $d_{Mn\text{-}Mn}$ is smaller that 2.8 Å.

The XPS spectra of the Ce 4d core levels reflect the intermediate valence in $Ce_2Co_{15}Mn_3$, $CeCo_8Mn_4$ and $CeCo_7Mn_5$ compounds. In Fig. 1, the Ce 4d spectrum of $CeCo_8Mn_4$ shows the multiplets arising from the interaction of the 4d hole with the 4f electrons, which are characteristic for all compounds with Ce in the trivalent states (the peaks corresponding to Ce^{3+} are superimposed on the Co 3s peaks at 108.4 and 111.47 eV), and two new peaks at binding energies 118.56 and 122.04 eV. Similar spectrum was observed in $CeCo_7Mn_5$ and $Ce_2Co_{15}Mn_3$ compounds. The last two peaks correspond to the fraction of tetravalent Ce in these three compounds. The spin-orbit splittings are about 3.4 eV for Ce^{3+} and 3.1 for Ce^{4+} in good agreement with the values measured in $CeNi_5$ [6], CeF_4 [7], $CeMn_4Al_8$ and $CeMn_6Al_6$ [19] intermediate valence compounds.

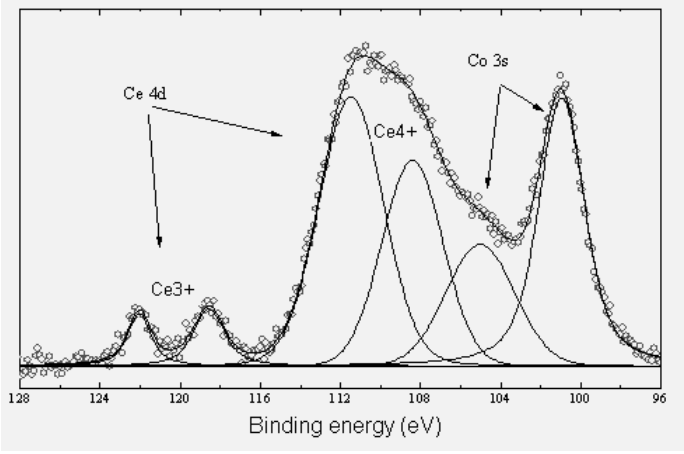

Fig. 1. XPS spectrum of the Ce 4d and Co 3s core levels in $CeCo_8Mn_4$

The exchange interaction J_{dc} between the core hole spin *s* and the 3d electron spin *S* gives rise to a satellite on the high binding energy side of the main line of the Co 3s spectrum [20]. The Co 3s core level spectrum shows an exchange splitting of about 4.2 eV (Fig. 1), which is a direct evidence of the local magnetic moments on Co sites. This value is close to that found in the pure Co metal, namely 4.5 eV [21]. The exchange splitting $\Delta_{ex} = J_{dc}(2S + 1)$ is proportional with the Co local moment $\mu_{Co} = 2S$ [22]. This result suggests that the Co local moment decreases only slightly when going from Co metal to $Ce_2Co_{15}Mn_3$, $CeCo_7Mn_5$ and $CeCo_8Mn_4$.

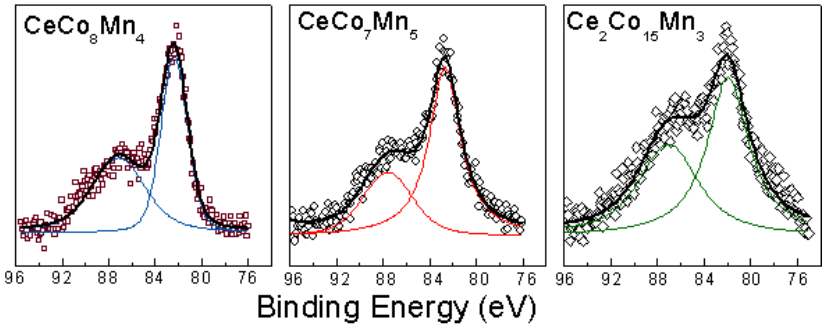

Fig. 2. XPS spectra of Mn 3s in $CeCo_7Mn_5$, $CeCo_8Mn_4$ and $Ce_2Co_{15}Mn_3$

Fig. 2 presents the curve fitting results of Mn 3s spectrum in the $CeCo_8Mn_4$, $CeCo_7Mn_5$ and $Ce_2Co_{15}Mn_3$ compounds, after background subtraction. The Mn 3s core level spectrum shows an exchange splitting around 4.9 eV. Such splittings of about (4–5) eV were observed in the 3s levels of Mn atoms in various intermetallic compounds and alloys, like $Mn_{1-x}Ni_xAl$ [19], $CeMn_4Al_8$ and $CeMn_6Al_6$ [28], $MnPd_{1-x}Sb_x$ [24]. For example, the exchange splitting in MnNi is about 5.2 eV and the Mn magnetic moment is 4 μ_B/Mn[25]. The values obtained for Mn 3s exchange splittings in $Ce_2Co_{15}Mn_3$, $CeCo_8Mn_4$ and $CeCo_7Mn_5$ compounds indicate a mean local magnetic moment per Mn atom of about 3.2 μ_B.

Magnetic field dependences of magnetization at T = 4 and 300 K of $Ce_2Co_{15}Mn_3$ compound are shown in Fig. 3. The saturation magnetizations M_S determined from the extrapolation of magnetization to the zero field are 22.67 μ_B/f.u. at T = 4 K and 18.41 μ_B/f.u. at T = 300 K. The magnetization as a function of temperature for $Ce_2Co_{15}Mn_3$ is shown in the inset of Fig.3.

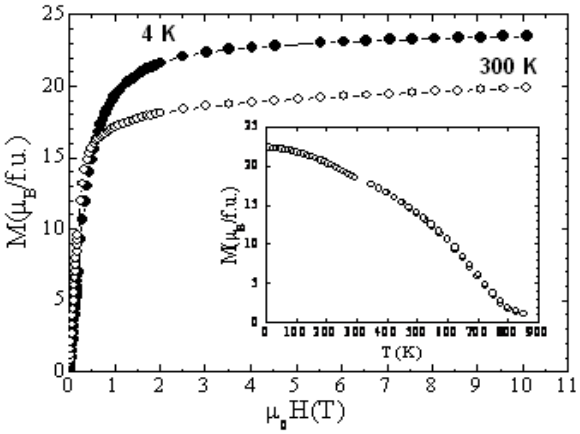

Fig. 3. Magnetization curves of $Ce_2Co_{15}Mn_3$ at 4 and 300 K in magnetic fields up to 10 T. In the inset is shown de temperature dependence of the magnetization

The Curie temperature T_C of $Ce_2Co_{15}Mn_3$ is determined to be 740 K from the temperature dependence of M^2 (T) according to the mean field approach. This value is smaller than the Curie temperature T_C = 772 K found in $Ce_2Co_{15}Mn_2$ compound, which crystallizes in the Th_2Ni_{17} structure type [26]. The values and variations of magnetization of $Ce_2Co_{15}Mn_3$ with field and temperature suggest that this compound has a ferromagnetic behavior below the Curie temperature T_C. The coupling between the Co atoms from different sites is ferromagnetic as usual for Co containing intermetallic, while between the Co and Mn atoms can be expected to be antiferromagnetic. Since the distances between the 18f sites $d_{18f–18f}$ (sites partially occupied by the Mn atoms) in $Ce_2Co_{15}Mn_3$ are smaller than this critical distance, there are some antiferromagnetic Mn–Mn pairs, like in many others Mn based alloys and intermetallic compounds [23, 27]. The antiferromagnetic interactions lead to a decrease of the Curie temperature and of the saturation magnetization per unit formula of $Ce_2Co_{15}Mn_3$ in comparison with values found in Ce_2Co_{17} compound (T_C = 1100 K and M_S = 26.1 μ_B/f.u.) [26]. The competition between these three kinds of interaction Co– Co (the dominant one), Co–Mn and Mn–Mn is expected to lead to a non parallel arrangement of the Mn moments relative to Co moments, which explains the obtained value for the saturation magnetization in $Ce_2Co_{15}Mn_3$.

Although the XPS spectra indicate similar electronic structure of Co and Mn atoms in $CeCo_7Mn_5$ and $CeCo_8Mn_4$, which suggests close values of the local magnetic moments per Co and respectively Mn atoms, the difference in the number of Co and Mn atoms per unit formula leads to very different values of magnetization as a function of magnetic field and temperature.

The magnetic field dependences of magnetizations recorded for temperatures between 5 K and 300 K for $CeCo_7Mn_5$ and $CeCo_8Mn_4$ (in the inset) are shown in Fig. 4 and their temperature dependences in Fig. 5. The values and the variations of magnetizations with field suggest an antiferromagnetic coupling between the transition metal moments located on different sublattices. The dM/dT curve for $CeCo_7Mn_5$ exhibits one local minimum near $T_C \cong 45$ K, ascribed to the ferromagnetic Co - Co coupling and a local maximum near $T_N \cong 150$ K, which can be ascribed to the antiferromagnetic Mn - Mn coupling. The magnetization of $CeCo_8Mn_4$ does not reach saturation even at high fields, but the values of spontaneous magnetization M_{sp} are much higher than those of $CeCo_7Mn_5$. As an example, at 4 K, M_{sp} = 2.6 μ_B/f.u for $CeCo_8Mn_4$, in comparison with M_{sp} = 0.7 μ_B/f.u for $CeCo_7Mn_5$. The dM/dT curve for $CeCo_8Mn_4$, shown in the inset of Fig. 5, exhibits one local maximum near $T_N \cong 100$ K and one local minimum near $T_C \cong 173$ K, ascribed like for $CeCo_7Mn_5$ to the antiferromagnetic and ferromagnetic ordering of the 3d magnetic moments. The magnetic susceptibilities for $CeCo_7Mn_5$ and $CeCo_8Mn_4$, measured in the temperature range 300 - 550 K, fit a Curie - Weiss law plus a small additional temperature - independent term with the parameters given in Table 1. From the correlation of the total Curie constants for the two compounds $C = C_{Co} + C_{Mn}$ results the effective magnetic moments per Co and Mn atoms and the values are given in Table 1.

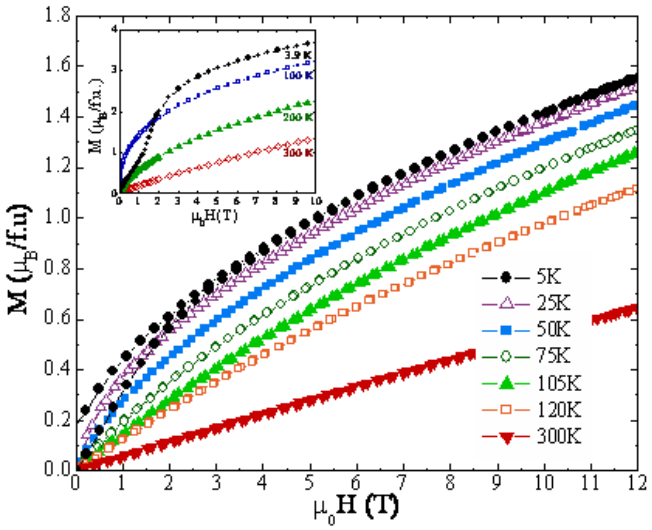

Fig. 4. Magnetization curves of $CeCo_7Mn_5$ and $CeCo_8Mn_4$ (inset) for temperatures between 4 K and 300 K in magnetic field up to 12 T.

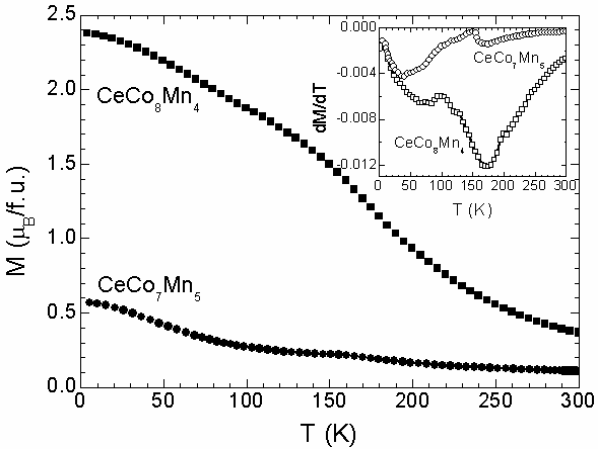

Fig. 5. Temperature dependence of magnetizations for $CeCo_8Mn_4$ and $CeCo_7Mn_5$ in 2 T magnetic field. The inset shows the dM/dT curves.

Table. 1. Magnetic characteristics of the intermetallic compounds from the ternary system Ce-Co-Mn.

Compound	T_C (K)	T_N (K)	μ_{Co} (μ_B)	μ_{Mn} (μ_B)	μ_{eff}^{Co} (μ_B)	μ_{eff}^{Mn} (μ_B)	θ (K)
$Ce_2Co_{15}Mn_3$	740	-	≅1.5	≅ 3.2			
$CeCo_8Mn_4$	173	100	1.6	3.2	2.4	4.08	240
$CeCo_7Mn_5$	45	150	1.6	3.2	2.4	4.08	-175
CeCoMn	-	44	-		-	3.12	-122.1
$CeCoMn_{1.33}$	-	44	-		-	3.22	-183.3
$CeCo_2Mn_{0.33}$	-	-	-	-	-	4.1	-1

Fig. 6 shows the temperature dependence of magnetization for CeCoMn and $CeCoMn_{1.33}$ compounds measured in an applied magnetic fields of 1T and 2T. The M(T) curves exhibit a maximum around 44 K and 35 K, respectively, revealing the antiferromagnetic behavior of the two compounds. Since the Ce and Co atoms do not carry any ordered magnetic moment, like in $CeCo_2$, the magnetic behavior of these alloys is due to the interactions between the Mn local moments. The nearest neighbor Mn-Mn distance between Mn atoms in both alloys is about 2.6 Å, smaller than the critical value, what explains the antiferromagnetic interaction between the neighboring Mn atoms. The upturn of the M(T) curves at lower temperatures is due to traces of magnetic impurities. In contrast with the CeCoMn and $CeCoMn_{1.33}$ compounds, M (T) for $CeCo_2Mn_{0.33}$ reveals the paramagnetic behavior of this compound in the temperature range 5 K - 300 K. The magnetic susceptibility of CeCoMn and

$CeCoMn_{1.}33$ compounds for T> 100 K and of $CeCo_2Mn_{0.33}$ in the measured temperature range may be described with a Curie - Weiss law plus an additional temperature - independent term χ_o, as one can see from the inset of Fig .6, where $1/(\chi - \chi_o)$ is plotted as a function of the temperature. The values of the effective magnetic moments of Mn atoms and of the paramagnetic Curie temperatures are listed in Table 1. The value of the paramagnetic Curie temperature suggests that the interaction between the Mn local magnetic moments in $CeCo_2Mn_{0.33}$ is negligible. This was to be expected due to a larger distance between the Mn moments in comparison with that found in the other two compounds CeCoMn and $CeCoMn_{1.33}$, which are much richer in Mn. In the case of $CeCo_2Mn_{0.33}$ alloy, the Mn atoms are diluted in the $CeCo_2$ matrix and consequently are only expected to be found as second near neighbors.

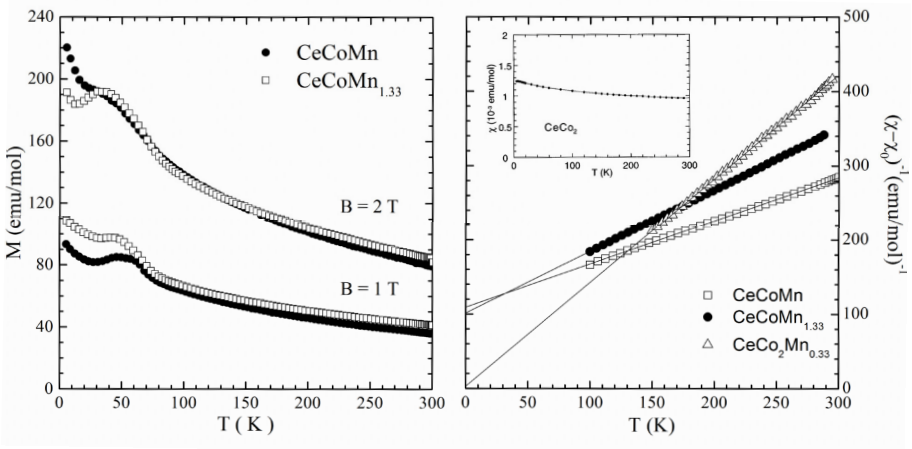

Fig. 6. Temperature dependence of the magnetization for CeCoMn and $CeCoMn_{1.}33$ and the temperature dependence of the reciprocal susceptibilities for CeCoMn, $CeCoMn_{1.}33$ and $CoCo_2Mn_{0.33}$. In the inset is shown the temperature dependence of $CeCo_2$ susceptibility.

CONCLUSIONS

XPS spectra of $Ce_2Co_{15}Mn_3$, $CeCo_7Mn_5$ and $CeCo_8Mn_4$ compounds pointed out the intermediate valence state of Ce ions and that both Co and Mn atoms carry magnetic moments. The complex magnetic structure of these three compounds is determined by the competition between the ferromagnetic (Co-Co pairs) and antiferromagnetic (Co-Mn and Mn-Mn pairs) interactions. The substitution of Co by Mn atoms leads to the decrease of the ferromagnetic interactions and to the increase of the antiferromagnetic interactions.

Both Ce and Co atoms are non-magnetic in CeCoMn, $Ce_3Co_3Mn_4$ and Ce_3Co_6Mn like in the isostructural parent compound $CeCo_2$. Magnetic behavior of these three compounds is mostly due to the Mn moments and depends essentially on the Mn - Mn distances. The interaction between the Mn moments is antiferromagnetic in CeCoMn and $Ce_3Co_3Mn_4$, but a paramagnetic behavior for Ce_3Co_6Mn was evidenced in the studied temperature range.

ACKNOWLEDGMENTS

This work was supported by the Romanian Ministry of Education and research – UEFISCDI Project No. PN- II-ID-PCE-2012-4-0470

REFERENCES

[1] P.W. Anderson, *Phys. Rev*., 124, 41 (1961).
[2] V.Yu. Irkhin, M.I. Katsnelson, A.V. Trefilov*, J. Phys.: Cond. Matter* 5, 8763 (1993).
[3] J. Kübler, Theory of Itinerant Electron Magnetism, Oxford Sciences Publications, 2000.
[4] J. Mathon, *Contemp. Phys*., 32, 143 (1991).
[5] A. Kjekshus, R. Mollebud, A.F. Andresen, W.B. Pearson, *Phil. Mag.*, 16, 1063 (1967).
[6] J.C. Fuggle, F.U. Hillebrecht, Z. Zolnierek, R. Läser, Ch. Freiburg, O. Gunnarsson, K. Schönhammer, *Phys. Rev. B,* 27, 7330 (1983).
[7] Y. Baer, Ch. Zürcher, *Phys. Rev. Lett*., 39, 956 (1977).
[8] J. Röhler, X-ray absorption and emission spectra, in: K.A. Gschneidner, J.R.Eyring, S. Hüfner (Eds.), Handbook on the Physics and Chemistry of Rare Earths, North-Holland, Amsterdam, 1987, pp. 453.
[9] O. Isnard, S. Miraglia, D. Fruchart, C. Georgetti, S. Pizzini, E. Dartyge, J.P.Kappler, G. Krill, *Phys. Rev. B*, 49, 15692 (1994).
[10] O. Isnard, S. Miraglia, D. Fruchart, C. Giorgetti, E. Dartyge, G. Krill, *J. Phys.: Condens*. *Matter* 8, 2437 (1996).
[11] R.D. Parks, S. Raaen, M.L. denBoer, V. Murgai, T. Mihalisin, *Phys. Rev. B*, 28, 3556 (1983).
[12] Y. Aoki, T. Nishigaki, H. Sugawara, H. Sato, *Phys. Rev. B*, 55, 2768l (1997).
[13] A. S. Panfilov, G. E. Grechnev, I. V. Svechkarev, H. Sugawara, H. Sato, O. Eriksson, *Physica B*, 319, 268 (2002).
[14] T. M. Seixas, J. M. Machado da Silva, *Physica B,* 269, 362 (1999).
[15] P. Vilars, L.D. Calvert, in: Pearson's Handbook of Crystallographic Data for Intermetallic Phases, second ed., ASM International, Materials Park, OH, 1991.
[16] A. Popescu, O. Isnard, R. Dudric, M. Coldea, J. *Alloys Compd*., 535, 10 (2012).
[17] R. Dudric, A. Popescu, O. Isnard, M. Coldea, *Intermetallics*, 38, 150 (2013).
[18] R. Dudric, A. Popescu, O. Isnard, V. Pop, M. Coldea, *Acta Phys. Pol.,* 2015 (in press).

[19] M. Coldea, M. Neumann, St. Lütkehoff, S. Mähl, R. Coldea, *J. Alloys Compd.,* 278, 72 (1998).
[20] S. Hüfner, Photoelectron Spectroscopy Principles and Applications, Springer Verlag, Berlin, 1995.
[21] P.D. Johnson, Y. Liu, Z. Xu, D.J. Huang, J. Electron. *Spectrosc. Relat. Phenom*., 75, 245 (1995).
[22] G. Garreau, V. Schorsch, E. Beaurepaire, J.C. Parlebas, O. Speder, P. Rennert, *J. Phys. IV Colloque* C9. 4, 127 (1994).
[23] V. Rednic, M. Coldea, S.K. Mendiratta, M. Valente, V. Pop, M. Neumann, L. Rednic, *J. Magn. Magn. Mat.,* 321 3415 (2009).
[24] R. Pacurariu, M. Coldea, M. Neumann, V. Pop, O. Isnard, M. Räkers, *Phys. Stat. Sol., B* 244, 3190 (2007).
[25] L. Pál, E. Krén, G. Kádár, P. Szabó, T. Tarnóczi, *J. Appl. Phys*., 39 538 (1968).
[26] Zhi-gang Sun, Hong-wei Zhang, Bing Liang, Jing-yun Wang, Bao-gen Shen, *J. Appl. Phys.,* 87, 5311 (2000).
[27] V. Rednic, L. Rednic, M. Coldea, V. Pop, M. Neumann, R. Pacurariu, A.R. Tunyagi, *Cent. Eur. J. Phys.*, 6, 434 (2008).

STUDIA UBB PHYSICA, Vol. 60 (LX), 1, 2015, pp. 31-44
(RECOMMENDED CITATION)

Dedicated to Academician Professor Dr. Emil Burzo on His 80th Anniversary

CONCENTRATION AND PUMP INTENSITY EFFECTS IN THE EMISSION OF Nd LASER MATERIALS

V. LUPEI[1*], A. LUPEI[1]

ABSTRACT. High doping concentrations useful for granting efficient absorption of the pump radiation can be hampered by the concentration-dependent self-quenching of emission due to energy transfer inside the system of doping ions. The paper discusses the pump intensity-dependent balance between the down- and upconversion processes in the Nd laser materials, based on their effect on emission dynamics. Reduction of emission quantum efficiency by self-quenching and its influence on the laser emission and heat generation is analysed.

Keywords**:** *Nd lasers, energy transfer, down-conversion, upconversion, heat generation*

INTRODUCTION

The non-radiative de-excitation of the emitting level in the pumped laser materials is major factor in limitation of the performances of the solid-state lasers. Basically there are two major mechanisms, the electron-phonon (EP) interaction that transforms the excitation into heat and the non-radiative energy transfer ET to another ion. The final levels of the donor D ion and of the acceptor A ion involved in this process could de-excite further by EP interaction and then the joint action of ET and EP interaction contributes to heat generation. The non-radiative processes accelerate the dynamics of emission of the excited level and the competition of radiative de-excitation with the non-radiative processes, is characterized by the emission quantum efficiency η_{qe}. The efficiency of the ET processes depends on their nature, which defines a microparameter of transfer and on the concentration of acceptors.

[1] *National Institute of Laser, Plasma and Radiation Physics, 077125 Bucharest, Romania*
* *Corresponding author e-mail: lupei_voicu@yahoo.com*

Of major relevance for the laser ions are the ET processes inside the system of doping ions since these could determine the selfquenching of emission. In case of Nd^{3+} the self-quenching could involve both down-conversion (DC) cross-relaxation ($^4F_{3/2}$, $^4I_{9/2}$) → ($^4I_{15/2}$, $^4I_{15/2}$) and several upconversion (UPC) processes, ($^4F_{3/2}$, $^4I_{9/2}$) → ($^4I_{13/2}$, $^4G_{7/2}$) or/and ($^4I_{11/2}$, $^4G_{9/2}$) or/and ($^4I_{9/2}$, $^2P_{1/2}$). In many Nd laser materials, including $Y_3Al_5O_{12}$ (YAG) the richer variety of processes and the better matching of D emission with the A absorption could determine larger ET microparameter for UPC than that for DC. The final D and A state $^4I_{15/2}$ for down-conversion is de-excited rapidly by fast EP relaxation along the ladder of ^4I_J levels to the ground level $^4I_9$ and thus the whole excitation involved in process is finally transformed into heat. However, in case of UPC the EP interaction relaxes the final state of the donor to the ground state and that of the acceptor back to the emitting level, and thus only one of the two excitations involved in ET is transformed into heat; physically UPC+EPI transforms the pair of two interacting excited Nd ions into a pair (excited ion)-(non-excited ion) that could be suitable for subsequent DC. A special case of ET involves the complete transfer of excitation from an excited to a unexcited ion which is thus promoted to the initial excited state of the donor (excitation-conserving D-D ET). If this process repeats it can migrate the excitation to large distances from the originally-excited donor, till is lost either by emission or by transfer in an energy converting DC or UPC process (migration-assisted ET). Both DC and UPC could involve direct (static) D-A ET as well as migration-assisted transfer. The relative contributions of DC and UPC at any moment of decay will depend not only on the specific ET microparameters but also on the relative instantaneous populations of the acceptors for each of these processes, i.e. excited ions for direct UPC and non-excited ions for direct DC and for the energy migration and thus it will depend both on the initial density of excited ions and on its temporal evolution. Reduction of emission quantum efficiency by self-quenching could alter the laser parameters, whereas the various effects of heat generation could contribute to reduction of the laser beam quality and of the abilities of power scaling. Most early experiments on the emission decay of Nd^{3+} in YAG used weak excitation, which determines low initial density of excited ions and thus the effect of ET on decay could be described quite accurately assuming only DC processes [1,2], with constant concentrations of acceptors during decay. However, with stronger excitation the presence of UPC became evident [3-5] and many subsequent studies invoked UPC as the only ET effect, without considering the time-dependent balance between UPC and DC. Moreover, the UPC process was generally discussed in terms of a constant rate and without any account of existence of direct and migration-assisted processes and of distribution of the Nd ions in the crystalline lattice; moreover, the ET parameters reported by various authors differ in large limits.

The contribution of the ET to heat generation is determined by the competition with other de-excitation processes, i.e. it will be different for the ions participating or non-participating to lasing: whereas for the first of these the stimulated emission dominates all other de-excitation and the global heat generation is determined solely by the laser quantum defect, with no non-radiative de-excitation of the emitting level, for the second category additional heat generation from this level results from the competition of the luminescence with non-radiative ET de-excitation, characterized by the emission quantum efficiency η_{qe}. As consequence, the heat generation parameter η_h, which expresses the fraction of absorbed power transformed into heat, will be different for these two categories of de-excitation, $\eta_h^{(l)}$ and respectively $\eta_h^{(f)}$, and in presence of lasing the contribution of these two categories of ions, delineated by the laser emission efficiency η_l, to the intensity and distribution of heat generation must be considered.

This paper addresses some of the problems described above by considering the joint action of DC and UPC processes on the emission decay and on quantum efficiency for various relative strengths of these processes and different fractions of Nd ions excited by pump. Additionally, the effects of the spatial distribution of the pump and laser mode on the generated heat field are discussed.

THE EFFECT OF ENERGY TRANSFER ON EMISSION DECAY

General account

The non-radiative energy transfer is determined by the static interactions between the D and A ions [6] and it leads to de-excitation of donor with rates with specific dependence on D-A distance: $W_{DA}^{(s)} = C_{DA}^{(s)} / R_{DA}^6$ with *s*=6, 8 or 10 for electric dipole-dipole (d-d), dipole-quadrupole (d-q) and quadrupole-quadrupole (q-q) interactions, whereas the strong short-range superexchange coupling leads to very fast rates. The ET microparameters $C_{DA}^{(s)}$ reflect the electronic structure of the ions and although this process is non-radiative, they depend on the superposition integral of donor emission and acceptor absorption in the spectral range of transfer, $S_{DA} = \int \sigma_e^D(\nu)\sigma_a^A(\nu)d\nu$. The multipolarities of the electric ET interactions are thus determined by the selection rules for the transitions involved in the donor and acceptor act. The electric and superexchange interactions are cumulative and $W_{DA} = \sum_s (W_{DA}^{(s)}) + W_{DA}^{ex}$.

The D-A ET competes with other de-excitation processes and the transfer to a unique acceptor ion preserves the exponential decay but it reduces the lifetime τ_D of the donor to $\left(\tau_D^{-1} + W_{DA}\right)^{-1}$; however, in solids each donor is surrounded by a particular configuration of acceptors at distances R_j and its lifetime becomes $\left(\tau_D^{-1} + \sum_j W_j\right)^{-1}$. The emission decay of the whole ensemble of donors would assume the impossible task of summing the individual contributions, but this could be replaced by proper averaging procedures based on the distribution of the doping ions in the laser material. The averaging procedure will then enable definition of an ET function $P(t)$ as the survival probability of the donor in its excited state in presence of transfer is $\exp[-P(t)]$. With this transfer function the emission decay becomes

$$I(t) = I(0)\exp(-t/\tau_D)\exp[-P(t)] \tag{1}$$

and a similar equation can be written for the evolution of the donor population in excited state n_D, which can be regarded as solution of population evolution equation

$$\frac{dn_D}{dt} = -\frac{1}{\tau_D}n_D - \frac{dP(t)}{dt}n_D . \tag{2}$$

The form of transfer function depends on the model of distribution of the ions in lattice used in the averaging procedure. In the almost general situation of absence of attractive or repulsive forces between the doping ions the most popular models of distribution are:

-*the average distance model* assumes that the doping ions are placed evenly in crystal at distances ~$(n_{Nd})^{-3}$. In this model the configurations of acceptor ions around any donor ion and thus all ET rates are identical and the emission decay remains exponential, but with Nd concentration dependence [7]: for d-d coupling $W_{DA} \propto (n_{Nd})^2$. This model is very simple but not realistic and does not account for the structure of the crystal.

-*the uniform continuous model* assumes that the density of acceptors around donor is the same in each geometrical point of space [6,8,9]. The transfer function is non-linear in time, $P(t) = \gamma^{(s)}t^{3/s}$, and $\gamma^{(s)}$ depends on C_{DA}: for d-d coupling $P(t) = \gamma^{d-d}t^{1/2}$, with $\gamma^{(d-d)} = (4/3)\pi^{3/2}n_{Nd}(C_{DA})^{1/2}$. The decay predicted by this model is not exponential and the fit with experimental data enables

identification of the multipolarity *s* of ion-ion interaction and evaluation of C_{DA}. The model is restricted to unique type of interaction, it does not account for the structure of the crystal and predicts finite density of acceptors at the donor position;

-*the discrete random distribution* assumes discrete occupation by acceptors of any available lattice site *i* with same probability [10], equal to relative acceptor concentration C_A,

$$P(t) = \sum_i \ln\left[1 - C_A + C_A \exp(-W_i t)\right] \tag{3}$$

This model is the most realistic since it accounts for the crystal structure (the positions *i*), and the rates W_i can include any type of interaction; it predicts complex decay, with departures from exponential. In case of Nd^{3+} the microparameter C_{DA} for the direct ET is larger than that of the D-D energy-conserving transfer C_{DD}, and the migration of excitation inside the system of Nd^{3+} ions takes place by the hopping mechanism [11]. In this case the migration-assisted self-quenching can be characterized by an ensemble-averaged transfer function linear in time $P_{ma} = \overline{W}t$, with the rate depending on the acceptor concentrations specific to both of these successive processes, $\overline{W} = \overline{W}_0 C_D C_A$ and with the microparameter $\overline{W}_0$ dependent on both C_{DA} and C_{DD}. In presence of the direct and of migration-assisted transfer processes

$$I(t) = I(0)\exp(-t/\tau_D)\exp\left[-P(t)\right]\exp(-\overline{W}t) = I(0)\exp(-t/\tau_D)\exp\left[-P'(t)\right]. \tag{4}$$

Although the direct and migration-assisted ET act together over the entire decay, due to the different dependences on time the migration-assisted transfer is manifested as a new quasi-linear dependence of the global transfer function $P'(t) = P(t) + \overline{W}t$ at the end of decay.

The ET processes could involve a unique or several types of acceptors and in this case the transfer function $P(t)$ can be written as sum of the transfer functions to each acceptor species. Such situation holds for the general case of ET self-quenching of Nd laser materials, due to the co-existence of the two types of processes, down-conversion and upconversion, but it is a special case, since the concentrations of acceptors for these processes are correlated and dependent of time [12-14]. Thus, by denoting the fraction of Nd excited ions by $r(t) = r(0)\exp(-t/\tau_D)\exp\left[-P'(t)\right]$, the relative instantaneous concentrations of acceptors is $\left[1 - r(t)\right]C_{Nd}$ for down-conversion and $r(t)C_{Nd}$ for upconversion.

The effect of down-conversion self-quenching on decay

For very small $r(0)$ fractions the down-conversion dominates the self-quenching and the influence of upconversion can be neglected to a quite good approximation; in fact, most of measurements of decay of Nd^{3+} fulfill this condition. For this case C_A in Eq. (3) could be considered constant during decay and equal to the relative Nd concentration C_{Nd}. Function (3) is difficult to use directly; however, over definite intervals of decay it can be approximated by more simple functions [1, 2]: at early times it could show linear dependence on time, $P(t) \approx \sum_i C_A W_i t = W_{lin} t$, whereas at longer times it could be approximated by the function corresponding to the uniform continuous distribution. When a very strong short-range interaction, such as superexchange is active in the transfer to the nearest acceptors a fast drop of the emission takes place at beginning of decay, and is followed by the linear approximation with the positions influenced by the strong interaction excluded from summ, the passage between these stages being gradual. This is precisely what it happens in the high resolution decay of Nd:YAG under weak excitation [15,16] where the almost sudden initial drop ~$4C_{Nd}$ of $P(t)$ evidences strong coupling between the Nd^{3+} ions inside the n.n. pair with transfer rate larger than 10^6 s^{-1}. The subsequent portion quasi-linear in time corresponds to the linear approximation of $P(t)$, and this is followed by a portion with $t^{1/2}$ dependence corresponding to d-d coupling with $C_{DA} \approx 1.85 \times 10^{-40} cm^6 s^{-1}$ [2]. Calculation of rate W_{lin} with this microprameter gave satisfactory fit to experiment only by excluding the first four sites from summation, in accord with the dominance of the faster superexchange coupling inside the n.n. pair. Such behavior was observed for many other Nd laser materials, but it requires high temporal resolution of detection, tens of ns, and pulse excitation in the ten ns range. In case of down-conversion migration-assisted ET both the concentrations of ions able to fill the role of donor or acceptor are equal to the Nd concentration and thus the averaged transfer function becomes $\overline{W} = \overline{W}_0 C_{Nd}^2$: in Nd:YAG $\overline{W}_0 = 240$ s^{-1}(%Nd)$^{-2}$.

The effect of upconversion on the emission decay

The upconversion was usually considered as unique source of self-quenching of Nd^{3+} at strong excitation and the effect on decay was described by the population evolution equation

$$\frac{dn_D}{dt} = -\frac{t}{\tau_D} n_D - W^{(up)} n_D^2 \tag{5}$$

This equation is convenient since it has analytical solution and generally it gives acceptable formal description of the observed decay. However, the physical meaning of this approach is highly questionable since the upconversion is described by a constant rate W^{up}, which does not account for the nature of process (static, migration-assisted), for type of ion-ion interaction or for the real distributions of acceptors in crystal, and the down-conversion is either disregarded or included as a constant contribution in the lifetime τ_D. The upconversion transfer rates reported by various authors for Nd:YAG show large spread: for 1 at.% Nd the rate inferred from emission decay of a crystal was (2.8±1)×10^{-16} cm^3s^{-1} [3], whereas in case of thin films this was about 5 times smaller [4], and this last value was confirmed by the subsequent measurements on crystals [5]. The upconversion rate W^{up} inferred from these studies is much higher than that for down-conversion: this is not surprising, since the upconversion includes four processes and the overlap integral *S* could be much larger.

As discussed above, the upconversion cannot exclude the simultaneous presence of down-conversion and in the model of random distribution of the doping ion the ET function $P(t) = P^{dw}(t) + P^{up}(t)$, with

$$P^{dw}(t) = \sum_i \ln\left\{1 - [1 - r(t)]C_{Nd} + [1 - r(t)]C_{Nd} \exp(-W_i^{dw} t\right\} \text{ and}$$
$$P^{up}(t) = \sum_i \ln\left[1 - r(t)C_{Nd} + r(t)C_{Nd} \exp(-W_i^{up} t)\right] \text{ [13,14],}$$

whereas for the migration-assisted ET $\overline{W} = \overline{W}^{dw} + \overline{W}^{up}$,

with $\overline{W}^{dw} = \overline{W}_0^{dw}[1 - r(t)]^2 C_{Nd}^2$ and $\overline{W}^{up} = \overline{W}_0^{up} r(t)[1 - r(t)]C_{Nd}^2$

The ET microparameters for down-conversion can be measured independently at low excitation, whereas those for upconversion could be inferred from the fit at higher excitation by using these down-conversion parameters and usually a general ratio R of the microparameters for upconversion to those for down-conversion could be considered. Under these assumptions, it was found [12] that the decays for 1.7 at.% Nd-YAG thin films [4] can be described by assuming R in the range 20-30.

THE EFFECT OF SELF-QUENCHING ON THE EMISSION QUANTUM EFFICIENCY

The emission quantum efficiency η_{qe} expresses the fraction of the excited ions fed into the emitting level that de-excite by radiative processes. It can be measured directly by the total amount of radiated energy or indirectly, by the thermal effects of the heat generated by the non-radiative processes, such as the rise of temperature, photoacoustic spectrometry, calorimetric interferometry, laser thermal depolarization, thermal lensing, thermal line broadening, and so on. These measurements give quite large spread of data and thus a valuable test of validity could be the η_{qe} calculated from the emission decay $I(t)$,

$$\eta_{qe} = \frac{1}{\tau_{rad}} \int_0^\infty \frac{I(t)}{I(0)} dt \tag{6}$$

This equation requires knowledge of τ_{rad} and accurate description of decay. For exponential decay with lifetime τ_f, $\eta_{qe} = \tau_f / \tau_{rad}$. The calculated η_{qe} enables definition of an effective lifetime of the non-exponential decay as $\tau_{eff} = \eta_{qe} \tau_{rad}$. Evaluation of η_{qe} for complex decays would require numerical calculation. However, in certain cases η_{qe} can be expressed by closed formula, dependent on the distribution model. Thus, in case of down-conversion ET,

-in the average-distance model $\eta_{qe} = \left[1 + (C_{Nd}/C_0)^2\right]^{-1}$, where C_0 is the Nd concentration that reduces the lifetime to $0.5\,\tau_D$ [8]; despite of the lack of reality of this model, this equation is largely used to predict the Nd concentration dependence of η_{qe};

-for the uniform continuous distribution $\eta_{qe} = 1 - \pi^{1/2} x \exp(x^2)\left[1 - erf(x)\right]$, where $x = \; x = (1/2)\pi^{1/2} C_{Nd} / C_0$ [9].;

-in the random discrete model for direct ET $\eta_{qe} \approx \exp(-bC_{Nd})$ with

$b = \sum_i \frac{W_i}{\tau_D^{-1} + W_i}$ [14].; in presence of migration-assisted ET

$$\eta_{qe} = \frac{1}{1 + \tau_D \overline{W}_0 C_{Nd}^2} \exp\left(- \sum_i \frac{W_i}{\tau_D^{-1} + W_i + \overline{W}_0 C_{Nd}^2} C_{Nd} \right)$$ [13,16]

and the calculated η_{qe} for Nd:YAG crystals or ceramics (Figure 1) gives very good description of experimental values: for 1 at.% Nd it predicts $\eta_{qe} \approx 0.80$ and $\tau_{eff} = 208$ μs.

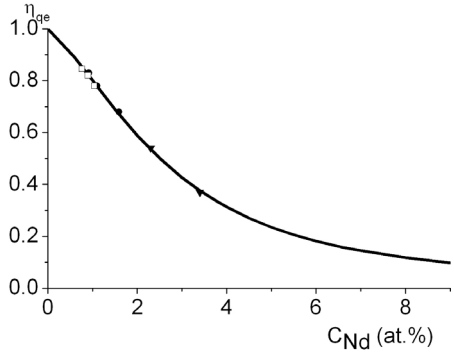

Figure 1. Emission quantum efficiency of Nd:YAG at weak excitation

Evaluation of η_{qe} in presence of both down-conversion (dc) and upconversion (uc) requires numerical calculation. For the low C_{Nd} used in the Nd lasers this corresponds well to the product of efficiencies of each of these conversion processes calculated with the transfer functions $P^{dw}(t)$ and respectively $P^{up}(t)$, i.e. $\eta_{qe}^{(dw+up)} \approx \eta_{qe}^{(dw)}\eta_{qe}^{(up)}$. The numerical calculation in case of 0.6, 1 and 1.5 at.%Nd in YAG under 809 nm pumping for different ratios R between the upconversion and down-conversion ET parameters (1 to 50) and for different initial fractions of excited ions $r(0)$ (0 to 1) reveals that starting from the C_{Nd}-dependent values for weak excitation (0.875, 0.800 and 0.680 for 0.6, 1 and 1.5 at.%Nd) at $r(0)=0$, η_{qe}^{dw} increases quasi-linearly with $r(0)$, with C_{Nd}-dependent slope, whereas η_{qe}^{up} starts from the value 1 for all C_{Nd} and decreases non-linearly with $r(0)$, more accentuated at higher C_{Nd} and R ratios. Thus, η_{qe}^{up} could be larger than η_{qe}^{dw} even for large R ratios, up to quite large $r(0)$ fractions, and the range extends for higher C_{Nd}; however, $\eta_{qe}^{(dw+up)}$ is always smaller than either η_{qe}^{dw} or η_{qe}^{up} and this situation is illustrated in Fig. 2 for R =30.

In a CW laser the threshold $P_{th} \propto \left(\eta_a \eta_{qe} \eta_{qd}^{(l)}\right)^{-1}$ and the slope efficiency $\eta_{sl} \propto \eta_a \eta_{qd}^{(l)}$, where η_a is the pump absorption efficiency and the Stokes ratio between the pump and laser wavelengths characterizes the laser quantum defect, $\eta_{qd}^{(l)} = \lambda_p / \lambda_l$. Reduction of η_{qe} at high C_{Nd} increases P_{th} but it has no effect on η_{sl};

moreover this could be compensated over a certain range of C_{Nd} by the enhancement of η_a, which could also enhance η_{sl}. Of major importance could be reduction of laser quantum defect: for the Nd lasers, where traditionally the diode laser pumping is made around 808 nm in the strongly absorbing level $^4F_{5/2}$ this can be made by direct ~880 nm pumping into the emitting level $^4F_{3/2}$ [17,18]: the reduction of 9-10% of the quantum defect will determine similar improvement of the laser parameters P_{th} and η_{sl}. Unfortunately, for most Nd materials the absorption cross-section for direct pumping could be considerably smaller than for traditional 800 nm pumping and this could impose special care to improve the absorption efficiency, such as higher C_{Nd} or longer pump radiation path inside the laser material using large active components or multipass pumping.

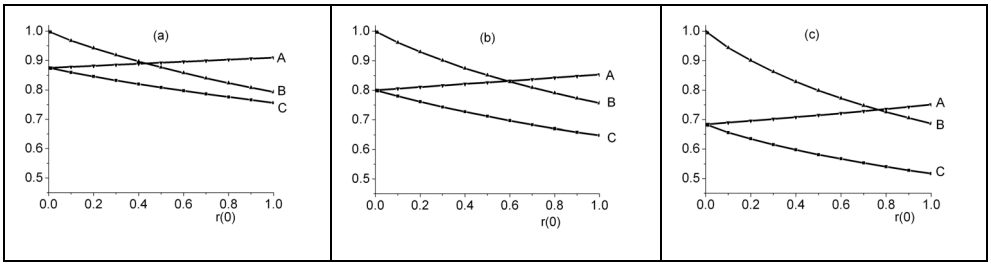

Figure 2. Calculated emission quantum efficiencies function on initial fraction of excited ions r(0) for Nd concentrations 0.6 at% (a), 1 at.% (b) and 1.5 at.% (c) and *R*=30: A - dc, B – uc, C – dc+uc

THE EFFECT OF SELF-QUENCHING ON HEAT GENERATION

By the involvement of EP interaction the self-quenching could contribute jointly with the quantum defect to heat generation in the pumped laser materials. The heat generation can be characterized by the heat load coefficient η_h that expresses the fraction of the absorbed power transformed into heat by non-radiative de-excitation: in CW emission processes this parameter is constant. In absence of laser emission both the emission quantum defect and the self-quenching of the emitting level are active and $\eta_h^{(f)} = 1 - \eta_{qe}\eta_{qd}^{(f)}$.

Under weak excitation the down-conversion makes η_{qe} dependent only on C_{Nd} and thus $\eta_h^{(f)}$ depends only on C_{Nd} and on λ_p. However, under strong excitation the joint action of down- and upconversion makes η_{qe} and $\eta_h^{(f)}$ dependent also on the fraction $r(0)$ and on ratio *R*. Calculation of $\eta_h^{(f)}$ for different C_{Nd} s in YAG using the calculated η_{qe} in presence of only down-conversion $\eta_h^{(f,dw)}$, only upconversion $\eta_h^{(f,up)}$ and of both down- and upconversion $\eta_h^{(f,dw+up)}$ shows that $\eta_h^{(f,dw)}$ starts from the C_{Nd} -dependent weak excitation values (0.318 for 0.6, 0.377 for 1 and 0.470 for 1.5 at.% Nd) and decrease quasi-linearly with *r*(0), whereas $\eta_h^{(f,up)}$ starts from the C_{Nd} -independent quantum-defect limited value for luminescence (~0.22 in case of 809 nm excitation) and increases with $r(0)$, faster for large C_{Nd}. However, for definite $r(0)$ ranges $\eta_h^{(f,up)}$ is smaller than $\eta_h^{(f,dw)}$ and well under the values measured for $\eta_h^{(f)}$ below threshold for the Nd:YAG lasers. Thus, $\eta_h^{(f)}$ around 0.38 was currently measured for 1 at.% Nd:YAG under weak excitation in absence of laser emission, in agreement with the calculated value of $\eta_h^{(f,dw)}$, but much above $\eta_h^{(f,up)}$. At the same time, the calculated $\eta_h^{(f,dw+up)}$ starts from the value corresponding to $\eta_h^{(f,dw)}$ but increases with $r(0)$ and it is always larger than both $\eta_h^{(f,dw)}$ and $\eta_h^{(f,up)}$. This is illustrated in Figure 2 with the calculated values of $\eta_h^{(f)}$ for 0.6, 1 and 1.5 at.% Nd:YAG with R =30 under 809 nm excitation, using the η_{qe} values presented in Fig. 2. These data show that upconversion alone cannot explain the heat generation and the assistance of down-conversion should be always accounted for.

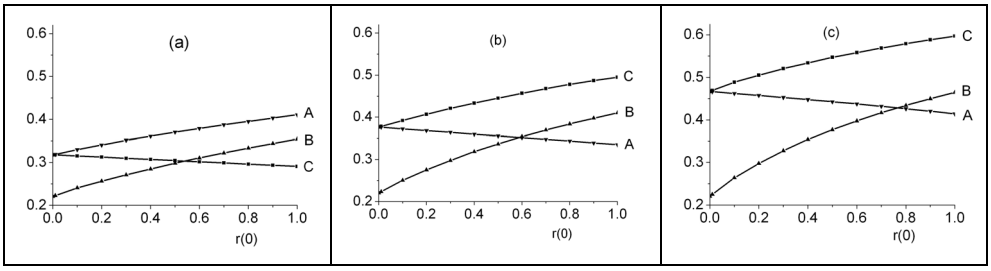

Figure 3. The calculated heat load parameter for 0.6 at.% Nd, (a), 1 at.% Nd (b) and 1.5 at.% Nd (c) in YAG for R=30: A – dc, B – uc, C – dc+uc.

In a pumped laser material the modal structure of the laser resonator, which determines the spatial configuration of excited ions that can be de-excited by stimulated emission could differ from the configuration of excited ions, determined by that of absorbed pump radiation; the relation between these two spatial configurations is characterized by the volume superposition integral η_v. Generally, it is considered that η_v =1 when the laser mode volume is larger than the absorbed pump volume and <1 in the opposite situation. Additionally, the laser process needs a threshold population which is reached for a given absorbed power P_{th}. As consequence not all excited ions participate to lasing and these can de-excite by luminescence and competing non-radiative de-excitation; these two classes of excited ions are delineated by laser emission efficiency $\eta_l = \eta_v\left[1-(P_{th}/P)\right]$. The stimulated emission is faster than any other de-excitation process and thus the only contribution of the lasing ions to the heat generation comes from the laser quantum defect and their heat load coefficient is $\eta_h^{(l)} = 1-\eta_{qd}^{(l)}$. The relation between the heat generated by the lasing ions and those that do not lase is governed by relation between $\eta_{qd}^{(l)}$ and $\eta_{qe}\eta_{qd}^{(f)}$ and for a given laser emission scheme in a given material it can be controlled by the doping concentration. The global contribution to heating of the excited ions is then

$$\eta_h = \eta_l\eta_h^{(l)} + (1-\eta_l)\eta_h^{(f)} = 1-\eta_l\eta_{qd}^{(l)} - (1-\eta_l)\eta_{qe}\eta_{qd}^{(f)} \tag{7}$$

Reduction of the quantum defect by direct pumping around 880 nm could reduce the heat generation for the one-micron CW Nd lasers by ~30% compared with 808 nm pumping and this could increase the power scaling ability by more than 55% [19].

SPATIAL DISTRIBUTION OF LASER, HEAT GENERATION AND LUMINESCENCE

The spatial distribution and not only the global value of heat generation could be of major relevance. Most papers consider the configuration of heat generation similar to that of the absorbed power. Based on differences in heat generation between the lasing and non-lasing ions it can be shown that the laser mode-pump volume superposition plays a major role and can distort such picture. Figure 4 shows the calculated radial distribution of heat and luminescence for 1 at.% Nd:YAG under uniform or Gauss 809 nm pumping for Gaussian one-micron laser emission with waist 60% from the absorbed pump waist and for P/P_{th} =10.

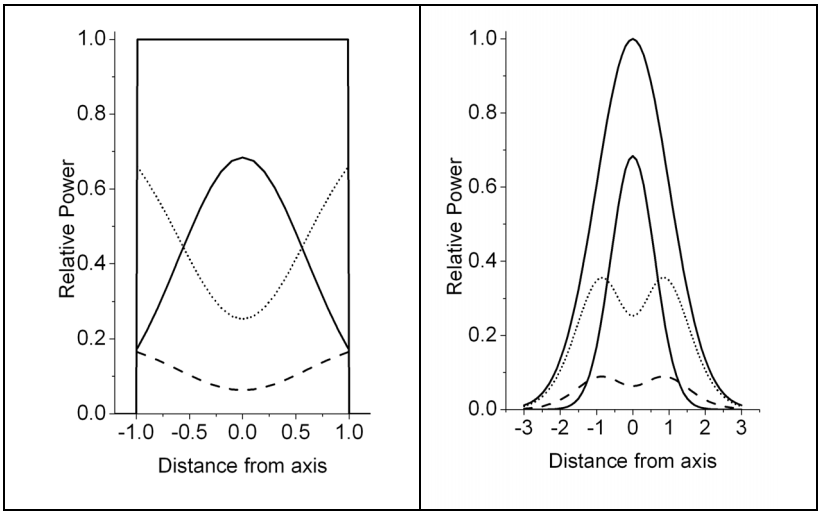

Figure 4. The calculated radial distribution of one-micron laser (full lines), luminescence (dashed lines) and heat generation for 1 at.% Nd:YAG under uniform (left side) or Gauss (right side) 809 nm pumping (external contours)

These distributions are calculated assuming weak pumping, with neglect of upconversion and show that even in these conditions, the excited ions outside the laser mode distort the distribution of heat generation; upconversion will accentuate these effects.

CONCLUSION

Concentration self-quenching in the Nd laser materials is a complex process which influences the dynamics of emission and reduces the emission quantum efficiency, leading to enhancement of laser threshold and contributing to generation of heat. Limitation of these effects requires detailed knowledge of the self-quenching mechanism: this paper shows that in case of Nd the down- and upconversion self-quenching act together in a correlated manner and, whereas down-conversion dominates at weak excitation, upconversion at higher excitation cannot be considered alone. The differences in the heat generation of the lasing and non-lasing ions could influence the thermal field inside the pumped laser material.

ACKNOWLEDGMENTS

This work was supported by a grant of the Romanian National Authority for Scientific Research, CNCS - UEFISCDI, project number PN II-PCE-IDEI-35/2011

REFERENCES

1. A.G. Avvanesov, B.I. Denker, V.V. Osiko et al., *Sov. J. Quantum Electron*. 12, 744 (1982)
2. V. Lupei, A. Lupei, S. Georgescu, C. Ionescu, *Opt. Commun*. 60, 59 (1986)
3. Y. Guyot, H. Manaa, J. Y. Rivoire, R. Moncorge et al, *Phys. Rev.* B51, 784 (1995)
4. S. Guy, C. L. Bonner, D. P. Shepherd, D. C. Hanna et al, *IEEE J. Quant. Electron*. 34, 900 (1998)
5. M. Pollnau, P. J. Hardman, M. Kern, W. A. Clarkson, D. C. Hanna, *Phys. Rev.* B58, 16076 (1998) 1
6. D. L. Dexter, *J. Chem. Phys*. 21, 836 (1953)
7. H. G. Danielmeyer, M. Blatte, P. Palmer, *Appl. Phys.* 1, 269 (1973)
8. Th. Forster, *Ann. Phys.* (Leipzig) 2, 55 (1948)
9. M. Inokuti, F. Hirayama, *J. Chem. Phys*. 43, 1978 (1965)
10. S. I. Golubov, Yu. V. Konobeev, *Sov. Phys. Sol. State* 13, 2679 (1972)
11. A. I. Burshtein, *Sov*. *Phys. Uspekhi* 27, 579 (1984)
12. V. Lupei, B. Diaconescu, A. Lupei, *Proc. SPIE* 4430, 88 (2001)
13. V. Lupei, *Opt. Mat.* 19, 95 (2002)
14. A. Ikesue, N. L, Aung, V. Lupei, Ceramic Lasers, Cambridge Univ. Press 2013
15. V. Lupei, A. Lupei, *Phys. Rev*. B61, 8087 (2000)
16. V. Lupei, A. Lupei, S. Georgescu, T. Taira, Y. Sato, A. Ikesue, *Phys. Rev*. B64, 092102 (2001)
17. R. Lavi, S. Jackel, *Appl. Opt*. 39, 3093 (2000)
18. V. Lupei, A. Lupei, N. Pavel, T. Taira, I. Shoji, A. Ikesue, *Appl. Phys. Lett*. 79, 590 (2001)
19. V. Lupei, *Opt. Mat*. 31, 701 (2009)

STUDIA UBB PHYSICA, Vol. 60 (LX), 1, 2015, pp. 45-52
(RECOMMENDED CITATION)

Dedicated to Academician Professor Dr. Emil Burzo on His 80th Anniversary

MAGNETORHEOLOGICAL ELASTOMER ELASTICITY - BASED CAPACITOR

O.M. BUNOIU[1*], I. BICA[1], L. CHIRIGIU[2], G. CIRTINA[1], L. IORDACONIU[1]

ABSTRACT. In the present paper, a magnetorheological elastomer (MRE) based on silicone rubber, magnetorheological suspension and catalyst, in a magnetic field, is obtained. Using the plane capacitor method, it is shown that the elastic properties of the magnetorheological elastomer are influenced by the intensity and direction of the applied magnetic field. The obtained experimental results are presented and discussed.

Keywords*: silicone rubber, magnetorheological elastomer, plane capacitor, carbonyl iron, magnetic Young modulus.*

INTRODUCTION

Magnetorheological elastomers (MREs) are part of the magnetically active materials category. They consist of an elastic matrix into which magnetizable nano- or microparticles are dispersed or aligned [1-4]. Like in the case of the magnetorheological suspensions [5-9], some physical the physical properties like of the MREs drastically change under the action of the magnetic field. This particular feature is used in mechanical shocks absorbers and dampers [10], (bat the damping mechanism differs from the classical magnetomechanical damping magnetostrictive ferromagnets [11-14]).

[1] *Department of Physics, West University of Timisoara, Bd. V. Parvan, nr.4, Timisoara 300223, Romania*
[2] *Department of Analytical Chemistry,* University of Medicine and Pharmacy, *Petru Rares Street, No. 2–4, Craiova, Romania*
** Corresponding author e-mail: madalin.bunoiu@e-uvt.ro*

One property of interest is related to the change of the electric conductivity of MREs in a magnetic field [15, 16], property used in obtaining active or passive electric circuit elements [17-22]. Such devices can be used in the manufacturing of deformations and mechanical tensions sensors and/or transducers. The physical properties of the MREs [1-4, 10, 15-23] strongly depend on the method of preparation. In this context, the obtaining procedure at an anisotropic MRE and the study of its elastic properties by means of the plane capacitor method is presented in the paper.

EXPERIMENT

Plane capacitor with MRE

The components used in obtaining the plane capacitor with MRE-based dielectric material are: silicone rubber, RTV-3325 (Bluestar – Silicones), silicone oil (Merck), catalyst, 60R (Merck) and carbonyl iron (Sigma) as microparticles with diameter between 4.5μm and 5.4μm and iron content of min 97%. A liquid mixture, consisting in 2.4cm^3 carbonyl iron and 0.2cm^3 silicone oil, is brought to the temperature of 573±5% [20] and maintained at this temperature for ≈5 minutes. At the end of the 5 minutes time the mixture is allowed to reach room temperature. Following the thermal decomposition of carbonyl iron, iron nanoparticles with average diameter of 61.2nm are formed inside the liquid matrix [20]. The obtained product is mixed and homogenized with silicone rubber (1.2cm^3±10%) and catalyst (0.2cm^3±10%). The formed mixture is injected between two parallel copper plates (diameter 30mm), provided on the outline with a spacer so as to maintain the distance between the plates at 3.5mm±10%.The as-formed set was placed between the poles of a type Phylatex (Germany)-Weiss electromagnet. The magnetic field has a normal direction to the surface of the plane capacitor plates and intensity of H=840kA/m±10%. After 24 hours, a plane capacitor with MRE dielectric material based on silicone rubber and iron nanoparticles (60% vol.) is obtained.

Measurements

The electric capacity of the plane capacitor at the temperature of the environment (296 K ± 10%) and in the absence of the magnetic field is measured with the capacimeter CM-7115A (Fujian). The capacitor with MRE is introduced in a transverse magnetic field (normal to the plates) and then in a longitudinal magnetic field (in plane). Three sets of measurements are performed with the CM-7115A (Fujian) capacimeter precision.

RESULTS AND DISCUSSION

The average values of the capacity *C* as a function of the magnetic field intensity *H* are presented in Fig.1a. At *H*=0, the capacity of the plane capacitor is fixed to the value C_0=96pF. We note with C_T the capacity of *C* in a transverse magnetic field and with C_L the capacity of the same *C* in a longitudinal magnetic field. When applying a transverse magnetic field ($0<H(kA/m)\leq 400$), the value of *C* jumps from C_0=96pF to C_T=124 pF, for *H*= 15kA/m. For $15<H(kA/m)\leq 400$, C_T has a quasi-linear growth with *H*. At *H*=400 kA/m one obtains $C_T=157pF$. In a longitudinal magnetic field, the values $C_L(H)<C_T(H)$. Here, as Figure 1 shows, two regions of $C_L=C_L(H)$, namely: $96\leq C_L(pF)\leq 97.5$, for: $0\leq H(kA/m)\leq 100$; $97.5<C_L(pF)\leq 131$, and for: $100<H(kA/m)\leq 400$, can be observed. Neglecting the edge effects [27], the capacitance of the plane capacitor with MRE based dielectric may be approximated to:

$$C_0=\varepsilon_0\varepsilon_r\frac{\pi d^2}{4h_0},\ \text{for } H=0 \quad \text{and} \quad C=\varepsilon_0\varepsilon_r\frac{\pi d^2}{4h},\ \text{for } H\neq 0 \tag{1}$$

Here ε_0 =8.85 pF/m, ε_r is the relative permittivity of the MRE; *d*, h_0 and *h* are the diameter and thicknesses of the MRE.

The linear magnetic strain is:

$$e=(h-h_0)/h_0=[(C_0/C)-1] \tag{2}$$

where h_0 and *h* can be obtained from Eqs.(1) .

For C_0 si *C=C(H),* from Fig.1, introduced in (2), on obtained in Fig.2, (e_T) transversal magnetic linear strain and (e_L) magnetic longitudinal linear strain.

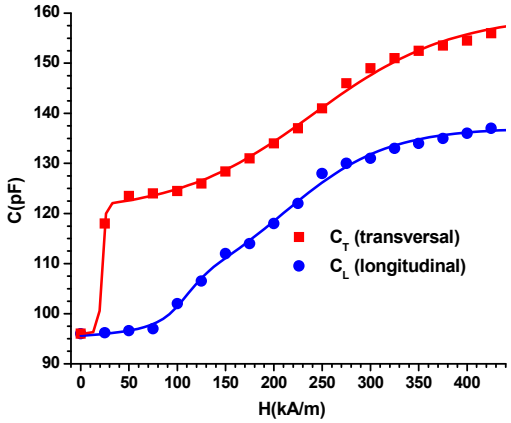

Fig. 1. Capacitance C of the plane capacitor as a function of the strength magnetic field H.

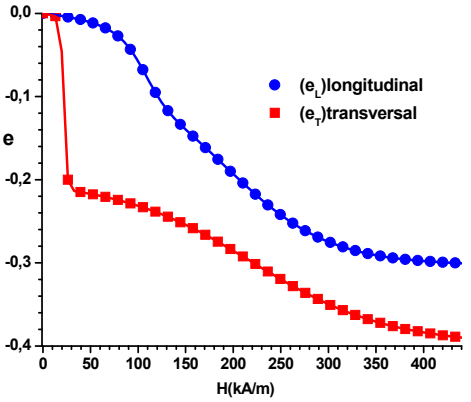

Fig. 2. The linear magnetic strain e as a function of the strength magnetic field H.

We see from Fig. 2 like MRE is compressed. MRE compression value depends on the strong magnetic field intensity vector direction. From Fig.2, it is observed that for H ≥ 20kA/m, compressing due to the transverse magnetic field is far enlarging compared to that due to the longitudinal magnetic field. In a magnetic field, the nanoparticles from the inside of the elastic matrix are magnetized. We consider that the nanoparticles are of diameter $d \approx d_m$. Then, their magnetic moment is [25]:

$$m = \frac{\pi}{6} d_m^3 \chi H \cos\alpha \tag{3}$$

where d_m is the diameter of the magnetizable particles, H is the magnetic field strength and α is the angle between the $\vec{H}$ and direction of chains magnetic dipoles $\vec{m}$.

The parameter χ is the initial magnetic susceptibility of the MRE. For $\mu_p >> \mu_e$ (μ_p and μ_e are the relative magnetic permeability of the iron nanoparticles and silicone rubber) this may approximated to [25]:

$$\chi = 3\frac{\mu_p - \mu_e}{\mu_p + 2\mu_e} \approx 3 \tag{4}$$

Introducing the expression (4) into Eq. (3) yields:

$$m = 0.5\pi d_m^3 H \cos\alpha \tag{5}$$

We consider $\vec{H}$ constant. Then, between two neighboring and identical magnetic dipoles, an attractive magnetic force occurs [20, 25]:

$$F_m = -\frac{3\mu_0\mu_e m^2}{\pi\, r^4} \tag{6}$$

where μ_0 = 12.56 x 10^{-7} H/m and *r* is the distance between the centers of the two dipoles.

The mechanical stress induced in to the MRE by F_m [26]:

$$\sigma = N_C \, F_m \big/ S = \frac{3}{2}\varphi \frac{F_m}{\pi\, d_m^2} \tag{7}$$

where N_c/S is the number of columns per transverse cross-section unit of MRE [26] and φ is the volume fraction of the iron nanoparticles.

From Eqs. (5), (6) and (7), which for $r=d_m$ results mechanical stress induced in to MRE by longitudinal magnetic field, i.e.:

$$\sigma_L = -4.5\varphi\mu_0 H^2 \cos^2\alpha \tag{8}$$

Here α is the angle between vector intensity of magnetic field and the direction of the dipoles columns.

For α=0, the stress is maximum and has the expression:

$$\sigma_T = -4.5\,\varphi\mu_0 H^2 \tag{9}$$

where σ_T is the stress component corresponding to vector intensity magnetic field normal to the plates.

For the magnetic tension, Eqs. (8) and (9), the elastic matrix reacts with the longitudinal elastic tension σ_{eL} and the transverse elastic tension $\sigma_{eT,}$ respectively.

At equilibrium are available equalities $\sigma_{eL} = \sigma_L$ and $\sigma e_T = \sigma_T$ or:

$$4.5\varphi\mu_0 H^2 = k_L\, d_0/S\, [(h/h_0)\text{-}1]_L \cos^2\alpha = k_L\, h_0/S\, [(C/C_0)\text{-}1]_L \cos^2\alpha = E_L\, e_L \tag{10}$$

$$4.5\varphi\mu_0 H^2 = k_T\, d_0/S\, [(h/h_0)\text{-}1]_T = k_T\, h_0/S\, [(C/C_0)\text{-}1]_T = E_T\, e_T \tag{11}$$

where k_L and k_T are MRE elastic constant, $e_L=[(C/C_0)\text{-}1]_L$ and $e_T=[(C/C_0)\text{-}1]_T$ are the longitudinal and the transversal linear strain, *S* is surface aria and:

$$\boldsymbol{E_T} = k_T\, d_0/S \text{ and } E_L = k_L\, d_0/S \cos^2\alpha \tag{12}$$

is the magnetic elasticity module (E_T) for transversal magnetic field and (E_L) is the magnetic elasticity module for longitudinal magnetic field. From Eqs. (10) and (11) results:

$$E_L = 4.5\varphi\mu_0 H^2/[(C/C_0)\text{-}1]_L \text{ and } E_T = 4.5\varphi\mu_0 H^2/[(C/C_0)\text{-}1]_T \quad (13)$$

The angle of α is obtained from the Eqs. (12) and (13), namely:

$$\alpha = \arccos[(E_T/E_L)^{0.5}] \quad (14)$$

For $\varphi = 0.60$, $\mu_0 = 12.56 \times 10^{-7}$ H/m and $(C/C_0)_{L,T}$, from Fig. 1, and the Eqs. (13) can be obtained $E_{L,T} = E_{L,T}(H)$, plotted in Fig. 3.

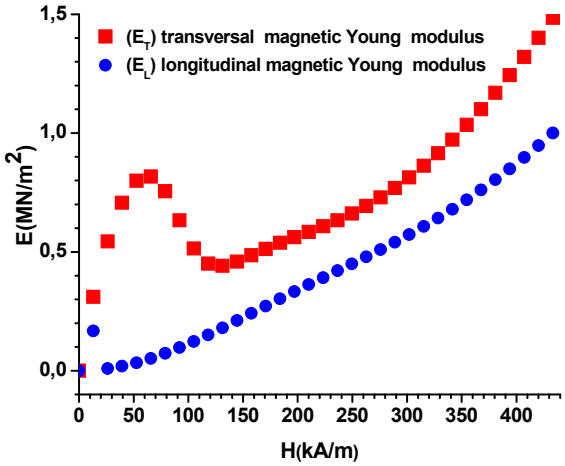

Fig. 3. Magnetic module E_T and E_L function of the magnetic strength field H.

Introducing $E_{L,T} = E_{L,T}(H)$ from Fig. 3 in Eqs. (14), and obtained $\alpha = \alpha(H)$, plotted in Fig. 4.

Shall see from Fig.4, as the angle α are shrinking as the H increase, corresponding with the modification of E_L, from Fig. 3. Introducing $C=C(H)$ values (Fig. 1a) and C_0=96pF into Eq. (10) and the dependence $e=e(H)$ is obtained as shown in Fig. 2. It can be noticed the linear strain e increases with the magnetic field $\vec{H}$ and it is sensibly dependent its direction. For $\alpha=0$ (transverse magnetic field) expression (11) can be rewritten as $\sigma_T = E e_T$. Then, using Eq. (7) for φ=0.60, $0 \le H(kA/m) \le 440$ and $e_T = e_T(H)$ from Fig. 2 one obtains $E=E(H)$ as plotted in Fig. 3. It can be noticed from Fig. 3 that the magnetic Young modulus E sensibly increases with H, in accord with the model proposed in Refs. [28, 29]. The columns formed by the iron nanoparticles have the same direction as $\vec{H}$. At the moment of a longitudinal magnetic field application ($\vec{H}$ *in plane)* the chains formed by the iron nanoparticles

tend to orient towards $\vec{H}$. An angle α will occur between the direction of $\vec{H}$ and that of the chains. We intend to determine α with the growth of $\vec{H}$. For this, we use the expression (6), *E=E(H)* from Fig. 3 and $e_L = e_L(H)$ from Fig. 2. Then, for φ=0.60 and *0 ≤ H (kA/m) ≤ 440*,the dependence $\alpha = \alpha(H)$ will be obtained as plotted in Fig.4. It can be seen from Fig. 4 that the angle α decreases with the increase of *H*. According to Refs. [28, 29] the value of α depends on $F_m \sim H^n$ (where $n \leq 2$).

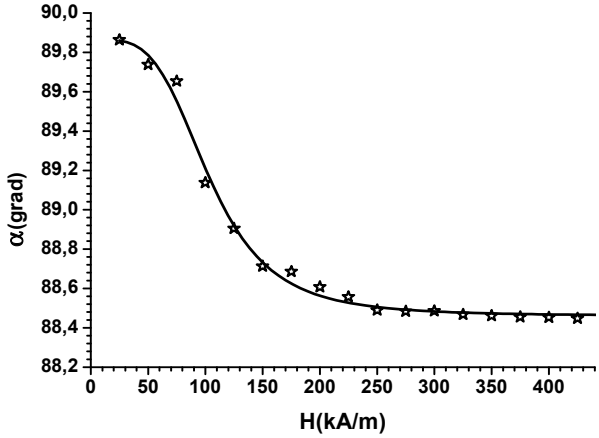

Fig. 4. The angle α between $\vec{H}$ and the direction of the dipoles columns $\vec{m}$ as a function of the longitudinal strength magnetic field H.

CONCLUSIONS

- Anisotropic MRE was obtained by magnetic field polymerization of the mixture formed by silicone rubber with catalyst and magnetorheological suspension based on silicone oil and Fe nanoparticles;
- The electric capacitance *C* of the plane capacitor with the MRE, the magnetic field – induced linear strain *e* and the stress σ depend on the strength and direction of $\vec{H}$;
- The magnetic Young modulus *E* of the MRE is strongly influenced by $\vec{H}$;
- The angle α between by $\vec{H}$ and the direction of the chains formed by iron particles decreases rapidly within the field range *20 ≤H(kA/m) ≤240* and becomes constant for higher field values.

REFERENCES

1. Yu L. Raikher, O.V. Stolbov, and G.V. Stepanov*, J. Phys. D: Appl. Phys*. 41, 152 002 (2008).
2. X. Zheng, S. Peng, W. Wen, and W. Li, *Smart Matter. Struct*. 17, 045001 (2008).
3. M. Farshad, and A. Benine*, Polymer Testing*, 23, 347 (2004).
4. G.V. Stepanov, D. Yu Borin, Yu L. Raikher, P.V. Melenev, and N.S. Peron, *J Phys.: Condens. Matter.* 20, 04121 (2008).
5. M.J. Hato, H.J. Choi, H.H. Sim, B.O. Park, and S.S. Raj, *Colloids and Surfaces A*: 377, 103 (2011).
6. B.O. Park, B.J. Park, M.J. Hato, and H.J. Choi, *Colloid and Polymer Science* 289, 387 (2011).
7. I.Bica, *J. Ind. Eng. Chem*. 12, 501 (2006).
8. Y.Fan, X. Gong, S. Xuan, W. Zhang, J. Zheng, and W.Jiang, *Smart Matter. Struct*. 20, 035007 (2011).
9. J.–H. Kov, F. Khan, D.–D. Jang, and H.–J. Jung, *Smart. Matter. Struct.* 19, 117002 (2010).
10. N. Huang, N. Zhang, and H. Du, *Smart Matter. Struct*. 20, 015019 (2011).
11. A. Ercuta, *J. Phys.: Cond. Matter*, 20, 325227 (2008).
12. A. Ercuta,I. Mihalca, *J. Phys. D-Applied Physics* 35, 2902 (2002).
13. A. Ercuta, I. Mihalca, *Defects and diffusion in metals: An annual retrospectives,* 203-2, 269 (2002).
14. K.M. Popp, X.Z. Zhang, W.H. Li, and P.B. Kosasih, *J. Phys. Conf. Ser*. 149, 012095 (2011)
15. N. Kchit, and G. Bossis*, J. Phys. D: Appl. Phys*. 42, 105505 (2010).
16. X. Zhu, Y. Meng, and Yu Tian, *Smart Matter. Struct*. 19, 117001 (2010).
17. I. Bica, *J. Ind. Eng. Chem*. 15, 773 (2009).
18. I. Bica, *J. Ind. Eng. Chem*. 16, 359 (2010).
19. I. Bica, *Mat. Letter*. 63, 2230 (2009).
20. I. Bica, *Mat. Sci. Eng. B* 166, 94 (2010).
21. I. Bica, *J. Ind. Eng. Chem*. 17, 83 (2011).
22. I.Bica, *J. Ind. Eng. Chem*. 18, 483 (2012).
23. I. Bica, *J. Ind. Eng. Chem*. 15, 605 (2009).
24. A.E. Green, and W. Zerna, *Theoretical Elasticity,* Second edition, Oxford University Press, London (1992).
25. S. Melle, Ph. D Thesis, Universidad de Madrid, Madrid (2002).
26. C. Bellen and G. Bossis, *Int. J. Mod. Phys. B* 16, 2447 (2002).
27. J. Paletto, Ph. D. Thesis, L'Université Claude-Bernard Lyon, Lyon (1972).
28. L. Borcea, and O. Bruno, *J. Mech. Phys. Solids*. 49, 2877 (2001).
29. H.M. Yin, L.Z. Sun, and J.S. Chen*, J. Mechanics Phys. of Solids* 54, 976 (2006).

STUDIA UBB PHYSICA, Vol. 60 (LX), 1, 2015, pp. 53-60
(RECOMMENDED CITATION)

Dedicated to Academician Professor Dr. Emil Burzo on His 80th Anniversary

THERMOLUMINESCENCE PROPERTIES OF THE $0.5P_2O_5$ - xBaO - $(0.5\text{-}x)K_2O$ GLASS SYSTEM. A POSSIBLE DOSIMETRIC MATERIAL

C. IVASCU[1], I.B. COZAR[2], A. TIMAR-GABOR[3], O. COZAR[1]*

ABSTRACT. Thermoluminescence (TL) properties of freshly β irradiated phosphate glasses doped with BaO and K_2O oxides at various concentrations were investigated. Barium-doped glasses ($0.5P_2O_5$ - 0.5BaO) show two TL peaks centered at 180 ^{0}C and 380 ^{0}C due to the defects generated by modifier Ba^{2+} ions inserted into the glass network. In the case of potassium-doped glasses ($0.5P_2O_5$ - $0.5K_2O$) an intense TL peak at 280 ^{0}C with an weak shoulder at 150 ^{0}C appear. The TL emission of the other phosphate glasses, $0.5P_2O_5$ - xBaO - $(0.5\text{-}x)K_2O$ with $0.1 \leq x \leq 0.4$, containing both type of the network modifier ions (K^+, Ba^{2+}) consist from the overlap of the above – mentioned luminescence spectra depending on the local energetic level diagrams of the luminescence centers. A linear dependence ($R^2 > 0.99$) of the integral TL signals with the absorbed doses were evidenced for all the investigated glasses which can be considered as good materials for dosimetry in the 0 – 50 Gy range.

Keywords: *P_2O_5 - BaO – K_2O glasses, TL dosimetry*

INTRODUCTION

Radiation dosimetry with solid luminescent materials is a well-established technique of monitoring ionizing radiation. Successful applications of thermoluminescence (TL) dosimetry are a result of search for materials that can be used as detectors of ionizing radiation and analysis of their properties [1].

[1] *Faculty of Physics, Babes-Bolyai University, Kogalniceanu 1, 400084 Cluj-Napoca, Romania*
[2] *National Institute for Research and Development of Isotopic and Molecular Technologies, 65-103 Donath, 400293 Cluj-Napoca, Romania*
[3] *Faculty of Environmental Science, Babes-Bolyai University, Fantanele 30, 400294 Cluj-Napoca, Romania*
** Corresponding author e-mail: onuc.cozar@phys.ubbcluj.ro*

Inorganic crystals such as LiF: Mg, Ti and LiF: Mg, Cu, P have been traditionally used for gamma and X-ray TL dosimetry applications. Various TL materials are in use today as dosimeters; however, as far as optically stimulated luminescence (OSL) is concerned, Al_2O_3:C is virtually the only synthetic material currently used in medical, environmental and personal dosimetry [2]. OSL has certain advantages over TL, such as higher precision, flexibility and ease of use, as well as the possibility of performing real-time measurements and future dose reassessments, if desired.

Extensive research is underwayto introduce new dosimetric systems into traditional in-phantom measurements, mailed dosimetric services for radiotherapy beam calibrations and two-dimensional TL dosimetry. Promising solutions are also being developed for online in-vivo dosimetry using OSL systems [3].

TL and OSL glass dosimeters are of particular interest because of their optical transparency, which results in an overall improvement of the efficiency of phosphor. Other characteristics that make them very suitable are their relatively simple preparation, easy shaping and long-term stability. Due to these advantages many studies have been dedicated to investigation and improvement of luminescent properties of glass systems [4-9].

Thus the effect of the Fe_2O_3 concentration on the TL properties of PbO–Sb_2O_3–As_2O_3 glasses in the light of different oxidation states of iron ions has been reported in the paper [10]. Also the Judd–Ofelt theory has been successfully used to characterize the absorption and luminescence spectra of Tb^{3+} ions in BaO–M_2O_3(M = Ga, Al, In)–P_2O_5 glasses [11, 12].

The thermoluminescence effect of the MgO at different concentrations on the B_2O_3-Li_2O glass system and TL properties of Cu-doped lithium potassium borate glasses have been reported in the papers [13] and [14], respectively.

The recent investigation of the Sm^{3+} - doped cadmium borate glass shown that this can be considered as a possible TL – dosimeter [15]. The Dy^{3+} - doped of alkali – silicate glasses [16] and of lithium magnesium borate glasses [17] suggested that these materials can be also used in radiation dosimetry measurements.

This paper presents the results of an investigation of TL properties of the $0.5P_2O_5$-xBaO-$(0.5–x)K_2O$ glass systems ($0.1 \leq x \leq 0.4$) undertaken to evaluate their usability as luminescence dosimetric materials.

EXPERIMENTAL

Starting materials to obtain the $0.5P_2O_5$-xBaO–$(0.5–x)K_2O$ glass systems with $0.1 \leq x \leq 0.4$ were reagent grade $(NH_4)_2HPO_4$, $BaCO_3$ and K_2CO_3. The samples were prepared by mixing powders of the components in suitable proportions and melting the mixture in sintered corundum crucibles at 1200 ^oC for 1h. The mixtures

were put into a furnace already stabilized at this temperature. The obtained glass samples were quenched by pouring the molten glass onto a stainless steel plate. The obtained transparent, homogenous and color-free glass pellets with a thickness of 1 mm were used in the experiments.

All TL signals were recorded at a controlled heating rate of 5 $^oC/s$ in nitrogen atmosphere with a RISØ TL/OSL DA-20 machine. Luminescence emissions have been detected using a bialkali EMI 9235QA photomultiplier tube using a HoyaU-340 filter (transmission between 290 and 390nm).

Irradiations were carried out at room temperature in a homogenous field of a ^{60}Co gamma source with a dose rate of 5.2Gy/h or individually and automatically in the luminescence reader using a $^{90}Sr–^{90}Y$ beta source with a dose rate of 0.05 Gy/s and which had been preliminarily calibrated against the gamma source.

RESULTS AND DISCUSSION

TL glow curves recorded at a controlled heating rate (5 $^oC/s$) immediately after β - irradiation to 25Gy are shown in Fig.1. No TL signals appear in the simple phosphate glass (P_2O_5). In the case of freshly irradiated $0.5P_2O_5$ - 0.5BaO glass, a narrow peak centered at 180 ^oC and also a broad intense peak in vicinity of 380 ^0C can be observed. An intense TL peak centered around 280 ^0C with an weak shoulder at 150 ^0C appear in $0.5P_2O_5$ - $0.5K_2O$ glass.

The differences between TL spectra of the two types of phosphate glasses may be attributed to the differences which appear in the energetic level diagrams of luminescent centers (defects) generated by the modifier ions (Ba^{2+}, K^+) inserted into the phosphate glass network.

TL glow curves of the mixed $0.5P_2O_5$ – xBaO - $(0.5–x)K_2O$ glasses with $0.1 \leq x \leq 0.4$ consist from the overlapping of the above-mentioned peaks. In the case of glasses containing both modifiers ions (Ba^{2+}, K^+) the structures of energetic levels characteristics to luminescent centers are changed and thus also the positions of luminescent peaks. The shapes of luminescent spectra are conditioned by the realized local structure of inserted cations (Ba^{2+}, K^+) and proper energetic level diagrams of luminescent centers in phosphate network. The local structural changes of these glasses with different Ba^{2+}, K^+ ions content are also evidenced by FT-IR and FT-Raman measurements. These results are in progress and will be published.

TL glow curves after freshly irradiated with $^{90}Sr – ^{90}Y$, integral TL output as function of the absorbed dose and reproductibility tests after 10 measurement cycles when the sample was gamma irradiated of 10 Gy dose and then immediately heated to 500 ^oC for barium – phosphate, potassium – phosphate and mixed (Ba, K) phosphate glasses are shown in Figs. 2, 3.

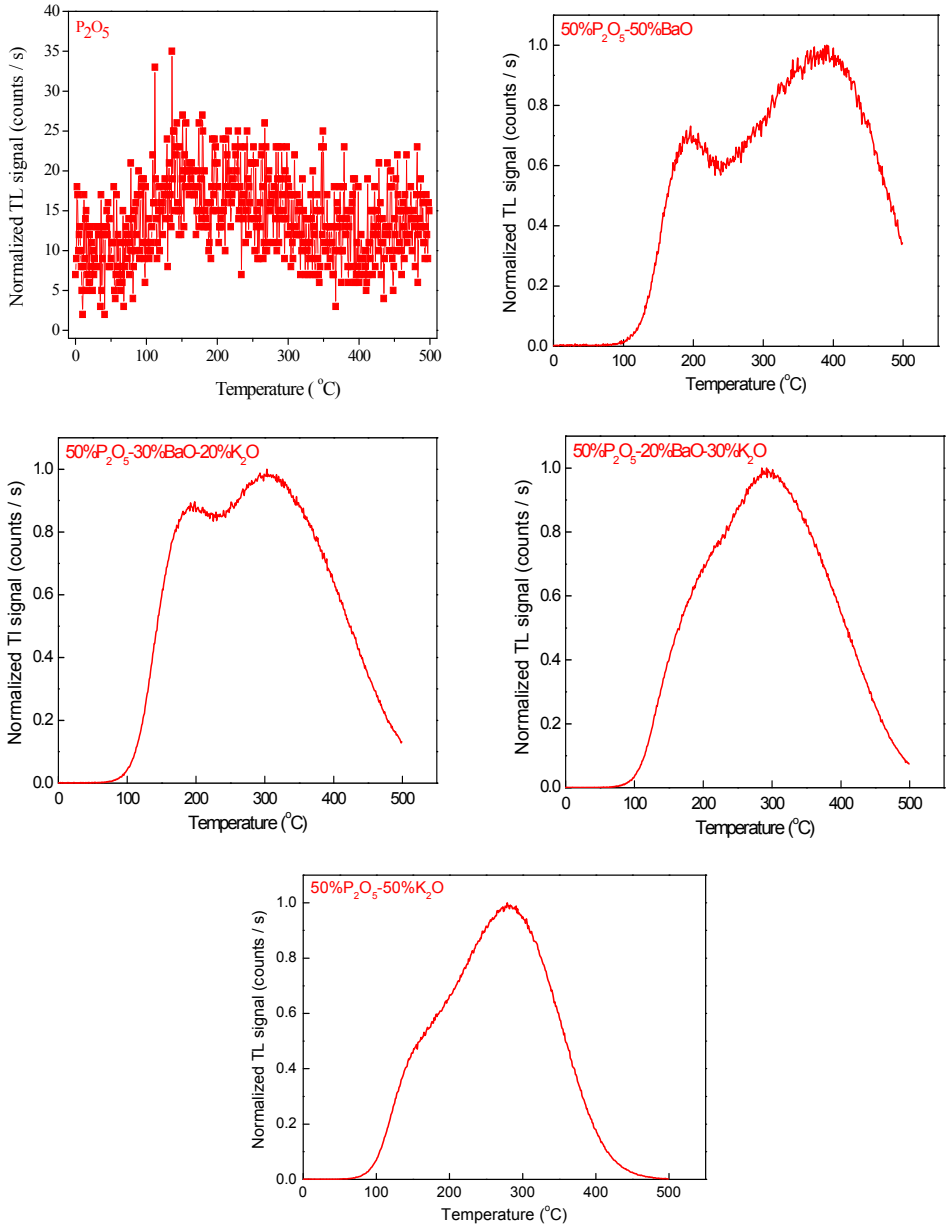

Fig. 1. TL glow curves of the P_2O_5 – BaO – K_2O glass system.

All measurements were performed with a single aliquot of each glass specimen because it had been observed that the process of recording the TL signal (ramp heating to 500 °C) reduces all signals to a negligible level (3% of the response recorded after an irradiation to 10 Gy).

Phosphate glass doped with barium oxide is at least one order of magnitude more sensitive to radiation than the glass doped with potassium oxide. An analysis of twelve aliquots showed that intensity ofthehigh-temperature peak produced by a 1-g portion of $0.5P_2O_5$–0.5BaO is about 50 times lower than the intensity produced by the traditional LiF:Mg, Ti(TLD100) pellet irradiated to the same dose and measured with the same setup.

However, very good linear dependences ($R^2 > 0.99$) of the integral TL signals can be observed for both dosimetric peaks of $0.5P_2O_5$ - 0.5BaO up to 50Gy (Fig. 2). The linear response at doses above 10Gy is a common characteristic of many TL materials what are very attractive for high-dose measurements [18].

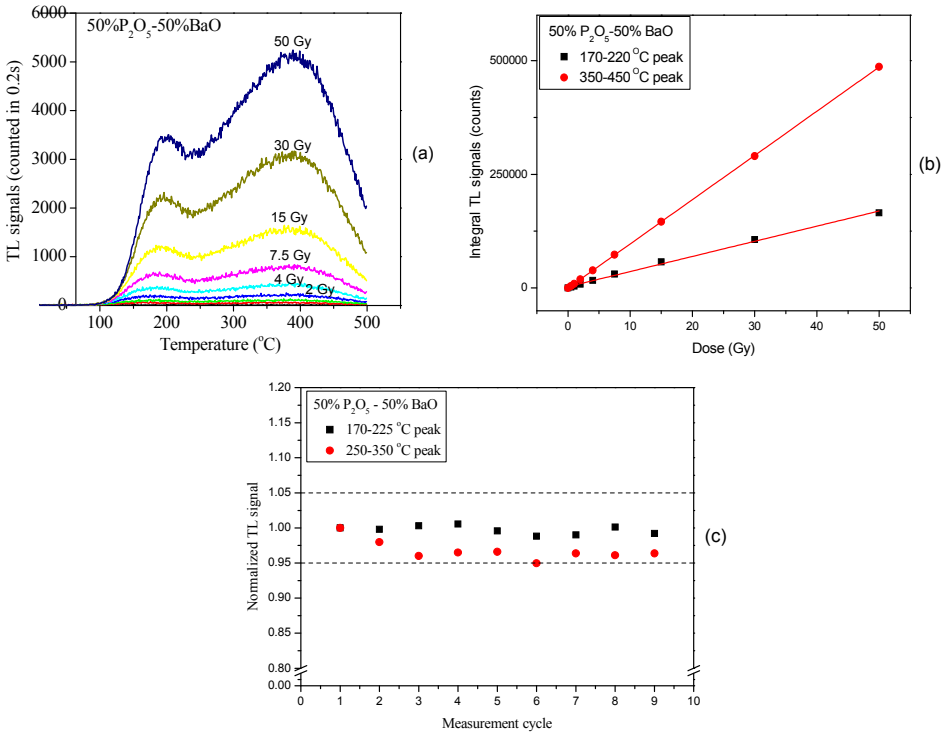

Fig. 2. Responses of β - irradiated $0.5P_2O_5$ – 0.5BaO glass: (a) – TL glow curves after freshly irradiation with ^{90}Sr – ^{90}Y; (b) – Integral TL output as a function of the adsorbed dose; (c) – Reproductibily tests after 10 measurement cycles when sample was gamma irradiated of 10Gy dose and then immediately heated to 500°C.

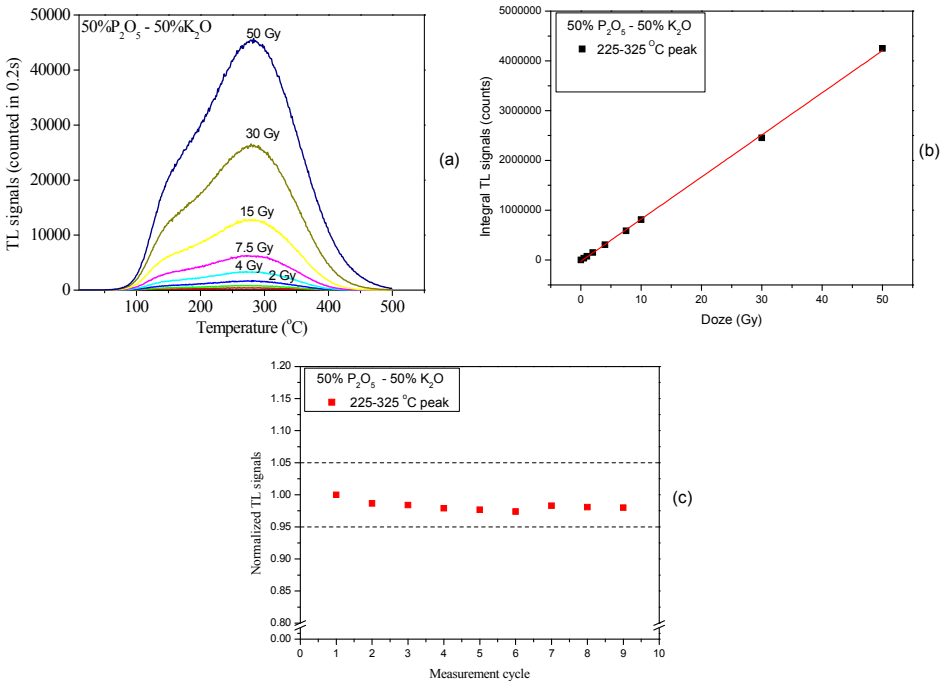

Fig. 3. Responses of β - irradiated $0.5P_2O_5 – 0.5K_2O$ glass: (a) – TL glow curves after freshly irradiation with $^{90}Sr – ^{90}Y$; (b) – Integral TL output as a function of the adsorbed dose; (c) – Reproductibily tests after 10 measurement cycles when sample was gamma irradiated of 10Gy dose and then immediately heated to 500°C.

An analogous dependence of the integral TL signals on the absorbed dose was also found in the case of $0.5P_2O_5–0.5K_2O$ (Fig.3) and $0.5P_2O_5$ - 0.3BaO - $0.2K_2O$ glasses. This might be an indication that the mechanism of the underlying luminescence process can be described by the first-order kinetics [19].

Reproducibility tests were also performed with 12 aliquots, each one repeatedly gamma irradiated of 10 Gy and then immediately heated to 500 °C over the course of 3 months for each type of the investigated glasses. Figs (2c-3c) show the average behavior of 12 aliquots over 10 measurement cycles. None of the investigated aliquots showed a pronounced sensitization or desensitization trend.

To estimate the threshold dose and the minimal detectable dose, we recorded the TL signals from a set of 10 unirradiated glass samples. The threshold dose D_0 was calculated as $D_0 = (B + 2\sigma_B)F$, where F is the calibration factor expressed in Gy/TL, B is the mean TL signal obtained for the background and σB is the standard deviation of

the background signal. For the high-temperature peak, a value of 0.2Gy was obtained. The low limit of detection for this peak was estimated to be 0.4Gy at 95% confidence level according to Eq.(8) in the paper [20].

CONCLUSIONS

Thermoluminescence properties of the investigated glsses depend on the relative ratio content of the incorporated network modifiers oxides (BaO, K_2O).

Two TL peaks centered at 200°C and 400°C were observed for $0.5P_2O_5$ – 0.5BaO glass, and only an intense TL peak at 280°C with an weak shoulder at 150°C appear in the case of $0.5P_2O_5$ – $0.5K_2O$glass.

TL emissions of the other phosphate glasses containing both type of detects generated by modifier Ba^{2+}, K^+ ions consist from the overlap of the above – mentioned luminescence spectra.

All the investigated glasses can be considered as good materials for dosimetry until 50 Gy due to the linear dependence ($R^2 > 0.99$) of the integral TL signals with the absorbed doses.

REFERENCES

1. V. Kortov, *Radiation Measurements,* 42, 576 (2007)
2. E.M. Yoshimura, E.G. Yukihara, *Nucl. Instrum. Methods Phys. Res.*, B 250, 337 (2006)
3. P. Olko, *Radiat. Meas.*, 45, 506 (2010)
4. B.L. Justus, T.L. Johnson, A.L. Huston, *Nucl. Instrum. Methods Phys. Res.*, B 95, 533 (1995)
5. M.I. Teixeira, Z.M. Da Costa, C.R. Da Costa, W.M. Pontuschka, L.V.E. Caldas, *Radiat. Meas.*, 43, 480 (2008)
6. P. Narayan, K.R. Senwar, S.G. Vaijapurkar, D. Kuman, P.K. Bhatnagar, *Appl. Radiat. Isot.*, 66, 86 (2008)
7. E.M. Yoshimura, C.N. Santos, A. Ibanez, A.C. Hernandes, *Opt. Mater.*, 31, 795 (2009)
8. A. El-Adawy, N.E. Khaled, A.R. El-Sersy, A. Hussein, H. Donya, *Appl. Radiat. Isot.*, 68, 1132 (2010)
9. W.E.F. Ayta, V.A. Silva, N.O. Dantas, *J. Lumin.*, 130, 1032 (2010)
10. B.V. Raghavaiah, P. Nageswara Rao, P. Yadgiri Reddy, N. Veeraiah, *Opt. Mater. 29*, 566 (2007)
11. S.V.G.V.A. Prasad, M. Srinivasa Reddy, V. Ravi Kumar, N. Veeraiah, *J. Lumin.*, 127, 637 (2007)
12. X.F. Meng, Q.T. Zhang, C.H. Lu, Y.R. Ni, Z.Z. Xu, J. Funct. Mater., 36, 270 (2005)
13. M.M. Elkholy, *J. Lumin.*, 130, 1880 (2010)

14. H. Aboud, H. Wagiran, R. Hussin, H. Ali, Y. Alajerami, M.A. Saeed, *Appl. Rad. Isot.*, 90, 35 (2014)
15. J. Anjaiah, C. Laxmikanth, N. Veeraiah, P. Kistaiah, *Mat. Sci. – Poland*, 33(1), 144 (2015)
16. R. Laopaiboon, C. Bootjomchai, *J. Lumin.*, 158, 275 (2015)
17. M.H.A. Mhareb, S. Hashim, S.K. Ghoshal, Y.S.M. Alajerami, M.A. Saleh, N.A.B. Razak, S.A.B. Azizan, *Luminescence*, DOI 10.1002/bio.2902 (2015)
18. C. Furetta, M. Prokic, R. Salamon, V. Procik, G. Kitis, *Nucl. Instrum. Methods Phys. Res. A*, 456, 411 (2001)
19. R. Chen, In: Proceedings of the IRPA Regional Congress on Radiation Protection in Central Europe, Dubrovnik, Croatia, May 20-25, 2001, 2o-01, 1-8 ISBN 953-96133-3-7
20. C.R. Hirning, *Health Physics*, 62, 223 (1992)

STUDIA UBB PHYSICA, Vol. 60 (LX), 1, 2015, pp. 61-72
(RECOMMENDED CITATION)

Dedicated to Academician Professor Dr. Emil Burzo on His 80th Anniversary

MODELING OF CRYSTAL FIELD PARAMETERS AND ENERGY LEVELS SCHEME SIMULATION FOR Fe^{6+} DOPED IN K_2MO_4 (M= Cr, S, Se)

M.G. BRIK[1,2,3,4], E.-L. ANDREICI[5] AND N.M. AVRAM[5,6*]

ABSTRACT. In this paper we report the results of a detailed comparative crystal field analysis of the crystal field parameters and energy level schemes, for all three above mentioned materials. The crystal structure data was used to calculate the crystal field parameters in the framework of exchange charge model using the Symmetry Adapted Axis System centered at the impurity ion. A thorough consideration of the impurity center symmetry was performed and the calculated crystal field parameters were used to diagonalize the crystal field Hamiltonian for each system. Energy levels obtained in this way were compared with the corresponding experimental data to yield good agreement between the theoretical and experimental results.

Keywords: *Fe^{6+}, K_2SO_4, K_2CrO_4, K_2SeO_4, crystal field parameters, energy levels.*

INTRODUCTION

Crystals doped with transition metal ions V^{3+}, Cr^{4+}, Mn^{5+}, Fe^{6+} (all of them have the $3d^2$ electron configuration) were, over the last years, the subject of systematic studies because of their potential applications as solid-state laser active media and electro optical devices [1, 2]. After doping, these ions usually occupy the sites with tetrahedral coordination, which can be described in terms of either low (V^{3+}, Cr^{4+}) or

[1] *College of Sciences, Chongqing University of Posts and Telecommunications, Chongqing 400065, P.R. China*
[2] *Institute of Physics, University of Tartu, Ravila 14C, Tartu 50411, Estonia*
[3] *Institute of Physics, Polish Academy of Sciences, Al. Lotnikow 32/46,Warsaw 02-668, Poland*
[4] *Institute of Physics, Jan Dlugosz University, Armii Krajowej 13/15, PL-42200 Czestochowa, Poland*
[5] *Department of Physics, West University of Timisoara, Bd. V. Parvan, No. 4, 300223, Timisoara, Romania*
[6] *Academy of Romanian Scientists, Independentei 54, 050094-Bucharest, Romania*
** Corresponding author e-mail: avram@physics.uvt.ro*

strong (Mn^{5+}, Fe^{6+}) crystal field [2]. Speaking about the ferrate (VI) ion, it is worth noting that it is perfectly stabilized in well-defined tetrahedral oxo coordination. Experimentally the absorption and luminescence spectra of Fe^{6+} ion in the K_2MO_4 (*M*= Cr, S, Se) crystals have been investigated [1, 3-5], including the Fe^{6+} excited states properties [4]. Wagner *et al* [6] studied the EPR spectra of the single crystals and powders with an aim of getting a better insight into the properties of the Fe-O bond and the site geometry of the FeO_4 polyhedral in various hosts. The density functional theory (DFT)-based study of the optical excitations and coupling constants in FeO_4 ion was reported in Ref. [7], and *ab initio* study of the absorption properties of the same complex can be found in Ref. [8].

However, until now no satisfactory and unified theoretical description and explanation for optical spectral data regarding title systems, in the framework of the crystal field theory wasn't offered. Previously, both experimental [1,4,5] and theoretical [7,8] papers have not used the actual C_s site symmetry of the Fe^{6+} centers, but the C_{3v} and T_d site symmetries, respectively. Therefore, in this paper we try to fill in this gap by reporting a detailed analysis of crystal field effects, modeling of the crystal field parameters (CFPs) and simulations of the energy level schemes for Fe^{6+} ion in three crystals K_2CrO_4, K_2SO_4 and K_2SeO_4, respectively.

The CFPs were modeled in the framework of the exchange charge model (ECM) of crystal field (CF) [9], using the actual crystal structure data in the Symmetry Adapted Axis System (SAAS) [10]. Application of the ECM implies knowledge of the overlap integrals between the *d*-functions of central ion and *s*, *p* functions of the ligands, which were calculated numerically with the wave functions from Ref. [11]. With the obtained CFPs we calculated the Fe^{6+} energy levels by diagonalizing the CF Hamiltonians of considered doped systems. The obtained results are discussed; quite satisfactory agreement with the experimental data [1, 4] was obtained.

SYMMETRY OF CRYSTALS

At room temperature, $K_2(M)O_4$ (M= Cr, S, Se) crystallizes in the orthorombic D_{2h}^{16}(Z=4) space group (number 62 in International Tables for Crystallography [12]), with α=β=γ=90° and a=7.663 Å, b=10.388 Å, c=5.922 Å for M=Cr [13], a=5.7704 Å, b=10.0712 Å, c=7.4776 Å, for M=S [14] and a=7.66 Å, b=6.00 Å, c=10.47 Å for M=Se [15], respectively (see Fig. 1).

It is essential that the Fe^{6+} ions in all considered K_2MO_4 crystals isovalently substitutes the M^{6+} ions, so no need for the charge compensation. The $[FeO_4]^{2-}$ cluster has the C_s site symmetry at room temperature. Under 93 K the K_2SeO_4 crystal has ferroelectric phase, with space group $Pna2_1$ (C_{2v}^9, Z=12) - number 62 in International Tables for Crystallography [12]). In this phase the parameters of the unit cell are α=β=γ=90°, a=22.716 Å, b=10.339 Å, c=5.967 Å, with the C_1 actual site symmetry of Fe^{6+} doped in K_2SeO_4 [16].

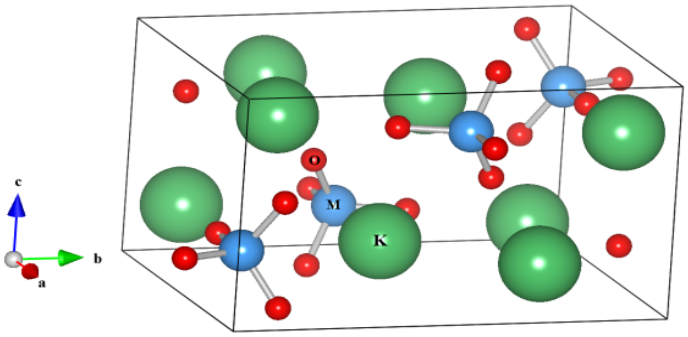

Fig. 1. One unit cell of K_2MO_4 (M= Cr, S, Se). The M ions are shown by the blue spheres tetrahedral coordinated by oxygen ions (red spheres) and K^+ ion are shown the by green spheres.

DESCRIPTION OF THE METHOD USE IN CALCULATIONS

In the present work for calculations of the CFPs we use ECM [9] of crystal field which is briefly described below.

In its framework the actual C_s (K_2CrO_4, K_2SO_4) respectively C_1 (K_2SeO_4) site symmetries of the ferrate (VI) ion, in three different host matrices, is considered. It is well known that in the frame of ECM, the crystal field Hamiltonian of the system will be written as [9]:

$$H = \sum_{p=2,4} \sum_{k=-p}^{p} B_p^k O_p^k \tag{1}$$

where O_p^k are the linear combinations of irreducible tensor operators acting on angular parts of the 3d-ion wave functions, and B_p^k are the CFPs containing all information about geometrical arrangement of the ligands around the central ion. Following Ref. [9], these parameters can be written as a sum of two terms:

$$B_p^k = B_{p,q}^k + B_{p,S}^k \tag{2}$$

The former contribution originates from the electrostatic interaction between valence electrons of an impurity ion and ions of crystal lattice, whereas the latter is proportional to the overlap of the wave functions of an impurity ion and ligands; it includes effects of the covalent bond formation and exchange interaction. Inclusion of these effects significantly improves agreement between the calculated and experimentally observed energy levels. Analytical expressions for calculating both contributions to the CFP in the case of 3*d*-ion are as follows [9]:

$$B^k_{p,q} = -K^k_p e^2 \left\langle r^p \right\rangle \sum_i q_i \frac{V^k_p(\theta(i),\varphi(i))}{R(i)^{p+1}} \tag{3}$$

$$B^k_{p,S} = K^k_p e^2 \frac{2(2p+1)}{5} \sum_i \left(G_s S_s(i)^2 + G_\sigma S_\sigma(i)^2 + \gamma_p G_\pi S_\pi(i)^2 \right) \frac{V^k_p(\theta(i),\varphi(i))}{R(i)} \tag{4}$$

Eq. (3) describes the point charge contribution to the CFP, which appears due to electrostatic interaction between the central ion and the lattice ions enumerated by index *i* with charges q_i and spherical coordinates R_i, θ_i, φ_i (in the reference system centered at the impurity ion itself). The averaged values $\left\langle r^p \right\rangle$, where *r* is the radial coordinate of the *d* electrons of the impurity ion, can be obtained either from the literature or calculated numerically, using the radial parts of the corresponding ion's wave functions. The values of the numerical factors K^k_p, γ_p, the expressions for the polynomials V^k_p and the definitions of the operators O^k_p can all be found in Ref. [9]; for the sake of brevity, they are not given here. Eq. (4) determines the so called exchange charge contribution to the CFPs; it is proportional to the overlap between the wave functions of the central ion and ligands and thus includes all covalent effects. The $S(s), S(\sigma), S(\pi)$ entries correspond to the overlap integrals between the *d*-functions of the central ion and *p*- and *s*-functions of the ligands $S(s) = \langle d0 | s0 \rangle, S(\sigma) = \langle d0 | p0 \rangle, S(\pi) = \langle d1 | p1 \rangle$. The G_S, G_σ, G_π coefficients are dimensionless adjustable parameters of the model, whose values are determined from the positions of the first three absorption bands in the experimental spectrum. They can be approximated to a single value, i.e. $G_s = G_\sigma = G_\pi = G$, which then can be estimated from one absorption band only (the lowest in energy). This is usually a reasonable approximation [9]. The overlap integrals, which enter the above-given equations, correspond to the Fe^{6+}-O^{2-} wave functions overlaps, were calculated numerically, taking the wave functions from Ref. [11]. For a further convenience of use, they were approximated by the following exponential functions of the Fe^{6+}-O^{2-} distance *R* (expressed in a. u.) [17]:

$$\begin{aligned} S(s) &= \langle d0 | s0 \rangle = -0.71931 \ \exp(-0.88026 \ R) \\ S(\sigma) &= \langle d0 | p0 \rangle = 0.68957 \ \exp(-0.81694 \ R) \\ S(\pi) &= \langle d1 | p1 \rangle = 1.2686 \ \exp(-1.1485 \ R) \end{aligned} \tag{5}$$

The ECM has been successfully applied to numerous crystals doped with the transitional metal ions; more further details can be found in Refs. [17-22 and references therein].

CALCULATIONS OF THE CFPs

Using the crystal structure data from Refs. [13,14,16], we generated large clusters consisting of 15876 ions in K_2CrO_4, 27999 ions in K_2SO_4 and 37632 ions in K_2SeO_4, which include all ions of crystal lattice located at the distances up to 61.814 Å, 69.336 Å and 76.920 Å respectively, from the impurity ion. Such clusters are needed to achieve proper convergence of the crystal lattice sums, in ECM, especially those ones of the second rank, which depend on the distance R as $1/R^3$, and, as such, converge very slowly. Table 1 below collects the calculated values of CFPs for all considered systems. To illustrate the role and significance of the exchange charge contribution (ECC) in comparison with that one of the point charge contribution (PCC) both contributions to the total CFPs, are shown separately.

Table 1. CFPs (Stevens normalization) and Racah parameters *B*, *C* (all in cm^{-1}) for $K_2MO_4:Fe^{6+}$ (*M*= Cr, S, Se). *G* is the dimensionless ECM parameter.

CFPs	K_2CrO_4			K_2SO_4			K_2SeO_4		
	PCC	ECC	Total value	PCC	ECC	Total value	PCC	ECC	Total value
B_2^{-2}	42	74	116	206	333	539	-1309	-2939	-4248
B_2^{-1}	-	-	-	-	-	-	-1971	-7513	-9484
B_2^{0}	125	34	159	-25	-177	-202	-97	-745	-842
B_2^{1}	-	-	-	-	-	-	-1688	-5868	-7556
B_2^{2}	248	1077	1325	504	974	1478	-373	-1164	-1537
B_4^{-4}	795	7216	8011	-1241	-6051	-7292	1024	9922	10946
B_4^{-3}	-	-	-	-	-	-	1113	10573	11686
B_4^{-2}	1697	14934	16631	-2929	-13968	-16897	1324	12351	13675
B_4^{-1}	-	-	-	-	-	-	-654	-6457	-7111
B_4^{0}	86	790	876	150	731	881	46	463	509
B_4^{1}	-	-	-	-	-	-	853	8093	8946
B_4^{2}	-559	-5059	-5618	-875	-4238	-5113	-786	-7618	-8404
B_4^{3}	-	-	-	-	-	-	587	6060	6647
B_4^{4}	981	8959	9940	1778	8652	10430	660	6506	7166
G		18.393			9.961			19.752	
B		446.2			472.2			375	
C		1368.5			1278.3			1687.5	

It is seen that the ECC is, very often, greater than the PCC, which means the importance of the covalent effects against the point charge effect, in studied systems. It can be also noted that the ECM parameter *G* and the values of the exchange charge contribution to the CFPs (for the second rank CFPs especially) are considerably greater for K_2CrO_4 and K_2SeO_4.

Before we proceed with the energy level analysis, we consider and compare the crystal field invariants N_v in each of the three considered hosts. This quantity can be viewed as a reliable qualitative measure of the crystal field strength defined as [23, 24]

$$N_v = \left[\sum_{p,k} \left(B_p^k \right)^2 \frac{4\pi}{2p+1} \right]^{1/2} \tag{6}$$

where the CFPs values B_p^k, p=2,4 and k= -p,-p+1,….,p-1,p, are taken in the Wybourne normalization. Relations between the Stevens and Wybourne normalizations for the crystal field parameters can be found in Ref. [25].

The values of N_v, calculated with the CFPs parameters from Table 1 are colected in Table 2.

Table 2. Values of N_v (all in cm^{-1}) for $K_2MO_4:Fe^{6+}$ (*M*= Cr, S, Se).

N_v	K_2CrO_4	K_2SO_4	K_2SeO_4
N_v-*ECM*	31116.8	48841.6	33088.0

The direction of decreased crystal field invariants, calculated in actual site symmetry, give the trends of decreasing of the field strength of the doped crystals.

CALCULATIONS OF THE Fe^{6+} ENERGY LEVEL SCHEMES

The energy levels of the Fe^{6+} impurity ion doped in crystals K_2MO_4 (*M*=S, Cr, Se) are considered as the eigenvalues CF Hamiltonian:

$$H = H_0(B,C) + H_{CF}\left(B_p^k\right) \tag{7}$$

The sequence of the energy levels of the Fe^{6+} cation with its $3d^2$ electron shell, in the tetrahedral coordination, is determined mainly by the crystal field splitting of the ^3F and ^1D terms. The ground state is the $^3A_2$ (^3F), whereas the lowest excited states are the ^1E (^1D) and $^3T_2$(^3F) states. The relative positions of these spin-singlet and spin-triplet states are strongly affected by the local geometry around impurity. The low-symmetry crystal field effects, which arise from the deviation of the

$[FeO_4]^{2-}$ cluster, from the ideal T_d symmetry, would produce additional splitting of the orbital triplet states and shift the energy levels. One of the main characteristic features of the $K_2MO_4:Fe^{6+}$ spectra is the presence of the sharp ^1E-$^3A_2$ radiative transition; in addition, the excited state absorption spectra from ^1E state can gives more information about location of the higher excited states.

The low lying energy level schemes of the $K_2MO_4:Fe^{6+}$ systems were calculated by diagonalizing the crystal field Hamiltonian (7), with CFPs from Tables 1, in the basis spanned by 25 wave functions of all 5 terms of the $3d^2$ electronic configuration of free Fe^{6+} ion. The obtained, in this way, energy levels are collected in Tables 3 along with the experimental data [1, 4].

Table 3. Energy levels (in cm^{-1}) of $K_2MO_4:Fe^{6+}$ (M= Cr, S, Se).

Energy levels (T_d group not.)	K_2CrO_4			K_2SO_4			K_2SeO_4		
	Calculated this work	Averaged	Observed [1, 4]	Calculated this work	Averaged	Observed [1, 4]	Calculated this work	Averaged	Observed [1, 4]
$^3A_2$	0	0	0	0	0	0	0	0	0
^1E	6212 6215	6214	6214	6219 6231	6225	6225	6170 6278	6224	6224
$^1A_1$	11582	11582	9119	11678	11678	9176	11598	11598	9104
	13164			13135			11659		
$^3T_2$	13167	13280	13280	13301	13332	13330	12443	13000	≈13000
	13510			13560			14899		
	17739			17917			17203		
$^3T_1$	17862	17931	17930	18086	18200	18200	18175	18422	≈17700
	18191			18597			19887		
	19237			19215			17293		
$^1T_2$	19295	19405	-	19464	19465	-	18045	18658	-
	19684			19717			20636		
	21218			21260			21420		
$^1T_1$	21240	21396	-	21415	21579	-	22809	22877	-
	21729			22062			24403		
	28105			28215			25913		
$^3T_1$	28643	28638	-	29224	28916	-	28644	29111	-
	29165			29309			32776		
^1E	33025 33031	33028	-	33081 33144	33113	-	29856 31391	30624	-
	33456			33888			34037		
$^1T_2$	33892	33758	-	33930	33991	-	36670	36098	-
	33926			34155			37588		
$^1A_1$	42516	42516	-	42617	42617	-	45777	45777	-

In addition, Fig. 2a, 2b and 2c visualizes correspondence between the experimental spectra and calculated energy levels.

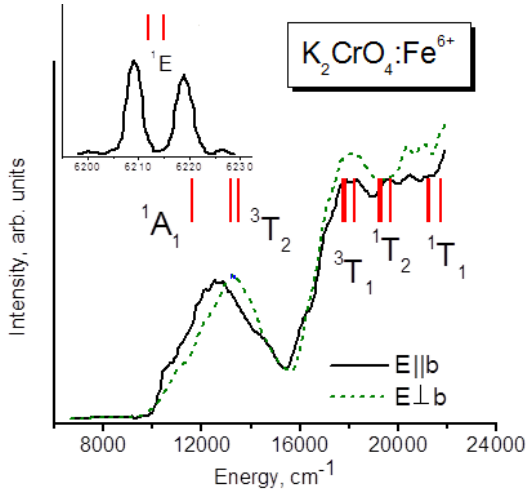

Fig. 2a. Experimental absorption spectra (solid lines) of $K_2CrO_4:Fe^{6+}$ and calculated Fe^{6+} energy levels (vertical lines) - adopted from [1].

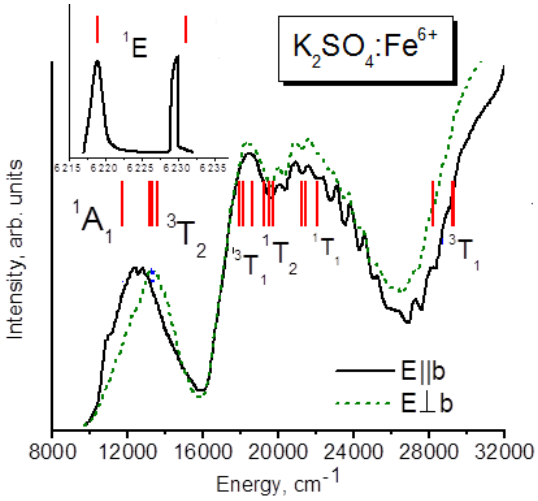

Fig. 2b. Experimental absorption spectra (solid lines) of $K_2SO_4:Fe^{6+}$ and calculated Fe^{6+} energy levels (vertical lines) - adopted from [4].

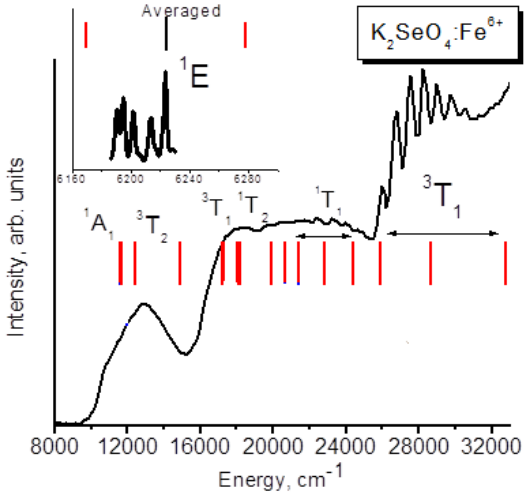

Fig. 2c. Experimental absorption spectra (solid lines) of $K_2SeO_4:Fe^{6+}$ and calculated Fe^{6+} energy levels (vertical lines) - adopted from [1].

All spectra are characterized by two prominent bands, which are due to the spin-allowed transitions $^3A_2 \rightarrow {}^3T_2(^3F)$ and $^3A_2 \rightarrow {}^3T_1(^3F)$, at about 13000 cm^{-1} and 18000 cm^{-1}, respectively. The latter one is mixed up with the spin-forbidden transitions to the $^1T_2$, $^1T_1$ states. A very weak absorption at about 6200 cm^{-1} is caused by the $^3A_2 \rightarrow {}^1E(^1D)$ transition.

We emphasize that application of the ECM with its calculations of all CFPs without any assumption about the impurity center symmetry allows for quantitative treatment of the low-symmetry crystal field effects, which is evidenced by the splitting of the orbital triplet and doublet states and complete removal of the degeneracy. The magnitude of this splitting is the largest in K_2SeO_4, where the splitting of the orbital triplets can be as large as ~7000 cm^{-1} for the $^3T_1(^3P)$ state (compare it with the splitting of just about 1000 cm^{-1} in the remaining two crystals).

When presenting the results, we give in the corresponding table the weighted averaged positions of all energy levels arising from the "parental" states of the T_d symmetry, which can be then directly compared to the experimental data from Ref. [1, 4]. On average, as is evidenced by Tables 3 and Fig. 2, agreement between these data is good. It can be noted that the calculated position of the $^1A_1$ state at about 11500 cm^{-1} is somewhat overestimated with respect to the experimental results [1, 4]; however, a similar overestimation was reported by the authors of Reference [4], after application of the angular overlap model.

Position of the $^3T_1(^3P)$ state at about 27000 - 28000 cm^{-1} is not shown in Fig. 2, since it is hidden by the strong charge transfer O^{2-} - Fe^{6+} transition.

As is known from the crystal field theory, the position of the $^3T_2(^3F)$ state of an ion with the d^2 configuration in the tetrahedral coordination determines the crystal field strength 10*Dq*. Collecting together the corresponding data for all considered crystals, we can arrange them in the order of the decreasing crystal strength as 10*Dq*(K_2SO_4)> 10*Dq*(K_2SeO_4)> 10*Dq*(K_2CrO_4), in full agreement with the direction of decreased crystal field invariants, calculated with the use of Eq. (6).

As it is well known [26], the Racah parameters *B* and *C* for transitional metal ions doped in different host matrices are significantly reduced with respect to those of free ion. To analyze this reduction, we introduce a non-dimensional quantity [27]

$$\beta = \sqrt{\left(\frac{B_1}{B_0}\right)^2 + \left(\frac{C_1}{C_0}\right)^2} \tag{8}$$

where subscripts "1" and "0" are related to the values of the Racah parameters in a host matrix and in a free state, respectively. This quantity can serve as a qualitative measure of the nephelauxetic effect in doped crystals. To calculate this parameter we need the values of the parameters B_0 and C_0 for free Fe^{6+} ion. These values B_0=1387 cm^{-1} and C_0=5292 cm^{-1} [28] have obtained by fitting the experimental values [29] of energy levels of free ferrate (VI) ion. With the relation (8), we obtained β = 0.412 for K_2CrO_4, β = 0.417 for K_2SO_4 and β = 0.418 for K_2SeO_4.Thus, the Fe^{6+}-O^{2-} bonds are more covalent in K_2CrO_4, less covalent in K_2SeO_4 with K_2SO_4 being between them.

CONCLUSIONS

In this paper we calculated the crystal field parameters for three K_2MO_4 crystals (*M*= Cr, S, Se) doped with Fe^{6+}. ECM of CF was used in the calculations, with takes into account the actual geometry of the impurity centers. With the obtained CFPs, the complete energy level scheme of the Fe^{6+} ions was calculated and comparison to the experimental absorption spectra yielded good agreement. The comparative analysis of the crystal field invariants and low symmetry crystal field effects (evidenced by the splitting of the orbital degenerated levels), was performed. The following trends were found: the crystal field strength decreases in the following sequence: $K_2SO_4 \rightarrow K_2SeO_4 \rightarrow K_2CrO_4$ (which agrees with the experimental absorption spectra), whereas the covalent effects are decreasing when going from K_2CrO_4 to less covalent in K_2SO_4 and, finally, K_2SeO_4. It was also demonstrated that proper description of the Fe^{6+} impurities in these crystals, including the CFPs, crystal field invariants, and splitting of the orbital degenerated states, requires knowledge and use of the actual symmetry of impurity centers.

ACKNOWLEDGMENT

M.G. Brik thanks the Programme for the Foreign Experts offered by Chongqing University of Posts and Telecommunications and the project PUT430 from Ministry of Education and Research of Estonia.

REFERENCES

1. T.C. Brunold, A. Hauser, H.U. Güdel, *J. Lumin*. 59, 321 (1994).
2. S. Kück, *Appl. Phys*. B72, 515 (2001).
3. L. Di Sipio, G. De Michelis, E. Baiocc, and G. Ingletto, *Transition Met. Chem*. 5, 164 (1980).
4. T.C. Brunold, H.U. Güdel, S. Kück and G. Hüber, *J. Lumin*. 65, 293 (1996).
5. D. Reinen, W. Rauw, U. Kesper, M. Atanasov, H.U. Gudel, M. Hazenkamp, U. Oetliker, *J. All. Comp*. 246, 193 (1997).
6. B. Wagner, D. Reinen, Th. C. Brunold and H.U. Gudel, *Inorg. Chem*. 34, 1934 (1995).
7. K. Wissing, M.T. Barriuso, J.A. Aramburu and M. Moreno, *J. Chem. Phys*. 111(22), 10217 (1999).
8. A. Al-Abdalla, L. Seijo and Z. Barandiaran, *J. Chem. Phys*. 109(15), 6396 (1999).
9. B.Z. Malkin, in A.A. Kaplyanskii, B.M. Macfarlane (Eds.), Spectroscopy of Solids Containing Rare-Earth Ions, North-Holland, Amsterdam, **1987**, p. 33.
10. C. Rudowicz, J. Qin*, J. Lumin*. 110, 39 (2004).
11. E. Clementi and C. Roetti, *Atomic Data and Nuclear Data Tables* 14, 177 (1974).
12. International Tables for Crystallography, Ed. T. Hahn, Vol. A, Springer Verlag, Berlin, **2006**, p. 298.
13. J.A. Mc Ginnety, *Acta Crystall*. B28, 2845 (1972).
14. K. Ojima, Y. Nishihata, A. Sawada, *Acta Crystall*. B51, 287 (1995).
15. R.W.G. Wyckoff, Crystal Structures, vol. 3, Interscience Publishers, Inc., New York, **1965**, p. 95.
16. N. Yamada, Y. Ono, and T. Ikeda, *J. Phys. Soc. Japan*, 53, 2565 (1984).
17. M.G. Brik, N.M. Avram and C.N. Avram Exchange charge model of crystal field for 3d ions, in: N.M. Avram and M.G. Brik (Eds), Optical Properties of 3d Ions in Crystals-Spectroscopy and Crystal Field Analysis, Tsinghua University Press, Springer, Beijing, Berlin, **2013**.
18. C. Jousseaume, D. Vivien, A. Kahn-Harari, B.Z. Malkin, *Opt. Mater*. 24, 143 (2003).
19. N.M. Avram, M.G. Brik, I.V. Kityk, *Opt. Mater.* 32**,** 1668 (2010).
20. M.G. Brik, C.N. Avram, *J. Lumin*. 131, 2642 (2011).
21. A.M. Srivastava, M.G. Brik, *J. Lumin.* 132, 579 (2012).
22. N. Mironova-Ulmane, M.G. Brik, I. Sildos, *J. Lumin.* 135**,** 74 (2013).
23. F. Auzel, O. Malta, *J. Phys.* 44**,** 201 (1983).
24. F. Auzel, *Opt. Mater.* 19, 89 (2002).
25. C. Rudowicz, *Mag. Res. Rev.* 13, 32 (1987).

26. B.N. Figgis, M.A. Hitchman, Ligand field theory and its application, Wiley-VCH, New York, **2000**, p 218.
27. M.G. Brik, N.M. Avram, C. N. Avram, *Physica* B371, 43 (2006).
28. E.-L. Andreici, A.S. Gruia, N.M. Avram, *Phys. Scr.* T149**,** 014060 (2012).
29. Yu Ralcenko, A.E. Kramida, J. Reader and NIST ASD Team (2011), *NIST Atomic Spectra Database* (ver. 5. 0), National Institute of Standards and Technology, Gaithersburg, MD, *http://physics.nist.gov/cgi-bin/ASD/energy1.pl*

STUDIA UBB PHYSICA, Vol. 60 (LX), 1, 2015, pp. 73-81
(RECOMMENDED CITATION)

Dedicated to Academician Professor Dr. Emil Burzo on His 80th Anniversary

NANOCRYSTALLINE MAGNETITE - Fe_3O_4 PARTICLES SYNTHESIZED BY MECHANICAL MILLING

T.F. MARINCA[1], H.F. CHICINAȘ[1], B.V. NEAMȚU[1], F. POPA[1], O. ISNARD[2,3], I. CHICINAȘ[1,*]

ABSTRACT. Nanocrystalline magnetite – Fe_3O_4 has been synthesized in nanocrystalline state by mechanical milling of well crystallized magnetite samples obtained by heat treatment of a stoichiometric mixture of iron and hematite. Upon increasing the milling time, the mean crystallite size of magnetite is diminishing. After only 5 minutes of mechanical milling the crystallites are 110 nm. The milling up to 120 minutes leads to a continuous reduction of crystallites size up to 8 nm. The mechanical milling process induces strains into the lattice and the lattice strains increase drastically in the first 60 minutes of milling, after that a saturation of lattice strains is noticed. During milling a contamination of the powder with elemental iron occurs for milling times larger than 30 minutes. A decrease of the saturation magnetisation is noticed upon increasing the milling time and the decrease is associated with the structural disorder and defects that are induced into the material during milling. A tendency of the magnetisation to become unsaturated is also noticed and it is related to canted spins effect.

***Keywords**: mechanical milling, magnetic material, ferrite, magnetite, nanocrystalline.*

INTRODUCTION

The iron oxides are of interest both for fundamental research and applicative research and are used in various fields of industry [1-3]. Among the iron oxides, the magnetite - Fe_3O_4 is probably the most studied nowadays. The magnetite crystallizes in

[1] *Materials Science and Engineering Department, Technical University of Cluj-Napoca, 103-105, Muncii Avenue, 400641 Cluj-Napoca, Romania*
[2] *Université Grenoble Alpes, Inst NEEL, F-38042 Grenoble, France*
[3] *CNRS, Institut NEEL, 25rue des martyrs, BP166, F-38042 Grenoble, France*
** Corresponding author e-mail: ionel.chicinas@stm.utcluj.ro*

cubic spinel structure from the space group Fd-3m. Typically, as almost all of the soft ferrites, the magnetite is ferrimagnetic having the Néel point at about 585 °C. The ferrimagnetism of the magnetite derives from the arrangement of the Fe^{2+} and Fe^{3+} cations into the spinel cubic structure that allows two type of positions: tetrahedral and octahedral. The Fe^{2+} cations and half of Fe^{3+} cations are positioned in the octahedral positions. The other half of Fe^{3+} cations are positioned in the tetrahedral positions. The octahedral positions create a magnetic sublattice aligned antiparallel to the other magnetic sublattice which is formed by the cations from tetrahedral positions [4].

The synthesis of the magnetite particles in nanocrystalline/nanosized state is nowadays a very challenging subject of research due to the large range of new potential applications, such as magnetic refrigeration, magnetic storage systems, magnetic separation, magnetic hyperthermia and cancer therapy [5-8]. There are several synthesis routes that can be used for obtaining magnetite particles in the nanocrystalline/nanosized state: solvothermal [9], co-precipitation [10], hydrothermal [11] or mechanosynthesis [12]. Among these routes, the mechanosynthesis is one of the most versatile approaches, which can be used for the synthesis of nanocrystalline magnetite particles and also magnetite nanoparticles. The nanocrystalline magnetite and magnetite nanoparticles can be obtained using a relatively large range of precursors.

The present paper investigates the structural and magnetic evolution of magnetite powder, obtained from iron and hematite by heat treatment, during mechanical milling processing.

EXPERIMENTAL

Iron and hematite (α-Fe_2O_3) powders have been used for the synthesis of the magnetite – Fe_3O_4 powder in nanocrystalline state. The first step of the synthesis consists in homogenising the iron and hematite powders in a Turbula type apparatus for 15 minutes. After that, the stoichiometric powder mixture has been heat treated at 870 °C for 4 h in argon atmosphere (in order to avoid the supplementary oxygen that can be provided by air). The second step consists in the mechanical milling of the magnetite powder obtained by heat treatment. A Fritsch high energy planetary ball mill, model Pulverisette 6, was used for the mechanical milling process. The mechanical milling process has been carried out in argon atmosphere and tempered steel vial and balls were used. A 350 rpm rotational speed was set. The milling process was carried out using a ball to powder mass ratio of 20:1.

An INEL Equinox 3000 diffractometer that works in reflection mode has been used for structural investigation of the powder. The X-ray diffraction patterns have been recorded in angular range of 2 theta = 20-110° using CoK_α radiation. The mean crystallite size and lattice strain were determined by Williamson-Hall method [13].

The magnetisation curves at room temperature have been recorded using extraction sample method in a continuous magnetic field up to 9 T. The saturation magnetisation values have been obtained according to the law of approach to saturation:

$$M = M_S \left(1 - \frac{a}{H} - \frac{b}{H^2}\right) + \chi H \quad (1)$$

The saturation magnetization values were obtained from $M=f(1/H^2)$ plots from the region of high external magnetic field, $\mu_0 H \geq 6$ T.

RESULTS AND DISCUSSION

Figure 1 presents X-ray diffraction patterns of the Fe_3O_4 samples milled for 0, 1, 5, 15, 30, 60 and 120 minutes. As reference, in the figure are given beside the peaks position of the iron and magnetite, the peaks position for the wüstite phase-FeO. This last oxide is encountered during processing Fe and magnetite. The JCPDS files no. 06-0696 for Fe, no. 19-0629 for Fe_3O_4 and 06-0615 for FeO have been considered.

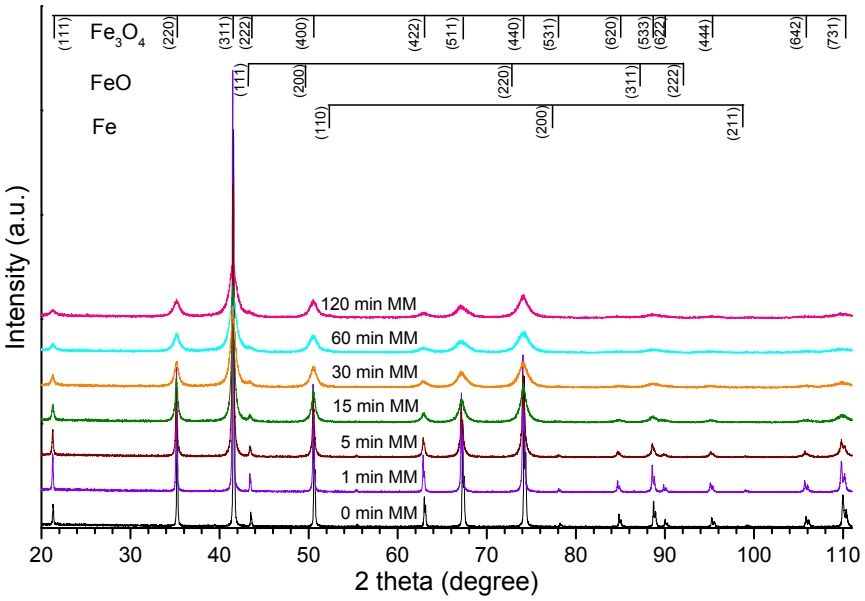

Fig. 1. X-ray diffraction patterns of the Fe_3O_4 samples milled for 0, 1, 5, 15, 30, 60 and 120 minutes.

The un-milled sample (sample obtained by heat treatment), marked in the figure as 0 min MM presents only the peaks characteristics for the cubic spinel structure of the magnetite. The same Bragg reflections are observed also for the samples milled up to 60 minutes. In the patterns of the samples milled for 60 and 120 minutes a new Bragg peak can be observed. This peak is assigned to the elemental iron, which is provided by powder contamination during milling. This is a well-known phenomenon that occurs during processing powder by mechanosynthesis route [14, 15]. In the case of milling ferrites the contamination is more pronounced due to the very abrasive characteristic of these materials [15]. In the figure 2 is presented a detail of X-ray diffraction patterns of the Fe_3O_4 samples milled 60 and 120 minutes in the 2θ range where the elemental Fe most intense peak ((110) line) is visible.

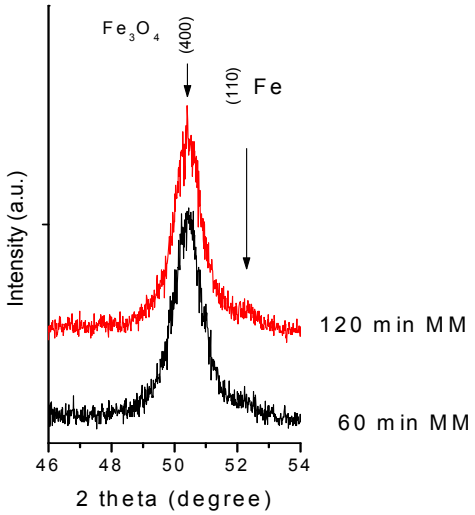

Fig. 2. Details of X-ray diffraction patterns of the Fe_3O_4 samples milled 60 and 120 minutes in the 2θ range where the Fe most intense peak is visible.

Upon increasing the milling time it can be noticed that the magnetite peaks become larger as compared to the magnetite un-milled sample. This is assigned, on the one hand, to the crystallite size refinement and on the other hand to the internal stresses induced in the samples by mechanical milling process [15]. In the figure 3 is shown the evolution of the mean crystallite size as a function of milling time for the Fe_3O_4 milled samples. One can observe that, for short milling times, the magnetite becomes nanocrystalline. After only 5 minutes of milling the mean crystallite size is about 110 nm. By increasing the milling duration at 15 minutes, the mean crystallites size is reduced down to 22 nm. At the final milling duration

the mean crystallites size is about 8 nm. It can be also observed that after 30 minutes of milling, the mean crystallite size variation is lower, from 11 to 8 nm. This is in agreement with the early reported results that show a saturation of the crystallites reduction at a certain milling time [14].

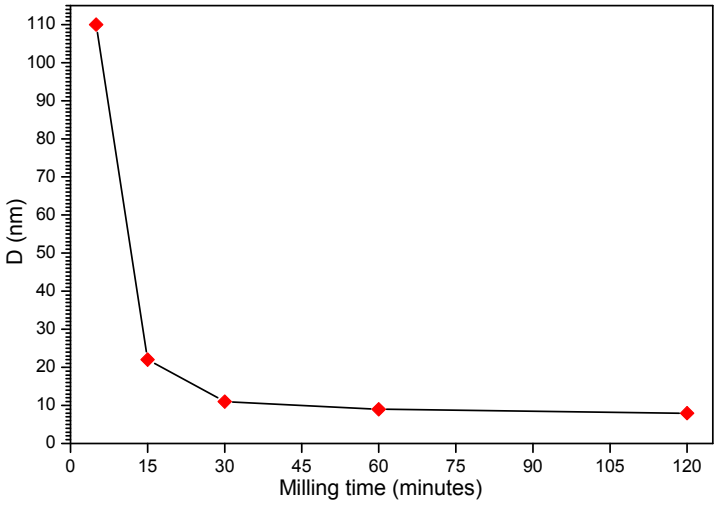

Fig. 3. Evolution of the mean crystallite size versus milling time for the Fe_3O_4 milled samples.

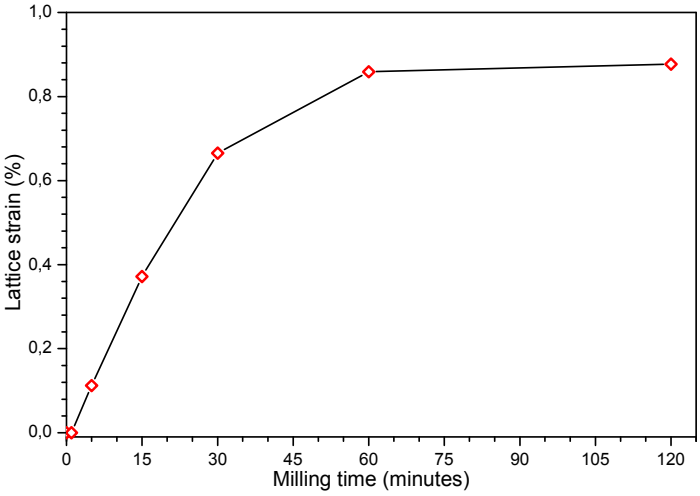

Fig. 4. Evolution of the lattice strain versus milling time for the Fe_3O_4 milled samples.

Figure 4 presents the evolution of the lattice strain as a function of milling time for the Fe_3O_4 milled samples. Upon increasing the milling time the lattice strains increase. In the first half of the milling process, durations up to 60 minutes, a rapid increase of the lattice strain is noticed. After this, in the second half of the milling process a saturation of the lattice strain is attained. The repeated fragmentation and cold welding processes lead to the appearance of the lattice strains [14].

Magnetisation curves recorded at 300 K for the Fe_3O_4 milled samples in a magnetic field up to 9 T are presented in the figure 5. It can be noticed that up to 5 minutes of milling the shape and values of the magnetisation are almost unchanged, suggesting that the mechanical milling has a very slight influence above this magnetic characteristic for this milling durations. Further increase of the milling time leads to a significant change of the magnetization. It can be observed that the values of the magnetisations decrease. Also, it is observed that, the magnetisation tends to become unsaturated. This phenomenon is more visible for the samples milled for 60 and 120 minutes. The tendency of the magnetisation to become unsaturated is associated which spin canted effect and other surface effects such as disordered magnetic shell structure [15, 16].

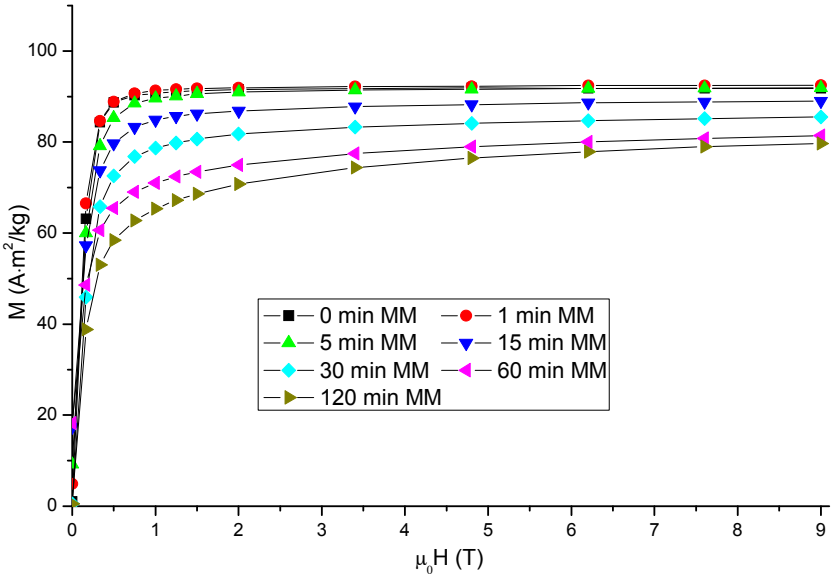

Fig. 5. Magnetisation curves recorded at 300 K for the Fe_3O_4 milled samples.

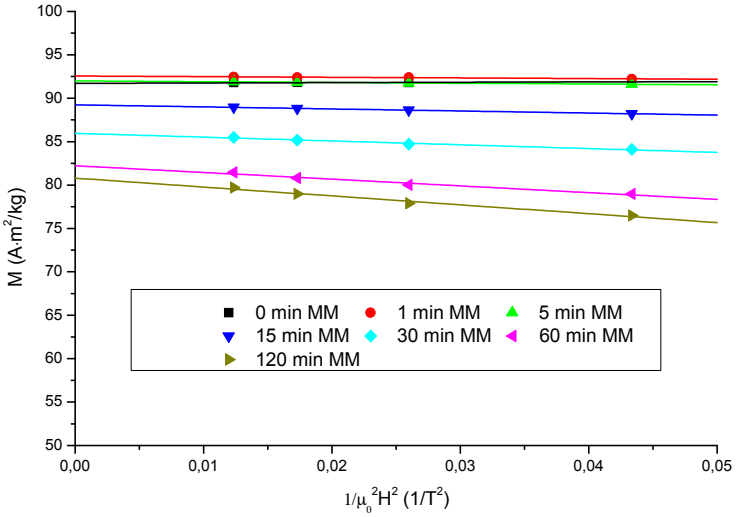

Fig. 6. M=f(1/H^2) plots of the Fe_3O_4 milled samples.

In order to determine the saturation magnetisation of the magnetite samples the M versus (1/(μH)^2) has been plotted. The M(1/(μH)^2) plots are presented in the figure 6. It can be observed that in the high-field region the M versus (μH)^2 plots have good linearity and the extrapolation to zero represents the values of the saturation magnetization.

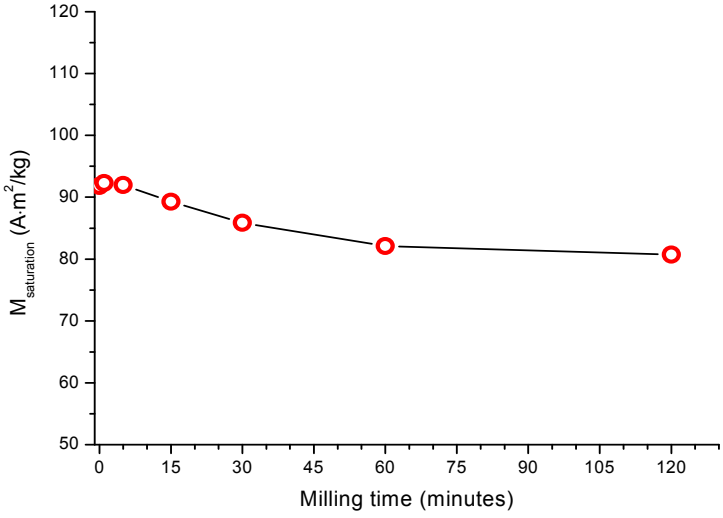

Fig. 7. Evolution of the saturation magnetisation of the Fe_3O_4 milled samples versus milling time.

The value of saturation magnetisation as resulted from the $M=f(1/(\mu H)^2)$ plots as a function of milling time is shown in the figure 7. It can be observed that the saturation magnetisation decreases upon increasing the milling time. In the case of the un-milled samples (0 minutes MM) the saturation magnetisation is about 91.8 $A \cdot m^2/kg$ and in the first 5 minutes of milling is almost constant. The value of the saturation magnetisation is very close to the one reported for the magnetite in reference [4] of about 92 $A \cdot m^2/kg$. After that, a decrease is observed, the saturation magnetisation decreases up to 80.7 $A \cdot m^2/kg$ upon increasing the milling time up to 120 minutes. The magnetisation decreased with about 11 % upon increasing the milling time from 0 to 120 minutes. The decrease of the saturation magnetisation is caused by the structural disorder and defects induced into the samples by high energy ball milling. These defects can be dislocations, vacancies, cations inversion, spin canted or surface spin disorder [15, 16]. If is taken into account a full inverse spinel ferrite (all the Fe^{2+} cations are located in octahedral sites) the net magnetic moment for a magnetite molecule is 3.8 μB. Resulting thus that the Fe^{2+} cations possess also a net magnetic moment of 3.8 μB. This is very close to the calculated one which is 4 μB. The net magnetic moment of the magnetite molecule decreases upon milling the sample for 120 minutes at about 3.35 μB. This suggests a large particles specific surface of the particles (very fine particles), that give rise to large amount of cations that have canted spins.

CONCLUSIONS

The nanocrystalline magnetite powder has been successfully obtained by mechanical milling of the well crystallised samples synthesised by heat treatment of a stoichiometric mixture of iron and hematite. The mean crystallite size decreases upon increasing the milling time and in the same time the lattice strains that are induced into the sample increases. A powder contamination with elemental iron provided by milling bodies was noticed. The magnetisation of the samples decreases upon increasing milling time due to the several causes such as structural defects and structural disorder, internal stresses or surface effects. The magnetisation tends to become unsaturated for long milling time as a result of spin canted effect.

ACKNOWLEDGEMENTS

This paper was supported by the Post-Doctoral Programme POSDRU/159/1.5/S/137516, project co-funded from European Social Fund through the Human Resources Sectorial Operational Program 2007-2013.

REFERENCES

1. R.M Cornell, U. Schwertmann, “The iron oxides”, Wiley-VCH Verlag, KGaA, Weinheim, 2003.
2. A.K. Gupta, M. Gupta, *Biomaterials*, 26, 3995 (2005).
3. N.M. Deraz, A. Alarifi, *Ceram. Int.,* 38, 4049 (2012).
4. B.D. Cullity, C.D. Graham. “Introduction to Magnetic Materials”, 2nd edition, IEEE Press& Wiley, New Jersey, 2009.
5. D. Wilson, M.A. Langell, *Appl. Surf. Sci.,* 303, 6 (2014).
6. P. Panneerselvam, N. Morad, K.A. Tan, *J. Hazard. Mater.,* 186, 1608 (2011).
7. K. Hayashi, W. Sakamoto, T. Yogo, *J. Magn. Magn. Mater.,* 321, 450 (2009).
8. M. Fang, V. Ström, R.T. Olsson, L. Belova, K.V. Rao, *Nanotechnology*, 23, 145601 (2012).
9. C. Li, Y. Wei, A. Liivat, Y. Zhu, J. Zhu, *Mater. Lett.,* 107, 23 (2013).
10. B. Peeples, V. Goornavar, C. Peeples, D. Spence, V. Parker, C. Bell, D. Biswal, G.T. Ramesh, A. K. Pradhan, *J. Nanopart. Res.,* 16, 2290 (2014).
11. X. Wu, J. Tang, Y. Zhang, H. Wang, *Mater. Sci. Eng., B*, 157, 81 (2009).
12. G.F. Goya, *Solid State Commun.,* 130, 783 (2004).
13. G.K. Williamson, W.H. Hall, *Acta Metall.,* 1, 22 (1953).
14. C. Suryanarayana, “Mechanical Alloying and Milling”, Marcel Dekker, New York, 2004.
15. T.F. Marinca, I. Chicinaş, O. Isnard, V. Popescu*, J. Am. Ceram. Soc.,* 96, 469 (2013).C.N.
16. Chinnasamy, A. Narayanasamy, N. Ponpandian, K. Chattopadhyay, H. Guérault, J.-M. Greneche, *Journal of Physics: Condensed Matter*, 12, 7795 (2000).

STUDIA UBB PHYSICA, Vol. 60 (LX), 1, 2015, pp. 83-90
(RECOMMENDED CITATION)

Dedicated to Academician Professor Dr. Emil Burzo on His 80th Anniversary

MAGNETIC PHASE TRANSITION AND MAGNETOCALORIC EFFECT IN THE PEROVSKITE $La_{0.55}Ca_{0.45}MnO_3$

I.G. DEAC[1*], A. VLADESCU[1,2], R. TETEAN[1]

ABSTRACT. We report results of magnetic and magnetocaloric investigations of the perovskite manganite $La_{0.55}Ca_{0.45}MnO_3$. The sample shows ferromagnetic behavior at low temperatures. Magnetocaloric effect was estimated from the magnetic entropy change ΔS_M obtained from isothermal magnetization data. We have found large values for $|\Delta S_M|$ around T_C's, of about 4.58 J/kg·K for $\mu_0\Delta H$ = 4 T, with reasonable large relative cooling power (~233 J/kg). Critical exponents associated with the ferromagnetic phase transition were analyzed and found to be close to those expected for the three-dimensional Heisenberg model. This model was also verified by using the field dependence of magnetic entropy change method.

Keywords: *Perovskite ceramics, Magnetic phase transition, Magnetic measurements, Magnetocaloric effect.*

INTRODUCTION

In recent times, there has been a significant increase in research on the magnetocaloric effect (MCE) [1]. The magnetic refrigeration, using the magnetocaloric effect, seems to be more effective and environmentally friendly than the vapor compression refrigeration. Earlier works indicated that gadolinium (Gd) has been considered as the most active magnetic refrigerant in room-temperature magnetic refrigerators [2]. A much larger MCE, twice larger as in Gd, was found in $Gd_5Si_2Ge_2$ [3]. In the last few years, some other alternative materials were considered to be of practical importance, such as $Gd_5(Si_{1-x}Ge_x)_4$ [3], $MnAs_{1-x}Sb_x$ [4], $MnFeP_{1-x}As_x$ [5], $Tb_{1-x}Gd_xAl_2$ [6]

[1] Faculty of Physics, Babes-Bolyai University, Str.M. Kogalniceanu 1, Cluj-Napoca, Romania
[2] *Emerson Process Management – Roxar Division Cluj-Napoca, Romania*
* *Corresponding author e-mail: iosif.deac@phys.ubbcluj.ro*

and the hole-doped manganites with the general formula $Ln_{1-x}A_xMnO_3$ (Ln = trivalent rare earth, A = divalent alkaline earth) [2, 7-10]. Since the Gd-based alloys have expensive cost prices, the research has been focused on materials that are cheaper but displaying larger MCEs [1, 2, 7, 9, 10]. A very important quality of these refrigerant materials is to show a large magnetic entropy change $|\Delta S_M(T; H)|$, under an external magnetic field variation. The mixed-valence manganites $Ln_{1-x}A_xMnO_3$ which are known for their colossal magnetoresistance (CMR) effect are promising materials since their Curie temperature T_C and saturation magnetization are strongly composition dependent and the magnetic refrigeration can be realized at various temperature ranges.

The perovskite $La_{1-x}Ca_xMnO_3$ is an important member in manganite family with intermediate bandwidth [11]. The La-based manganites show a very rich magnetic phase diagram including the charge/orbital ordering (CO/OO) state, FM and antiferromagnetic (AFM) states (and coexistence) [12, 13]. For $x < 0.5$, they possess a strong FM–PM phase transition and a large magnetoresistance effect. When $x > 0.5$, it shows a CO-antiferromagnetic (AF) state. The compound $La_{0.55}Ca_{0.45}MnO_3$, lies very close to the boundary of FM and CO-AF phase, being still ferromagnetic, having a high Curie temperature and a narrow FM - PM transition. These facts suggest the possibility of a large MCE in this compound that can be potentially used in magnetic refrigerators. Usually, MCE at T_C is higher for a first order magnetic transition, but because the transition takes place in a narrow temperature range, the resulting *cooling power* is lower [1, 2]. The materials that show second order phase transitions, have a smaller magnitude of entropy change $|\Delta S_M|$, but it is extended on a broader temperature range, resulting in a larger *cooling power*.

The present work is a study of the critical magnetic behavior and of the magnetocaloric effect in $La_{0.55}Ca_{0.45}MnO_3$ manganite. We have found quite large values of magnetic entropy change and high relative cooling power in this compound, making it interesting for magnetic refrigeration over a wide temperature range. The magnetic phase transition and the magnetic entropy change in the region of the transition temperature can be described in the frame of the short-range 3 D Heisenberg model.

EXPERIMENTAL

The sample $La_{0.55}Ca_{0.45}MnO_3$ was synthesized using the conventional solid state reaction method, and it was the same which was studied in a previous experiment [14].

A commercial cryogen-free VSM magnetometer (Cryogenic Ltd.) was used for magnetic measurements in the temperature range 5 - 300 K and in magnetic fields up to 12 T. Zero field-cooled (ZFC) and field-cooled magnetizations, as a function of temperature, were measured in 0.1 T.

As known, the MCE can be estimated calculating the magnetic entropy change ΔS_M (T; H_0), associate with a change in magnetic field. For a second order phase transitions we can use the approximation [1]:

$$\Delta S_M(T,H_0) == \frac{\mu_0}{\Delta T}\int_0^{H_0}[M(T+\Delta T,H)-M(T,H)]dH \quad (1)$$

In consequence, we measured the isothermal *M(H)* curves at a temperature interval of ΔT = 5 K around the magnetic transition to calculate the magnetic entropy change.

The cooling power per unit volume - the relative cooling power (*RCP*) - is a very important parameter for selecting magnetic refrigerants:

$$RCP(S) = .\text{-}\Delta S_M(\max) \text{ x } \delta T_{FWHM} \quad (2)$$

here ΔS_M (max) is the maximum value of change in the magnetic entropy and δT_{FWHM} is the full width at half maximum (FWHM) of ΔS_M vs. T curve. A good magnetocaloric material needs to have both a large magnitude of ΔS_M and a broad width of the ΔSM (T) curve.

RESULTS AND DISCUSSIONS

The diffraction pattern showed a pure LCMO sample having an orthorhombic unit cell with lattice parameters: a = 5.428 Å; b = 7.663 Å; c = 5.443 Å [14].

Figure 1 illustrates the temperature dependence of FC and ZFC magnetization taken in 0.1 T. The Curie temperature T_C = 251 K was determined as the point where dM/dT has a minimum, as shown in the inset of Fig.1. The magnetization has a low history dependence with a bifurcation between ZFC and FC $M(T)$ curves.

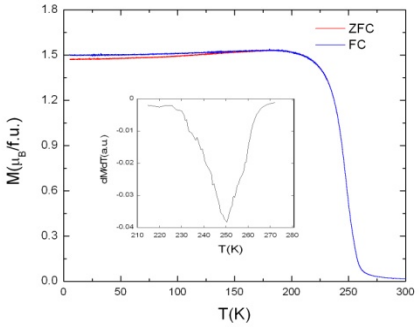

Fig. 1. FC and ZFC magnetization as a function of temperature, measured in 0.1 T. Inset: d$M(T)$/dT.

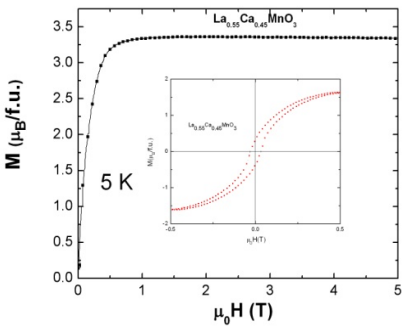

Fig. 2. M(μ_0H) curve taken at 5 K up to 5 T. Inset: M(μ_0H) hysteresis loop at 5 K.

At low temperatures the magnetization M_S (5 K) ≈ 3.4 μ_B was close to the theoretical saturation value (3.55 μ_B) in fields higher than 1 T. The inset of Fig. 2 indicate a very weak magnetic hysteresis with H_C = 0.033 T at 5 K. The magnetic behaviour described in Figs. 1 and 2 indicates a FM behavior of this compound below T_C. Since we are faced with a sharp magnetic phase transition, we expect a large MCE, around T_C.

In Fig. 3 we show the $M(H)$ curves for temperatures taken from 190 K to 285 K. As can be seen, below T_C the $M(H)$ increases rapidly at low fields. It is important to note that the main changes of the magnetization occurred in a relative low-field range (below 1 T), which is very important for the household applications. The order of the phase transition was established analyzing the Arrot plot (M^2 versus H/M) [15] on the Banerjee criterion [16] basis.

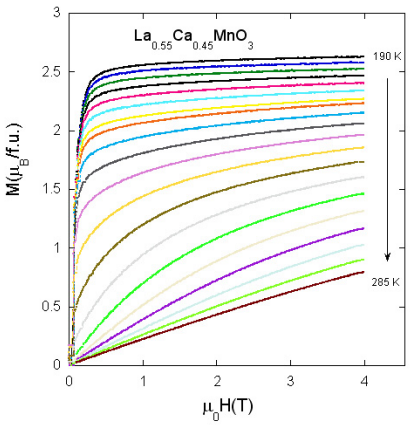

Fig. 3. Isothermal magnetization curves $M(\mu_0 H)$ taken at fixed temperature interval of 5 K, from 190 to 285 K.

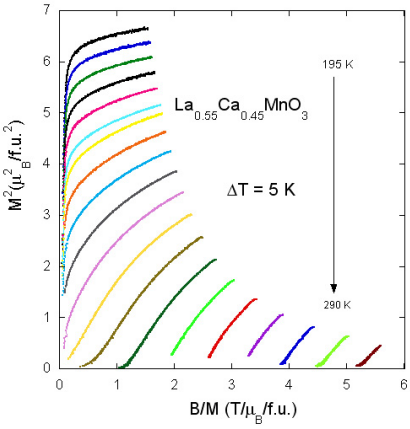

Fig. 4. Arrot plots obtained from measured M vs. H isotherms.

According to this, if the H/M versus M^2 curves has positive slopes, close to T_C, we are faced with a second order phase transition. If negative slope curves are presents, the transition is first order. The Arrot plot for our system can be seen in Fig.4. The curves have positive slopes in all the M^2 range indicating a second order magnetic phase transition [16]. In the case of a second order magnetic phase transition, the entropy change ΔS_M can be readily calculated from $M(H)$ isotherm data, by using the approximation given in eq. (1).

We estimated the MCE, from the magnitude of the magnetic entropy change, which was calculated from the isothermal magnetization curves. These curves were measured in the range 0 – 4 T around T_C with a temperature interval of 5 K and a field step of 1 T.

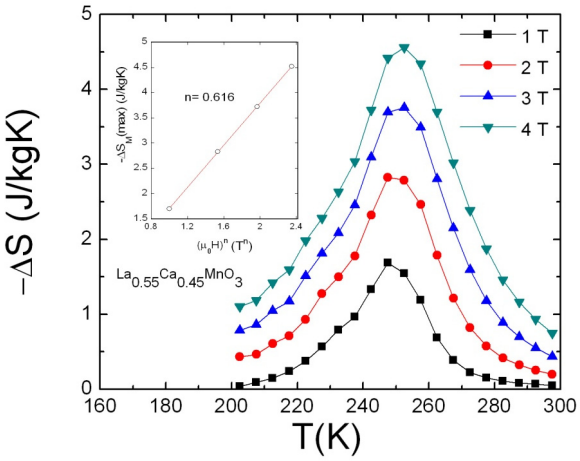

Fig. 5. The magnetic entropy change - ΔS_M as a function of temperature in various fields for $La_{0.55}Ca_{0.45}MnO_3$. In the inset: the maximal entropy change vs. applied magnetic field; the solid line is the fitting curve.

To analyze the magnetocaloric effect, $-\Delta S_M$ is plotted in Fig. 5, as a function of temperature for different values of $\mu_0 H$, from 1 to 4 T.

As expected, the magnetic entropy change curves present peaks located very close to the Curie temperature T_C, at about 252 K. The maximum value, $-\Delta S_M$ (max), was about 4.58 J/kg K in 4 T and it still has a large value of 1.70 J/kg K when the change of the field was 1 T, which is high enough for magnetic refrigeration.

The transition range becomes broader in higher applied magnetic fields, and δT_{FWHM} changes from about 24 K in 1 T, to 45 K in 4 T. These lead to a large *RCP* indicating a material with a high cooling capacity. It can be seen in Fig. 5, that the ΔS_M distribution is rather uniform, which is also a very important aspect for a magnetic cooler. The *RCP* for this compound reaches 233 J/kg for $\mu_0 \Delta H$ = 4 T. Some quantitative parameters related to magnetocaloric effect in $La_{0.55}Ca_{0.45}MnO_3$ are given in Table 1.

The magnitudes of the MCE obtained for our sample at T_C are higher or comparable to those measured in the case of other manganites [1, 2, 7-10] indicating that this material could be used in magnetic cooling.

A large entropy change was expected in this compound where the magnetization has a sharp variation around T_C. A larger MCE is expected in a system that shows a stronger spin–lattice coupling, as usually happens in manganese perovskites [17].

Table 1. Maximum entropy changes, $-\Delta S_M^{\max}$, full width at half maximum of the $\Delta S_M(T)$ curve δT_{FWHM} and relative cooling powers (*RCP*) when $\mu_0\Delta H$ = 1 – 4 T, temperature of the maximum entropy change T(max) = 252 K for the sample $La_{0.55}Ca_{0.45}MnO_3$.

$\mu_0\Delta H$ (T)	$-\Delta S_M^{\max}$ (J.kg^{-1}.K^{-1})	δT_{FWHM} (K)	*RCP* (J.kg^{-1})
1	1.68	31	52
2	2.87	40	114
3	3.80	48	182
4	4.58	51	233

We can also use the Arrot plot to analyze the critical behavior of this compound near the phase transition. The M^2 vs. H/M curves, in Fig. 4, are not straight, mainly at low magnetic fields, indicating that the mean field model is not valid to describe this phase transition. To calculate the critical exponents we have used the modified Arrot plot (MAP) method [18]. The critical exponents β, γ and δ are defined as [19, 20]:

$$M_S(T) = M_0(-\varepsilon)^{\beta}, \qquad T < T_C \tag{3}$$

$$\chi_0^{-1}(T) = \left(\frac{h_0}{M_0}\right)\varepsilon^{\gamma} \qquad T > T_C \tag{4}$$

$$M = DH^{1/\delta} \qquad T = T_C \tag{5}$$

where ε is the reduced temperature $\varepsilon = (T-T_C)/T_C$ and M_0, h_0/M_0 and D are critical amplitudes; β, γ and δ also satisfy the Widom scaling relation: $\beta + \gamma = \beta\delta$.

The MAP method is an iterative procedure presumes the use of the Arrott–Noakes (A–N) [18] plot (i.e. the plot of $M^{1/\beta}$ vs. $(H/M)^{1/\gamma}$). The spontaneous magnetization value $M_S(T,0)$ is obtained from the intercepts of isothermal $M(H)$ curves on the ordinate of the plot (for temperatures below T_C). In a similar way, the reciprocal susceptibility $\chi_0^{-1}(T)$ is obtained from the intercepts on abscissa.

Thermal variation of the spontaneous magnetization $M_S(T)$ and the inverse susceptibility $\chi_0^{-1}(T)$ obtained from the modified Arrot plot are displayed in Fig. 6.

The values of the critical exponents can be derived by fitting these values to eq. (3), (4) and (5). By successive iterations, the best fits we got: T_C = 252 K, β = 0.385, γ = 1.350 and δ = 4.506. These values are closer to that predicted by the 3D-Heisenberg ferromagnets (β = 0.36; γ = 1.39; δ = 4.8) [19].

Such a behavior was also demonstrated by using numerical calculations [21, 22]. These showed that in frame of the double-exchange model, the critical exponents can be consistent with those expected for the isotropic short range 3D Heisenberg model. Also, the phase separation scenario in manganites, agrees with the short range magnetic interaction in these compounds. The presence of the ferromagnetic clusters in manganites was often found in simple magnetic measurements [23].

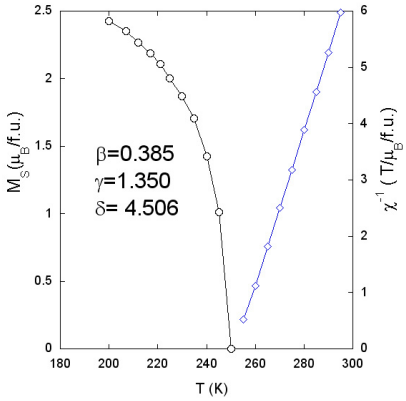

Fig. 6. The spontaneous magnetization $M_S(T)$ and the inverse initial susceptibility $X_0^{-1}(T)$ along with the fitting curves for $La_{0.55}Ca_{0.45}MnO_3$.

A magnetic field dependence of magnetic entropy change, a universal relation $|\Delta S_M| \propto H^n$, is expected [24] in a magnetic system with a second-order phase transition. The local exponent *n* can be calculated as [25]:

$$n = 1 + \frac{\beta - 1}{\beta + \gamma} \tag{6}$$

The field dependence of maximum magnetic entropy change is described in the inset of Fig. 5. It can be seen, that the dependency $|\Delta S_M| \propto H^n$, is linear when $n = 0.616$. If we combine eq. (4) with Widom scaling relation, the values of the critical exponents can be readily obtained as: $\beta = 0.366$ and $\gamma = 1.283$ presuming $\delta = 4.506$ (using: $M = DH^{1/\delta}$ at $T = T_C$). The values of the critical exponents found in this way are in very good agreement to the values obtained by using MAP method, confirming the suitability of the short-range order 3 D- Heisenberg model to describe the critical magnetic behavior of this compound.

CONCLUSIONS

Magnetic critical phase transition and magnetocaloric material potential of $La_{0.55}Ca_{0.45}MnO_3$ were studied. We obtained a large magnetic entropy change $|\Delta S_M|$ ~4.58 J/kg K for $\mu_0\Delta H = 4$ T at the FM - PM phase transition temperature, and a high relative cooling power *RCP* ~233 J/kg. The critical phase transition was investigated by using the modified Arrot plot (MAP) method. The phase transition

was found to be second order having critical exponents corresponding to those predicted for the short-range 3 D-Heisenberg model. This result was also confirmed analyzing the field dependence of the magnetic entropy change.

ACKNOWLEDGEMENTS

This work was supported by the grant IDEI code PN-II-ID-PCE-2011-3-0583 of CNCS, Romania.

REFERENCES

[1] A.M. Tishin, Y.I. Spichkin, The Magnetocaloric Effect and Its Applications, Institute of Physics, Bristol 2003.
[2] K.A. Gschneidner Jr., V.K. Pecharsky, A.O. Tsokol, *Rep. Prog. Phys*. 68 (2005) 1479–1539.
[3] V.K. Pecharsky, K.A. Gschneidner, Jr., *Phys. Rev. Lett.* 78 (1997) 4494 - 4497.
[4] S. Gama, A. Coelho, de Campos, et al., *Phys. Rev. Lett.* 93 (2004) 237202.
[5] O. Tegus, E. Brück, K.H.J. Buschow, and F.R. de Boer, *Nature* (London) **415**, 150 (2002).
[6] W. Wang, X.X. Zhang, F.X. Hu, *Appl. Phys. Lett.* 77 (2000) 1360-1368.
[7] M.-H. Phan, S.-C. Yu, *J. Magn. Magn. Mater*. 308 (2007) 325–340.
[8] V.B. Naik, S.K. Barik, R. Mahendiran, B. Raveau, *Appl. Phys. Lett*., 98 (2011) 112506 (1-3).
[9] M.-H. Phan, S.-C. Yu, *J. Magn. Magn. Mater*. 308 (2007) 325–340.
[10] W. Zhong, C-T Au, Y-W Du, *Chin. Phys. B* 22 (2013) 057501 (1-11).
[11] A. Ramirez*, J. Phys.: Condens. Matter* 9 (1997) 8171–8199.
[12] P. Schiffer, A.P. Ramirez, W. Bao, and S.-W. Cheong, *Phys. Rev. Lett*. **75**, (1995) 3336-3339.
[13] Y. Tokura, Y. Tomioka, *J. Magn. Magn. Mater*.200 (1999) 1-23.
[14] I.G. Deac, I. Balasz, *Mater. Chem. Phys*. 136 (2012) 850-857.
[15] A. Arrott, *Phys. Rev*. 108 (1957) 1394-1396.
[16] S.K. Banerjee, *Phys. Lett.* 12, (1964) 16-17.
[17] A. Asamitsu, Y. Moritomo, Y Tomioko, T. Amira and Y. Tokura, *Nature* 373 (1995) 407-409.
[18] A. Arrott, J.E. Noakes, *Phys. Rev. Lett*. 19 (1967) 786-789.
[19] H. Eugene Stanley, Introduction to Phase Transitions and Critical Phenomena, Clarendon Press, Oxford (1971)
[20] M.E. Fisher, *Reports on Progress in Physics* 30 (1967) 615-730.
[21] J.L. Alonso, L.A. Fernandez, F. Guinea, V. Laliena, V. Martin-Mayor, *Nucl. Phys*. *B* 596, (2001) 587-610.
[22] Y. Motome and N. Furukawa, *J. Phys. Soc. Jpn*. 70, (2001) 1487-1490.
[23] S. Hcini, S. Zemni, A. Triki, H. Rahmouni, M. Boudard*, J. Alloys Compd*. 509 (2011) 1394–1400.
[24] H. Oesterreicher and F.T. Parker, *J. Appl. Phys*. 55, (1984) 4334-4338.
[25] V. Franco, A. Conde, J.M. Romero-Enrique, and J.S. Blazquez, *J. Phys.: Condens. Matter* 20, (2008) 285207(1-5).

STUDIA UBB PHYSICA, Vol. 60 (LX), 1, 2015, pp. 91-101
(RECOMMENDED CITATION)

Dedicated to Academician Professor Dr. Emil Burzo on His 80th Anniversary

COLLECTIVE BEHAVIOR OF COUPLED QUANTUM MECHANICAL OSCILLATORS

L. DAVIDOVA[1], S. BORBÉLY[1] AND Z. NÉDA[1,2*]

ABSTRACT. A simple model of coupled oscillators is investigated from the perspective of quantum mechanics. The classical model of two oscillators connected by a common platform can be easily solved analytically, but the quantum system requires a numerical approach. We assume that both the oscillators and the platform are quantum objects in their respective ground states at start and they evolve in time as a connected system. By following numerically this time-evolution we investigate the dynamics of the oscillators and calculate an order parameter that characterizes their correlated time-evolution. We study the order parameter as a function of the oscillators initial state and compare the findings with the equivalent classical system. Interestingly, for a given parameter region we found an enhanced collective behavior in the quantum mechanical system.

Keywords*: nonlinear dynamics, collective behavior, quantum synchronization, coupled oscillators*

INTRODUCTION

Systems of coupled oscillators have provided great demonstrations of complex behaviour emerging from the interaction of simple system. Classical coupled oscillators have been thoroughly studied from the earliest observations of spontaneous synchronization by Huygens [1], and still are of great interest to physicists. Recent experimental studies conducted using metronomes on a moving platform [2] or a freely rotating platform [3], as well as detailed numerical

[1] *Babeş-Bolyai University, Faculty of Physics, 1 Kogălniceanu str., 400084 Cluj-Napoca, Romania*
[2] *Edutus College, Department of Mechatronics, Optics, Mechanical Engineering and Informatics, Bertalan Lajos Street 4-6, Budapest, Hungary*
** Corresponding author e-mail: zneda@phys.ubbcluj.ro*

studies of systems of pendulus [4], show that the possibility of spontaneous in-phase and anti-phase synchronization is an inherent property of such type of systems. On the other hand, it is easy to demonstrate that emergent synchronization only occurs in systems with driving and damping present, and depends on the system's parameters [5]. The simplest system of two oscillators attached to a common platform without driving or friction is exactly solvable and its degree of synchrony depends only on the initial positions of both oscillators.

If we take a closer look at this simplest system of coupled oscillators within the formalism of quantum mechanics, many of the classical properties of the oscillator systems translate into similar properties in the analogous quantum mechanical system. For instance, Y. F. Chen [6] demonstrated that the stationary coherent states of certain coupled oscillator systems possess the same shape as the classical trajectories of the system. If this holds true for the system we've selected here, we should observe similar dynamics in the quantum system and the classical one. Spontaneous synchronization should not be observed without energy dissipation or driving and the correlation between oscillators should follow a similar pattern with the classical case, being highly dependent on initial conditions. The system of coupled oscillators with dissipation has been studied by G. L. Giorgi et. al. [7] and indeed they have observed synchronization occurring between the oscillators average coordinates in a case they are connected to a common heat bath. This collective behavior depends mostly on the relevant physical parameters of the system, rather than the initial conditions. The case with driving has also been studied by Zhirov and Shepelyansky [8], and they established conditions for emergent synchronization in such systems.

Our aim here is quite modest, we intend to numerically study the collective behavior in a system of coupled quantum oscillators, using Pearson correlation between the expectation values of the oscillator coordinates as order parameter. As a quantum counterpart of the system considered by McDermott and Redmount [9], we assume that the oscillators and the platform they are attached to are initially independent quantum oscillators. They are initialized using their ground state wave functions shifted to match the desired starting positions. We intend to compare the numerical findings with the exact results obtained in the equivalent classical system.

CLASSICAL SYSTEM OF COUPLED OSCILLATORS

We consider a system of two oscillators with masses m coupled by springs of spring constants *k* to a common platform with mass *M* (Fig. 1). We denote by x_1 and x_2 the spring deformation values and by x_3 the absolute coordinate of the platform. We assume the ideal case where friction and driving are absent.

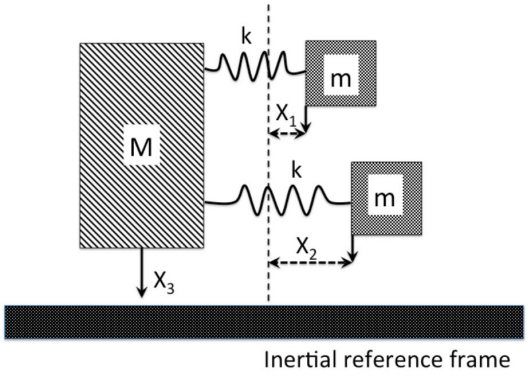

Fig. 1. The coupled oscillator system considered in our study.

The Lagrange function for this system is

$$L = \frac{1}{2}M\dot{x}_3^2 + \frac{1}{2}m(\dot{x}_1 + \dot{x}_3)^2 + \frac{1}{2}m(\dot{x}_2 + \dot{x}_3)^2 - \frac{1}{2}kx_1^2 - \frac{1}{2}kx_2^2, \qquad (1)$$

where the first term is the kinetic energy of the platform, the second and third terms stands for the kinetic energy of the oscillators relative to the chosen inertial reference frame, and the last two terms are the potential energies of the oscillators. The Euler-Lagrange equations of motion are:

$$\begin{aligned} M\ddot{x}_3 &= k(x_1 + x_2) \\ m\ddot{x}_1 &= -kx_1 - m\ddot{x}_3 \\ m\ddot{x}_2 &= -kx_2 - m\ddot{x}_3 \end{aligned} \qquad (2)$$

Eliminating the $\ddot{x}_3$ terms, we can derive a system of coupled differential equations yielding the dynamical evolution of the two masses m :

$$\begin{aligned} kx_1 + m\left(\frac{m+M}{2m+M}\right)\ddot{x}_1 - \frac{m^2}{2m+M}\ddot{x}_2 &= 0 \\ kx_2 + m\left(\frac{m+M}{2m+M}\right)\ddot{x}_2 - \frac{m^2}{2m+M}\ddot{x}_1 &= 0 \end{aligned} \qquad (3)$$

This system allows for an exact analytical solution. Assuming the initial positions of the oscillators $x_1(0) = 1, x_2(0) = a$ and that they are in rest relative to the platform $\dot{x}_1(0) = 0, \dot{x}_2(0) = 0$ the exact solutions for $x_1(t)$ and $x_2(t)$ are:

$$x_1(t) = \frac{1}{2}\left((1-a)\cos\frac{\sqrt{k}t}{\sqrt{m}} + (1+a)\cos\frac{k(2m+M)t}{\sqrt{kmM(2m+M)}} \right)$$
$$x_2(t) = \frac{1}{2}\left((a-1)\cos\frac{\sqrt{k}t}{\sqrt{m}} + (1+a)\cos\frac{k(2m+M)t}{\sqrt{kmM(2m+M)}} \right) \quad (4)$$

The Pearson correlation coefficient will be used as a measure of the synchronization level for the two oscillators. This coefficient will not distinguish between strong (phase-locked) and weak forms of synchronization. It will be denoted by *r* and it takes values between [−1,1]. For a completely in-phase synchronized state $r = 1$ and for a completely anti-phase synchronized state $r = -1$:

$$r = \frac{\langle x_1 x_2 \rangle_t - \langle x_1 \rangle_t \langle x_2 \rangle_t}{\sqrt{\langle x_1^2 \rangle_t - \langle x_1 \rangle_t^2}\sqrt{\langle x_2^2 \rangle_t - \langle x_2 \rangle_t^2}} \quad (5)$$

Here we denoted by $\langle x \rangle_t$ the time-average of quantity x. Taking into account that $\langle \cos(\alpha t) \rangle_t = 0$ and $\langle \cos(\alpha t)\cos(\beta t) \rangle_t = 0$ for all $\alpha \neq 0, \beta \neq 0$ by simple algebra one gets a result independent of m, k and M:

$$r = \frac{2a}{a^2 + 1} \quad (6)$$

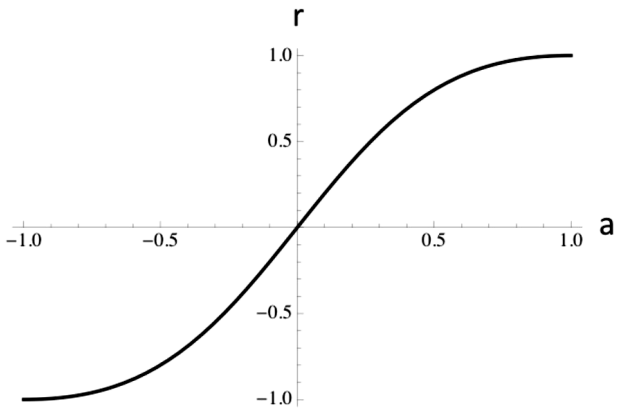

Fig. 2. Pearson correlation of the two classical oscillators coordinate as a function of the initial position of one of the oscillators ($x_1(0) = 1, \dot{x}_1(0) = 0, \dot{x}_2(0) = 0$ and $x_2(0) = a$, no friction and no driving).

We conclude that in this simple classical system, the synchronization level *r* (measured through the Pearson correlation) of the oscillators depends only on their initial relative phases and does not depend on any other physical parameters of this system. There is no phase-locked synchronization, unless the oscillators start completely in-phase or completely in anti-phase. The universal $r(a)$ curve is plotted in Fig. 2.

QUANTUM OSCILLATORS

The Hamiltonian operator of the corresponding quantum mechanical system writes as:

$$\hat{H} = -\frac{\hbar^2}{2m}\frac{\partial^2}{\partial x_1^2} - \frac{\hbar^2}{2m}\frac{\partial^2}{\partial x_2^2} - \frac{\hbar^2}{2M}\frac{\partial^2}{\partial x_3^2} + \frac{1}{2}k(x_1 - x_3)^2 + \frac{1}{2}k(x_2 - x_3)^2 \quad (7)$$

In order to study the evolution of this system, we make the assumption that all three masses start in the beginning as independent quantum oscillators initialized using their ground states wave functions centered around the mean coordinates: $\langle x_1 \rangle = x_{01}, \langle x_2 \rangle = x_{02}$ and $\langle x_3 \rangle = x_{03}$, respectively. The wave function of such system would be $\Psi_0(x_1, x_2, x_3) = \Psi_{01}(x_1)\Psi_{02}(x_2)\Psi_{03}(x_3)$, where

$$\Psi_{01}(x_1) = \left(\frac{\sqrt{mk}}{\pi\hbar}\right)^{\frac{1}{2}} \exp\frac{\sqrt{mk}(x_1 - x_{01})^2}{2\hbar}$$

$$\Psi_{02}(x_2) = \left(\frac{\sqrt{mk}}{\pi\hbar}\right)^{\frac{1}{2}} \exp\frac{\sqrt{mk}(x_2 - x_{02})^2}{2\hbar} \quad (8)$$

$$\Psi_{03}(x_3) = \left(\frac{\sqrt{Mk}}{\pi\hbar}\right)^{\frac{1}{2}} \exp\frac{\sqrt{Mk}(x_3 - x_{03})^2}{2\hbar}$$

This initial wave function can be represented as a linear combination of the eigenstates Ψ_n of the Hamiltonian (7):

$$\Psi_0(x_1, x_2, x_3) = \sum_n C_n \Psi_n(x_1, x_2, x_3) \quad (9)$$

The coefficients C_n are given as:

$$C_n = \iiint \Psi_n^*(x_1, x_2, x_3)\Psi_0(x_1, x_2, x_3)dx_1 dx_2 dx_3 \quad (10)$$

Now that we can represent the initial wave form as a combination of eigenstates, we can calculate the evolution of the system using the eigenstates Ψ_n and energy eigenvalues E_n

$$\Psi(x_1,x_2,x_3,t) = e^{-i\hat{H}t}\Psi_0(x_1,x_2,x_3) = \sum_n C_n \Psi_n(x_1,x_2,x_3)e^{-iE_n t} \tag{11}$$

In order to obtain the correlation between the coordinates of the two masses m, we must find the expectation values of x_1 and x_2:

$$\left\langle x_i(t)\right\rangle_\Psi = \iiint \Psi^*(x_1,x_2,x_3,t)x_i\Psi(x_1,x_2,x_3,t)dx_1dx_2dx_3 \tag{12}$$

We will treat the expectation values as equivalent to classical coordinates of the system. Similarly with the classical system, we choose the Pearson correlation coefficient as a measure of synchronization between the oscillators. In this approach the quantum mechanically computed order parameter is:

$$r = \frac{\left\langle X_1X_2\right\rangle_t - \left\langle X_1\right\rangle_t\left\langle X_2\right\rangle_t}{\sqrt{\left\langle X_1^2\right\rangle_2 - \left\langle X_1\right\rangle_t^2}\sqrt{\left\langle X_2^2\right\rangle_2 - \left\langle X_2\right\rangle_t^2}} \tag{13}$$

where $X_i = \left\langle x_i(t)\right\rangle_\Psi$ is obtained from (12). For an alternative calculation instead of this semi-classical Pearson correlation, one could use one where all the averages are quantum mechanically calculated

$$r' = \frac{\left\langle\left\langle x_1x_2(t)\right\rangle_\Psi\right\rangle_t - \left\langle X_1\right\rangle_t\left\langle X_2\right\rangle_t}{\sqrt{\left\langle\left\langle x_1^2(t)\right\rangle_\Psi\right\rangle_t - \left\langle X_1\right\rangle_t^2}\sqrt{\left\langle\left\langle x_2^2(t)\right\rangle_\Psi\right\rangle_t - \left\langle X_2\right\rangle_t^2}} \tag{14}$$

with:

$$\begin{aligned}\left\langle x_1x_2(t)\right\rangle_\Psi &= \iiint \Psi^*(x_1,x_2,x_3,t)x_1x_2\Psi(x_1,x_2,x_3,t)dx_1dx_2dx_3\\ \left\langle x_i^2(t)\right\rangle_\Psi &= \iiint \Psi^*(x_1,x_2,x_3,t)x_i^2\Psi(x_1,x_2,x_3,t)dx_1dx_2dx_3\end{aligned} \tag{15}$$

In our calculations we used classical averages for $\left\langle x_1x_2(t)\right\rangle$ and $\left\langle x_i^2(t)\right\rangle$, as quantum mechanical averages calculated from (15) coincide very closely with the classical averages for this system, yet bring in extra error due to the integration.

NUMERICAL APPROACH TO THE QUANTUM MECHANICAL PROBLEM

The first task is to obtain the eigenvalues and eigenvectors for the Hamiltonian (7). For this, we have to solve the stationary Schrödinger equation in three dimensions, which can be done only numerically. The simplest way to do

this is to confine the problem into a three-dimensional box where each spatial dimension of length L is represented by N equidistant points. This way we view the coordinate space as a three dimensional grid and we seek the solution for the nodes of this grid. As the grid is finite and uniform, instead of using three coordinates for the nodes of the grid, we can use only one index n ranging from 1 to N^3, which allows us to treat the wave function in this space as a one dimensional vector:

$$\Psi = \begin{pmatrix} \Psi_1 \\ \Psi_2 \\ \dots \\ \Psi_n \end{pmatrix} \tag{16}$$

The global index n replaces the three oscillator coordinate indices i_{x_1}, i_{x_2} and i_{x_3} in such a way that the resulting one dimensional vector Ψ can later be restored into its three dimensional form in the following way:

$$\Psi(x_1, x_2, x_3) = \Psi_{x_1 + x_2 N + x_3 N^2} \tag{17}$$

In such case the coordinates x_1, x_2, x_3 can be obtained as:

$$\begin{aligned} x_1 &= n \bmod N \\ x_2 &= (n \text{ quotient } N) \bmod N^2 \\ x_3 &= n \text{ quotient } N^2 \end{aligned} \tag{18}$$

On this equidistant grid the second order derivatives can be calculated using the following three-point formulas

$$\begin{aligned} \frac{\partial^2 \Psi}{\partial x_1^2} &= \frac{\Psi_{n+1} - 2\Psi_n + \Psi_{n-1}}{\left(\frac{2L}{N+1}\right)^2} \\ \frac{\partial^2 \Psi}{\partial x_2^2} &= \frac{\Psi_{n+N} - 2\Psi_n + \Psi_{n-N}}{\left(\frac{2L}{N+1}\right)^2} \\ \frac{\partial^2 \Psi}{\partial x_3^2} &= \frac{\Psi_{n+N^2} - 2\Psi_n + \Psi_{n-N^2}}{\left(\frac{2L}{N+1}\right)^2} \end{aligned} \tag{19}$$

Thus, we can write the Hamiltonian as a $N^3 \times N^3$ matrix, and the Schrödinger equation as a matrix eigenproblem:

$$\sum_{j=1}^{N^3} H_{ij} \Psi_j = E \Psi_i \tag{20}$$

which can be solved by a standard algorithm using for example the Mathematica software.

After we've obtained the eigenvectors, we can transform them back into the three dimensional form. Using the initial states (8), the evolution of the system can be calculated according to (11) and (10). Naturally in equation (10) we replace the integrals with sums according to the used numerical integration algorithm.

COLLECTIVE BEHAVIOR IN THE QUANTUM MECHANICAL SYSTEM

In order to apply the numerical method to the quantum system, we need to establish the units for all variables. For convenience of the calculations we choose a system where $\hbar = 1$. The simulated space is a cube with side up to $N = 40$. The masses of the oscillators are equal, $m_1 = m_2 = m$, the spring constants are also equal, $k_1 = k_2 = 1$, and the platform's mass is fixed at $M = 1$.

With these values we can simulate the evolution of the system, as shown in Fig. 3. Note that the initial Gaussian wave packet disperses over time due to the coupling of the oscillators. However, this dispersion still allows for treating the wave function as a packet. The expectation values of $x_1(t)$ and $x_2(t)$ according to (12) are essentially coordinates that we can treat as classical positions of the oscillators for the purpose of calculating the degree of synchronization. As an example a particular time-evolution for these quantities is given in Fig. 4.

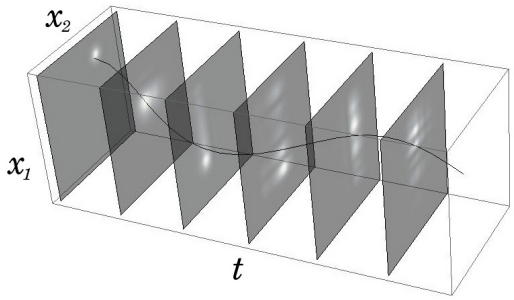

Fig. 3. Evolution of the system's wave function in the x_1, x_2 coordinate plane. The line is the trajectory of the expectation value of the system's coordinates.

As we are interested in the following in the dependence of the degree of synchrony on the initial positions of the oscillators, for computational convenience we fixed the initial position of one of the oscillators at $x_{01} = 1$ and vary that of the other oscillator's initial position between −1 and 1.

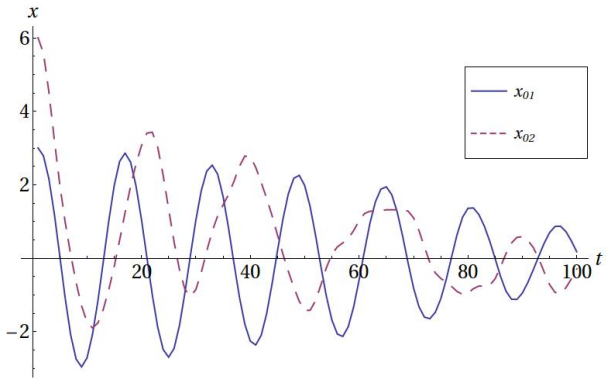

Fig. 4. Trajectories of the expectation values of x_1 and x_2 calculated with initial positions $x_{01} = 3$ and $x_{02} = 6$. The decrease in amplitude is due to the dispersion of the wave function.

Finite size effects due to the discretization of the space has a minimal influence on the obtained results. This is nicely visible on Fig. 5, where for $m = 1$ we present the computed Pearson-type correlation for different discretization $(N = 10;30;40)$. This result suggests, that $N = 40$ is an acceptable discretization, and such system sizes could still be handled by our Mathematica code.

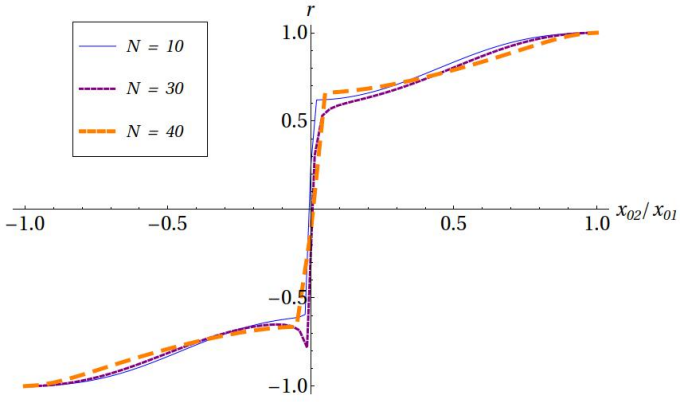

Fig. 5. Correlation curves with varying discretization number N and $m = 1$

On Fig. 6 we present the results for the correlation parameter as a function of the initial position of one of the oscillators, considering different m values. The observable trends are rather similar with the classical case: the oscillators move in a synchronicity if they start from similar coordinates and the motion is in anti-synchrony if they start in anti-phase. Beside this general trend, there are however visible differences between the quantum-mechanical and the classical curve. The collective behavior of the quantum-mechanical system is highly dependent on the mass ratio between the platform and the oscillators, whereas the classical system does not depend on it at all. In the quantum mechanical system, for small m values there is a large jump in the order parameter in the vicinity of the $x_{02} = 0$ point. Transition from the synchronized to anti-synchronized dynamics is much steeper, which means that the correlated and anti-correlated trends are much more pronounced in the quantum-mechanical system. This means, that even for a small amount of synchrony in the initial state, the system will move in a largely synchronous manner. The same is true for the initially anti-synchronized states.

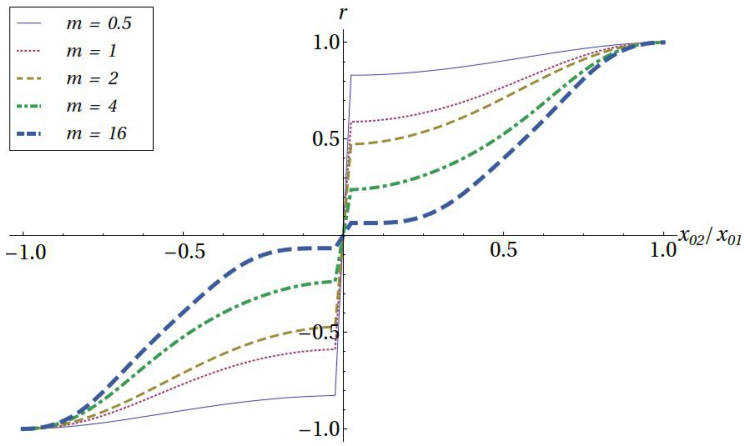

Fig. 6. Pearson correlation as a function of the initial position of one of the oscillators. Results for different m values and $N = 40$.

CONCLUSIONS

Unlike the classical system of coupled oscillators, which can be solved exactly, the quantum mechanical system could be handled only by numerical approximations. The presented results could be affected thus by border artifacts and other numerical errors. In spite of such limitations of the results, we feel that several interesting conclusions can be drawn.

First, we observed that the quantum mechanical system behaves much like the classical one in terms of the overall results regarding the initial positions of the oscillators: we obtained a collective behavior resembling synchrony if the oscillators start from similarly oriented displacements and a dynamics resembling anti-synchrony if they started from oppositely oriented initial positions. In difference with the classical coupled oscillator system, in the quantum mechanical system the transition between the positively and negatively correlated states (synchrony and anti-synchrony) is much sharper when the mass of the oscillators (m) is not too large relative to the mass of the coupling platform (M). In this limit the results indicate that the level of correlations and anti-correlations are more pronounced, which means that the quantum-mechanical system exhibits a stronger and more stable collective behavior than its classical counterpart. A noticeable difference relative to the classical system is the dependence of the observed trends as a function of m/M.

ACKNOWLEDGEMENT

We acknowledge support from research grant PN-II-ID-PCE- 2011-3-0348.

REFERENCES

1. C. Huygens it in Oeuvres Completes de Christian Huygens (1665), edited by M. Nijhoff (Societe Hollandaise des Sciences, The Hague, 1893), Vol. 5, p. 243 (a letter to his father, dated 26 Feb. 1665)
2. J. Pantaleone, *Am. J. Phys*. 70, 9921000 (2002)
3. Sz. Boda, Sz. Ujvari, A. Tunyagi and Z. Neda, *European Journal of Physics,* **34** 1451 (2013)
4. M. Kapitaniak, K. Czolczynski, P. Perlikowski, A. Stefanski, and T. Kapitaniak, *Physics Reports,* **517** (2012)
5. Davidova L, Ujvari Sz. and Neda Z., *Sync or anti-sync - dynamical pattern selection in coupled self-sustained oscillator systems*, poster at XXV IUPAP Conference on Computational Physics, accepted contribution in the Journal of Physics: Conference Series (JPCS).
6. Chen, Y.F., *Physical Review A,* **83.3** (2011): 032124.
7. Giorgi, Gian Luca et al., *Physical Review A,* **85.5** (2012): 052101.
8. Zhirov, O.V. and Dima L. Shepelyansky, *The European Physical Journal D-Atomic, Molecular, Optical and Plasma Physics* **38.2** (2006): 375-379.
9. McDermott, Rachael M. and Ian H. Redmount, "Coupled Classical and Quantum Oscillators", arXiv preprint quant-ph/0403184 (2004).

STUDIA UBB PHYSICA, Vol. 60 (LX), 1, 2015, pp. 103-108
(RECOMMENDED CITATION)

Dedicated to Academician Professor Dr. Emil Burzo on His 80th Anniversary

STRUCTURAL PARTICULARITIES OF THE SILVER AND COPPER DOPED SiO_2–CaO–P_2O_5 BASED BIOACTIVE GLASSES

R.A. POPESCU[1,2], K. MAGYARI[1], R. STEFAN[2], I. PAPUC[2], L. BAIA[1*]

ABSTRACT. Silver and copper oxidesdoped SiO_2–CaO–P_2O_5 based bioactive glasses were obtained and structurally investigated taking into consideration their possible use as biomaterials for bone regeneration. The samples synthesized by the sol-gel method have shown the existence of a preponderantly amorphous structure, as indicated by the X-ray diffraction (XRD) data. The samples were further heat treated at 600 °C and investigated by means of XRD, Fourier Transform Infrared Spectroscopy (FT-IR) and UV-vis spectroscopy. The XRD data revealed features that can be associated with theexistence of apatite like crystallization centers. UV-vis absorption spectra indicate the presence of a small amount of metallic silver in the glass matrix, while the FT-IR spectra of silver and copper doped SiO_2–CaO–P_2O_5 samples shown common characteristics to the bioactive glasses.

Keywords: *bioactive glasses, FT-IR, silver, copper*

INTRODUCTION

The development of bioactive glasses is one of the most important subjects in the field of hard tissue implants. Almost 40 years after being discovered by Prof. Hench, bioactive glasses still attract the attention of many researchers all over the world [1, 2].

Sol-gel represents one of the main process alongside the melt-quenching method [3]. It has been claimed that one of the essential advantages of this process relates to its resource to produce new glasses from structures which would normally crystallize if processed by quenching a melt [4, 5].

[1] *Faculty of Physics & Interdisciplinary Research Institute on Bio-Nano-Sciences, Babes-Bolyai University, M. Kogalniceanu 1, 400084 Cluj-Napoca, Romania*
[2] *Faculty of Veterinary Medicine, University of Agricultural Science and Veterinary Medicine, 400372 Cluj-Napoca, Romania*
[*] *Corresponding author: lucian.baia@phys.ubbcluj.ro*

Sol-gel glasses based on SiO_2–CaO–P_2O_5 are recognized as bioactive in a very different chemical proportion [6]. Some authors have originally reported about sensitive compositions of the glass to reach and maintain bioactivity. They did the investigation through in vitro studies [6, 7]. A benefit of sol-gel synthesized glasses is that they can be formed with different metallic nanoparticles to create a particular composition [8].

It is well known that silver exhibitsantibacterial properties [8, 9] and copper is recognized to have, besides antibacterial properties, very significantly angiogenetic properties [8]. In a previous study, we demonstrated that the glasses with a minimum of 0.2 mol% Ag_2O displayeda good antibacterial effect against L. monocytoges ATCC 19115, but once the Ag_n clustersoccurred this effect was diminished [10].

The release of copper *in vivo* has been figured to minimise the risk of ischemia in skin flaps. It was discovered that copper-composition scaffolds not only provided guided vascularization, but also improves wound healing [11]. Wu et al. [12] has reported that a Cu-containing bioactive porous scaffold was successfully prepared by incorporating Cu^{2+} into glass. In the same study it has been demonstrated that it is possible to develop multifunctional scaffolds by combining enhanced angiogenesis potential, osteostimulation, and antibacterial properties for the treatment of large bone defects.

The main purpose of this study is to obtain and structurally characterize glasses, whose bioactive and biocompatible properties can be further evaluated, the most efficient materials could be eventually used in tissue engineering applications. In order to get more insight concerning the structural characteristics of the samples obtained in the present study, X-ray diffraction analysis (XRD), and FT-IR spectroscopy measurements were performed. To assess the silver/copper incorporation into the samples network, UV-Vis absorption spectroscopic measurements were also involved.

EXPERIMENTAL

Formation of Glass

The glass compositions belonging to the $60SiO_2\cdot(32\text{-}x)CaO\cdot8P_2O_5\cdot xCuO$ and $60SiO_2\cdot(32\text{-}y)CaO\cdot8P_2O_5\cdot yAg_2O$ (x, y=0, 0.5 and 2.5 mol%) system were prepared by sol-gel method. The used precursors were tetraethyl orthosilicate (TEOS), triethyl phosphate (TEP), calcium nitrate tetrahydrate ($Ca(NO_3)\cdot4H_2O$), silver nitrate ($AgNO_3$) and $Cu(NO_3)\cdot3H_2O$ hydrolyzed in the presence of nitric acid. The (HNO_3+H_2O)/(TEOS+TEP) molar ratio was constant and equal to 8. Reactants were added consecutively after 1-h intervals, with continuous stirring. The solution (*sol*) was poured into closed containers that were kept at 37°C temperature until gelation (*gel*) was reached (1-2 days depending on the sol composition). The resultant gel was by atmospheric dried in an oven 110^0C for 24 h. Nitrate elimination and material stabilization was carried out at 600^0C/3h. This temperature was determined by differential thermal analysis of the dried gels.

Methods

The XRD analysis was carried out on a Shimadzu XRD- 6000 diffractometer using CuKα radiation (λ=1.54), with Ni-filter. The diffractograms were recorded in 2θ range from10° to 80° with a speed of 2°/min.

The FT-IR absorption spectra were recorded with a JASCO 4100 (Jasco, Tokyo, Japan) spectrometer, at room temperature, in the 400–4000 cm^{-1} spectral range with a spectral resolution of 4 cm^{-1} and by using the well-known KBr pellet technique.

UV–Vis Spectroscopy absorption measurements were performed with an Analytic Jena Specord 250 plus UV-Vis spectrometer. The spectral resolution was of 2 nm.

RESULTS AND DISCUSSION

Structural characterization

The XRD patterns of the as-prepared powders is presented in Fig. 1 and revealed broad characteristics recorded around 2Θ~22° that denoted the preponderantly amorphous character of the samples. The irregular shape of the XRD signals obtained from the thermally treated samples can be owed to the presence of the second signal centered at 2θ~32° that shows the possible existence of a few crystallization centers associated with the formation of tricalcium phosphate phase, identified as $Ca_3(PO_4)_2$ H_2O (Fig. 2)[13].

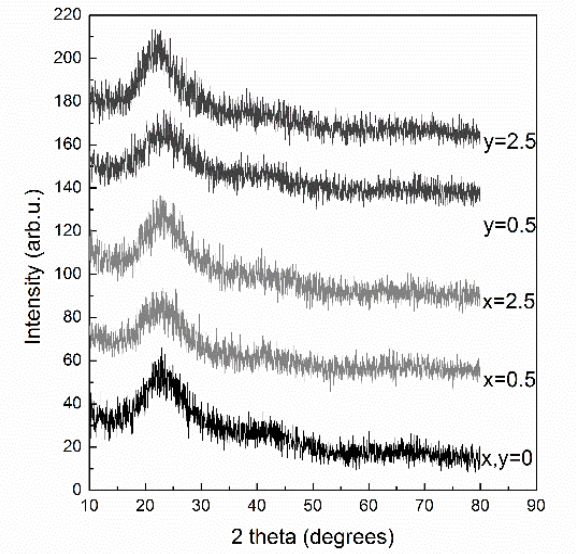

Fig. 1. XRD patterns of the as-prepared samples belonging to the $60SiO_2$·(32-x)CaO·$8P_2O_5$·xCuO and $60SiO_2$·(32-y)CaO·$8P_2O_5$·yAg_2Osystems, with x and y values as indicated.

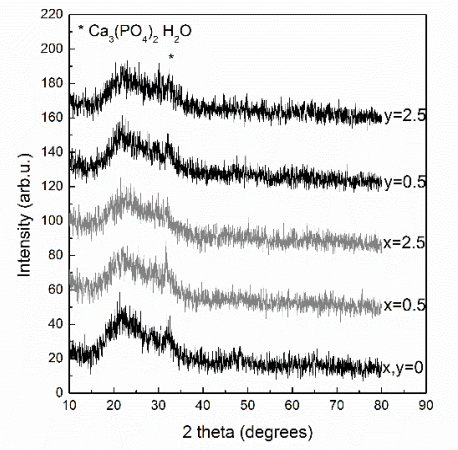

Fig. 2. XRD patterns of the thermally treated samples belonging to the $60SiO_2 \cdot (32\text{-}x)CaO \cdot 8P_2O_5 \cdot xCuO$ and $60SiO_2 \cdot (32\text{-}y)CaO \cdot 8P_2O_5 \cdot yAg_2O$ systems, with x and y values as indicated.

The FT-IR spectra of the heat treated samples exhibit absorption bands characteristic for bioactive glass (Fig. 3).Thereby, one can see features that can be assigned to the Si-O-Si stretching (1040 and 860 cm^{-1}) and Si-O-Si bending vibrations (510 cm^{-1}). The presence of water is indicated by the wide absorption signal at around 1640 cm^{-1}. The band at 1440 cm^{-1} is associated with the existence of the carbonate group and the 560 and 580 cm^{-1} signals show the presence of the phosphate groups [13]. By inspecting the recorded FTIR spectra no significant changes can be noticed, this result indicated that no important structural changes occurred in the glass structure with the addition of silver or copper, as expected for their low content.

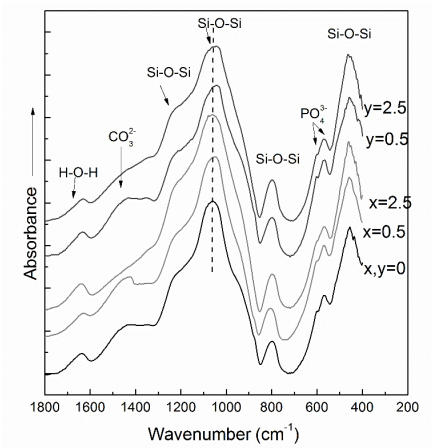

Fig. 3. FT-IR spectra of the thermally treated samples belonging to the $60SiO_2 \cdot (32\text{-}x)CaO \cdot 8P_2O_5 \cdot xCuO$ and $60SiO_2 \cdot (32\text{-}y)CaO \cdot 8P_2O_5 \cdot yAg_2O$systems, with x and y values as indicated.

In order to get more details about the structure of the investigated bioactive glasses, UV-vis absorption measurements were performed. UV-vis spectrum of the sample with 2.5 mol% CuO (Fig. 4a) shows a band centered at 800 nm characteristic to d-d transitions of Cu^{2+} in octahedral coordination [14]. According to the literature, the samples containing silver could give rise to plasmon resonance bands in the 400-500 nm spectral region of the UV-vis spectra as a consequence of Ag nanoparticles presence [10]. Thus, by analyzing the Figure 4b one can observe the appearance of an absorption signal with a maximum of around 420 nm for the samples with silver, this signal being associated with the existence of very small, spherical silver particles, formed inside the glass matrix [10]. For the glass sample with 2.5 mol% Ag_2O content, a less intense signal appears between 300 and 330 nm due to electronic transitions in Ag metallic species [15].

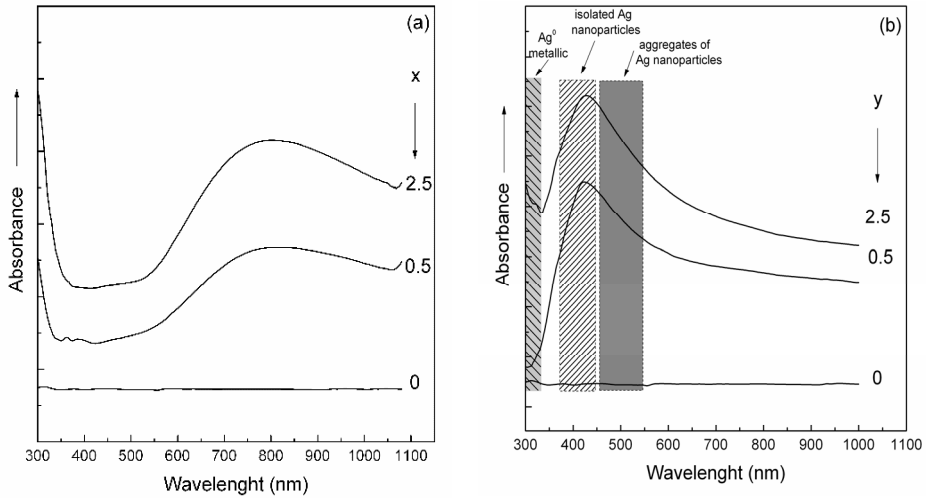

Fig. 4. UV-vis spectra of the (a) $60SiO_2 \cdot (32\text{-}x)CaO \cdot 8P_2O_5 \cdot xCuO$ (b) $60SiO_2 \cdot (32\text{-}y)CaO \cdot 8P_2O_5 \cdot yAg_2O$ samples with x and y values as indicated

CONCLUSIONS

In this study several compositions of silver and copper oxides containing bioactive SiO_2–CaO–P_2O_5 based glasses were synthesized. The structural particularities determined after the silver or copper addition to the bioactive glass network was investigated by three different techniques. The XRD pattern of the as prepared samples revealed the amorphous structure of the glass. Thermally treatment applied to the both set of samples revealed the occurrence of a second broad maximum centered at $2\theta \sim 32°$ that show the possible existence of a few crystallization centers associated with the formation of tricalcium phosphate phase. UV-vis absorption spectra indicate the presence of a small amount of metallic silver into the glass matrix, as indicated

by the absorption signal recorded around 420 nm. For 2.5% Cu containing sample, the UV-vis spectra emphasize a band centered at 800 nm characteristic of d-d transitions of Cu^{2+} in octahedral coordination.The FT-IR spectra of the obtained sol-gel glass samples exhibit absorption bands characteristic for bioactive glass, no influence of the silver and copper addition have been noticed.

REFERENCES

1. Vallet-Regi, M., Salinas, A.J., Arcos, D.,*From the bioactive glasses to the star gels.* J Mater Sci Mater Med, 2006. **17**(11): p. 1011-7.
2. Anderson, J.M., *The future of biomedical materials.* J Mater Sci Mater Med, 2006. **17**(11): p. 1025-8.
3. Jeffrey, B.C., and S.G. W., *Sol-Gel Science - The Physics and Chemistry of Sol-Gel Processing.* ACADEMIC PRESS, INC., 1990: p. 2-3.
4. Dutra, Z.E., *The Formation of unusual glasses by sol-gel processing.* Journal of Non-Crystalline Solids, 1992. **147&148**: p. 820-823.
5. Polak, J.M., Bishop, A.E.,*Stem cells and tissue engineering: past, present, and future.* Ann N Y Acad Sci, 2006. **1068**: p. 352-66.
6. Sooraj, H.N., L.M. A., and S.J. D., *A comparative study of CaO-P2O5-SiO2 gels prepared by a sol-gel method.* Materials Chemistry and Physics, 2004. **88**: p. 5-8.
7. Aguiar, H., Solla, E.L., Serra, J., Gonzalez, P., Leon, B., Almeida, B., Cachinho, S., Davim, E.J.C., Correia, R., Oliveira, J.M., Fernandes M.H.V., *Orthophosphate nanostructures in SiO2–P2O5–CaO–Na2O–MgO bioactive glasses.* Journal of Non-Crystalline Solids, 2008. **354**(34): p. 4075-4080.
8. Jones, J.R., Ehrenfried, L.M., Sarevanapavan, P., Hench, L.,*Controlling ion release from bioactive glass foam scaffolds with antibacterial properties.* J Mater Sci Mater Med, 2006. **17**(11): p. 989-96.
9. Di Nunzio, S., Vitale Brovarone, C., Spriano, S., Milanese, D., Verne, E., Bergo, V., Maina, G., Spinelli, P., *Silver containing bioactive glasses prepared by molten salt ion-exchange.* Journal of the European Ceramic Society, 2004. **24**: p. 2935-2942.
10. Magyari, K., Stefan, R., Vodnar, D.C., Vulpoi A., Baia, L.,*The silver influence on the structure and antibacterial properties of the bioactive 10B2O3−30Na2O−60P2O2 glass.* Journal of Non-Crystalline Solids, 2014. **402**: p. 182-186.
11. Erol, M.M., Mourino, V., Newby, P., Chatzistavrou, X., Roether, J.A., Hupa, L., Boccaccini, A.R.,*Copper-releasing, boron-containing bioactive glass-based scaffolds coated with alginate for bone tissue engineering.* Acta Biomater, 2012. **8**(2): p. 792-801.
12. Wu, C., Zhou, Y., Xu, M., Han, P., Chen, L., Chang, J., Xiao, Y.,*Copper-containing mesoporous bioactive glass scaffolds with multifunctional properties of angiogenesis capacity, osteostimulation and antibacterial activity.* Biomaterials, 2013. **34**(2): p. 422-33.
13. Magyari, K., Baia, L., Vulpoi, A., Simon, S., Popescu, O., Simon, V.,*Bioactivity evolution of the surface functionalized bioactive glasses.* J Biomed Mater Res B Appl Biomater, 2014.
14. Bonici, A., Lusvardi, G., Malavasi, G., Menabue, L., Piva, A., *Synthesis and characterization of bioactive glasses functionalized with Cu nanoparticles and organic molecules.* Journal of the European Ceramic Society, 2012. **32**(11): p. 2777-2783.
15. Baia, L., Muresan, D., Baia, M., Popp, J., Simon, S., *Structural properties of silver nanoclusters–phosphate glass composites.* Vibrational Spectroscopy, 2007. **43**(2): p. 313-318.

STUDIA UBB PHYSICA, Vol. 60 (LX), 1, 2015, pp. 109-118
(RECOMMENDED CITATION)

Dedicated to Academician Professor Dr. Emil Burzo on His 80th Anniversary

CW EPR POWDER SIMULATIONS USING SPIRAL-TYPE GRIDS

C. CRĂCIUN[1*]

ABSTRACT. This paper compares two types of spiral grids from the point of view of their homogeneity and efficiency for CW EPR powder simulations. One grid is well-known in the EPR context and has a parameter-free analytical expression. The other grid has been defined for minimizing the potential energy of charged particles on the unit sphere and has an adjustable shape. The quality of EPR simulations produced by these spiral grids is analysed for a spin system S = 1/2, with different symmetry of the gyromagnetic matrix.

Keywords: *CW EPR, simulation, spiral grid*

INTRODUCTION

CW EPR powder spectra are calculated as a sum over the spectral contribution of all single-crystals composing the powder sample [1]. The single-crystals' orientations in the laboratory frame may be modelled using a spherical grid. The quality of EPR simulations depends on the orientational grid's type and size. Higher dimensional grids yield better simulated spectra, but they are time expensive for powder EPR simulations. Therefore, the grids with good EPR behaviour even at low size are preferred.

Different grids have been previously used for simulation of magnetic resonance spectra [1-13]. This paper analyses the homogeneity characteristics and the EPR behaviour of two spiral-type grids. The first spiral grid (MW) was proposed by Mombourquette and Weil in the context of EPR simulations [7]. This grid has a C_i symmetry [10], a high convergence rate in simulations [1], and a high homogeneity degree [10]. The second spiral grid (RSZ), known as the "generalised spiral", was proposed by Rakhmanov, Saff, and Zhou [14]. This grid was defined for minimizing the energy of a set of charged

[1] *Babeş-Bolyai University, Faculty of Physics, 1 Kogălniceanu str., 400084 Cluj-Napoca, Romania*
* *Corresponding author e-mail: cora.craciun@phys.ubbcluj.ro*

particles on the unit sphere, which interact through the logarithmic potential $V(r) = \log(1/r)$ [14]. The shape of the RSZ grid may be adjusted by means of a parameter in the grid's analytical expression. To the author's knowledge, the RSZ grid has not been previously used for EPR simulations.

This paper is structured as follows. Next section presents theoretical details about the two spiral grids and about CW EPR powder simulations. The grids' homogeneity degree and their EPR efficiency are compared in the Results and discussion section. The final section summarizes current work.

THEORETICAL AND COMPUTATIONAL DETAILS

1. The MW spiral grid

The MW grid (Fig. 1 f) consists in a single spiral which connects the poles of the unit sphere or an equator point and a pole [7]. At its proposal, the MW grid was generated with an optimization procedure, which ensured that the consecutive grid points on the spiral were equally-spaced [7]. Later, the grid was generated analytically and has the following expressions in spherical coordinates, on the full unit sphere [1,10]:

$$\theta_k = \arccos(h_k), \quad \phi_k = \Delta \arcsin(h_k), \tag{1}$$

$$\Delta = \sqrt{\pi(N-1)}, \quad h_k = \frac{2k}{N-1} - 1, \quad 0 \le k \le N-1.$$

Unlike the RSZ spiral grid, the MW grid has a fixed shape, at a given grid size *N*.

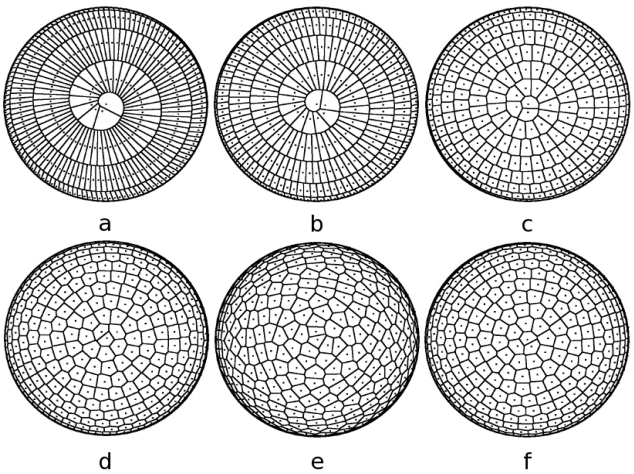

Fig. 1. The upper hemisphere of the MW spiral grid (f) and of the RSZ spiral grids with the following parameter *C*: (a) 1.2, (b) 1.6, (c) 2.6, (d) 3.4, and (e) 4.6. All grids have 578 points on the full unit sphere.

2. The RSZ spiral grid

The RSZ spiral grid in spherical coordinates is [14]

$$\theta_k = \arccos(h_k), \quad h_k = \frac{2(k-1)}{N-1} - 1, \quad 1 \le k \le N, \tag{2}$$
$$\phi_k = \left(\phi_{k-1} + C / \sqrt{N(1-h_k^2)}\right) (\mathrm{mod}\ 2\pi), \quad 2 \le k \le N-1, \quad \phi_1 = \phi_N = 0,$$

where N is the grid size, C is a parameter, and *mod* stands for the modulo operation. The best packing of the grid points on the unit sphere (the Tammes problem) was obtained with the parameter value $C = \left(8\pi / \sqrt{3}\right)^{1/2} \approx 3.809$ [15,16]. In the energy minimization context, however, the optimal value $C = 3.6$ was obtained by experimentation [14,16]. In this paper, the C parameter is varied between 1.0 and 4.8 with step 0.2, to obtain different RSZ grids for EPR simulations (Fig. 1 a-e).

The Voronoi diagrams of the spiral grids presented in Fig. 1 have been computed with the STRIPACK package (R.J. Renka) [17], in the implementation available at [18].

3. CW EPR powder simulations

CW EPR powder spectra for the spiral grids are compared for a spin system $S = 1/2$, characterised by electron Zeeman interaction with the static magnetic field. For this spin system, the simulated powder spectra have the following analytical form [19]:

$$S(B) \approx \sum_{k=1}^{N} w_k I_k F[B - B_0(\Omega_k), \Gamma] = \sum_{k=1}^{N} C_B w_k \frac{\langle g_1^2(\Omega_k) \rangle}{g(\Omega_k)} F[B - B_0(\Omega_k), \Gamma], \tag{3}$$

where $\Omega_k = (\theta_k, \phi_k)$ is the orientation of the static magnetic field in the molecular frame of the gyromagnetic matrix **g**, I_k is the linear spectral intensity at orientation Ω_k, $F[B - B_0(\Omega_k), \Gamma]$ is the line shape absorption function, centred at the resonance magnetic field B_0 and having the peak-to-peak line width Γ in the first derivative, w_k is the weighting factor, C_B is a constant, $g(\Omega_k)$ is the effective gyromagnetic value, and $\langle g_1^2(\Omega_k) \rangle$ is [19]:

$$\begin{aligned} \langle g_1^2(\Omega_k) \rangle = \big(g_x^2 g_y^2 (\sin\theta_k)^2 + g_y^2 g_z^2 \left[(\sin\phi_k)^2 + (\cos\theta_k \cos\phi_k)^2\right] + \\ + g_x^2 g_z^2 \left[(\cos\phi_k)^2 + (\cos\theta_k \sin\phi_k)^2\right]\big) / 2g^2(\Omega_k), \end{aligned} \tag{4}$$

with g_x, g_y, and g_z the principal values of the **g** matrix.

RESULTS AND DISCUSSION

1. The spiral grids' homogeneity

The weighting factor w_k in the CW EPR powder spectrum (formula 3) may be approximated with the area of the Voronoi cell corresponding to the k^{th} grid point. Therefore, the relative standard deviation of the m distribution of the Voronoi cells' areas A_k, for $1 \le k \le N$, has been chosen for comparing the grids' homogeneity [10]:

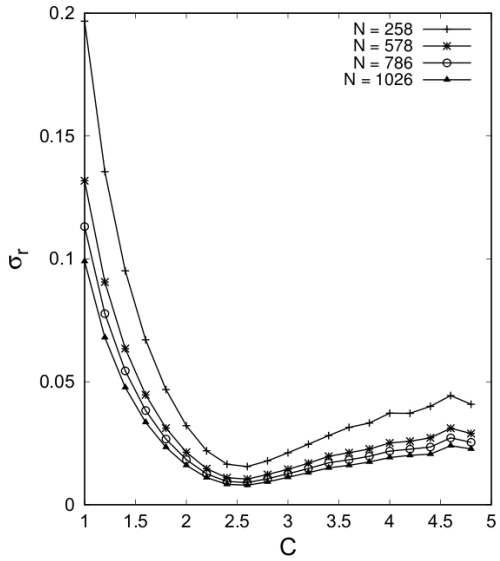

Fig. 2. Dependence of the σ_r homogeneity metric on the RSZ grid's parameter *C*, for different grid sizes *N*.

Table 1. The σ_r homogeneity metric for the RSZ (*C* = 2.6 and *C* = 3.4) and MW spiral grids, at different grid sizes *N*

N	σ_r (RSZ, *C* = 2.6)	σ_r (RSZ, *C* = 3.4)	σ_r (MW)
258	0.016	0.028	0.030
578	0.011	0.020	0.020
786	0.009	0.017	0.017
1026	0.008	0.015	0.015

$$\sigma_r = \sqrt{\frac{N}{16\pi^2}\sum_{k=1}^{N} A_k^2 - 1} \tag{5}$$

Table 2. Principal values of the **g** matrix used in EPR simulations. The symmetry of the **g** matrix (I - isotropic, A - axial, R - rhombic) is indicated in parenthesis in each case.

No.	g_x, g_y, g_z	No.	g_x, g_y, g_z	No.	g_x, g_y, g_z
1	2.0, 2.0, 2.0 (I)	10	2.1, 2.0, 2.0 (A)	19	2.2, 2.0, 2.0 (A)
2	2.0, 2.0, 2.1 (A)	11	2.1, 2.0, 2.1 (A)	20	2.2, 2.0, 2.1 (R)
3	2.0, 2.0, 2.2 (A)	12	2.1, 2.0, 2.2 (R)	21	2.2, 2.0, 2.2 (A)
4	2.0, 2.1, 2.0 (A)	13	2.1, 2.1, 2.0 (A)	22	2.2, 2.1, 2.0 (R)
5	2.0, 2.1, 2.1 (A)	14	2.1, 2.1, 2.1 (I)	23	2.2, 2.1, 2.1 (A)
6	2.0, 2.1, 2.2 (R)	15	2.1, 2.1, 2.2 (A)	24	2.2, 2.1, 2.2 (A)
7	2.0, 2.2, 2.0 (A)	16	2.1, 2.2, 2.0 (R)	25	2.2, 2.2, 2.0 (A)
8	2.0, 2.2, 2.1 (R)	17	2.1, 2.2, 2.1 (A)	26	2.2, 2.2, 2.1 (A)
9	2.0, 2.2, 2.2 (A)	18	2.1, 2.2, 2.2 (A)	27	2.2, 2.2, 2.2 (I)

The grids with smaller σ_r values are more homogeneous [10]. In case of RSZ spiral grids, the σ_r homogeneity metric presents a minimum when the grids' parameter *C* is about 2.6 (Fig. 2). At the same grid size, the RSZ grid has similar homogeneity with the MW grid when its parameter is $C \approx 3.4$ (Table 1). This *C* value is close to the 3.6 value determined from energy minimization considerations [16].

2. Simulated CW EPR powder spectra

Simulated spectra for the spiral grids with 578 points on the full unit sphere are compared with those of the MW grid with 9606 points, chosen as reference. The spin system considered is S = 1/2 and its **g** matrix is isotropic, axial, or rhombic (Table 2). The axial **g** matrices used in simulations have the x, y, or z orthogonal axis. The spiral grids given in formulas (1) and (2) are built around the z axis of the reference system. This z axis will be called in the following the main axis of the spiral grids.

Four simulation cases, two for axial and two for rhombic **g** matrices (Fig. 3), are discussed in the following. In Fig. 4 are given difference spectra obtained by subtracting the reference spectra, $S_0(B)$ (Fig. 3 g), from the spiral grids' spectra, $S(B)$ (Fig. 3 a-f):

$$d(B_j) = S(B_j) - S_0(B_j), \quad 1 \le j \le M, \tag{6}$$

where B_j are the equally-spaced magnetic fields at which the spectral intensity has been calculated. In the four simulation cases considered, the RSZ grid with *C* = 1.6 generates low-noise simulated spectra (Fig. 3 b), but there is a residual contribution along the g_z direction in its difference spectra (Fig. 4 b).

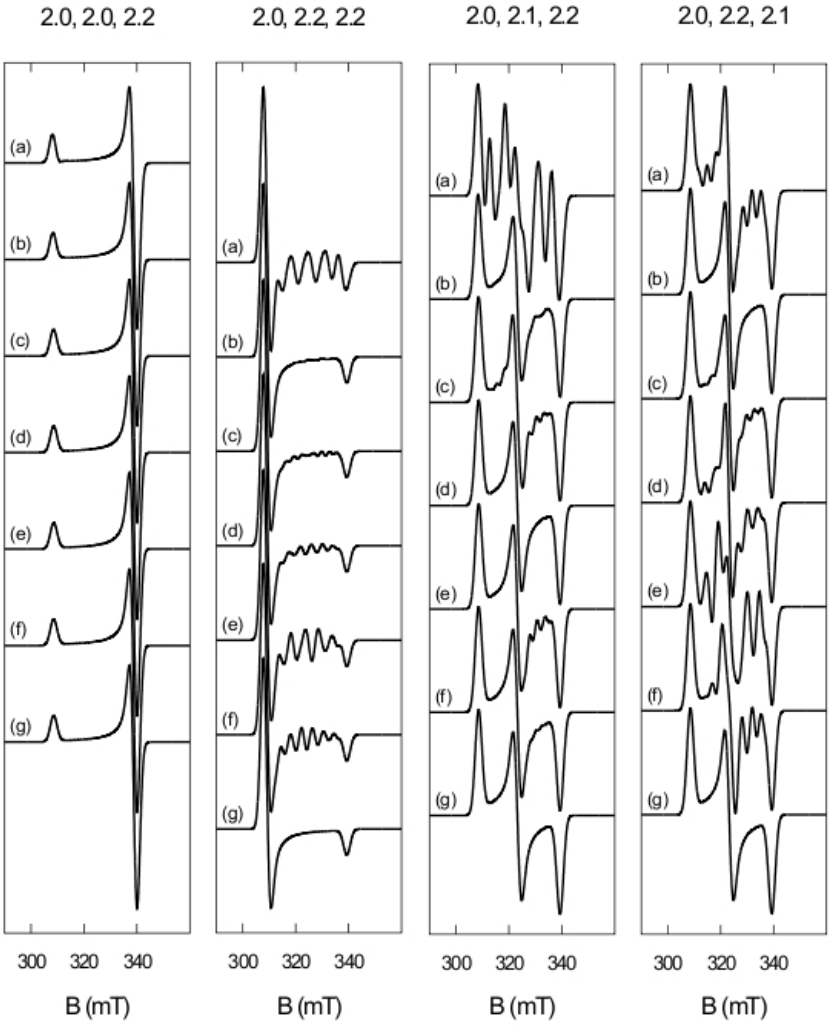

Fig. 3. Simulated CW EPR powder spectra (a-e) for the RSZ spiral grids with 578 points and the following *C* parameter: (a) 1.2, (b) 1.6, (c) 2.6, (d) 3.4, and (e) 4.6, (f) for the MW spiral grid with 578 points, and (g) for the reference MW grid with 9606 points. Principal values of the **g** matrix, g_x, g_y, and g_z, are indicated above each figure. Simulation parameters: microwave frequency ν = 9.5 GHz, full width at half maximum of the Gaussian line shape of 3 mT.

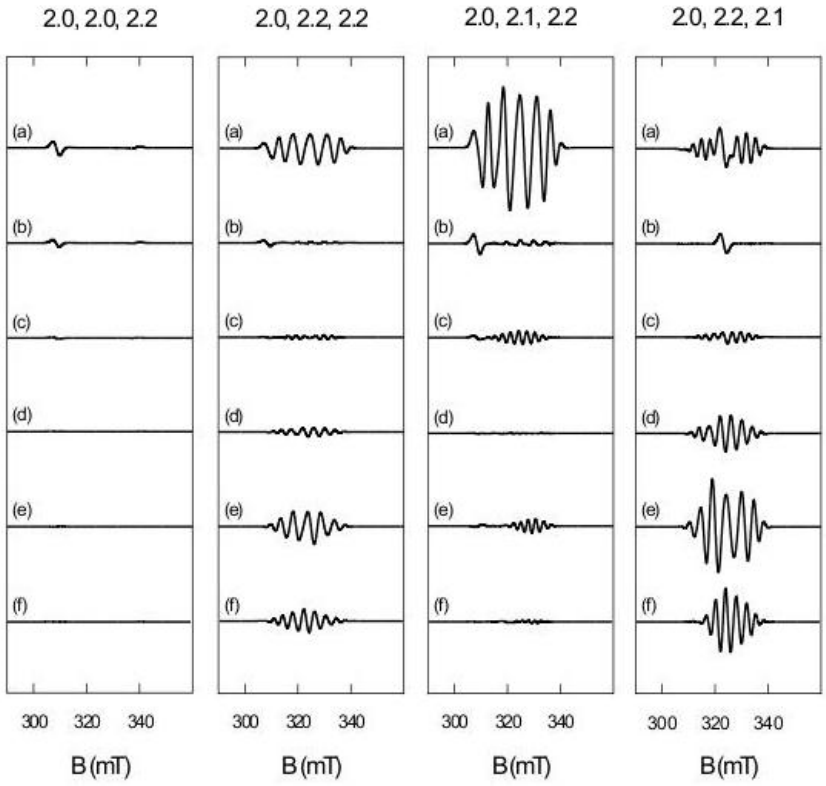

Fig. 4. Difference between the simulated spectra of the spiral grids with 578 points (Fig. 3 a-f) and the corresponding simulated spectra of the MW grid with 9606 points (Fig. 3 g), for the same **g** matrix.

i. $g_x = g_y = 2.0$, $g_z = 2.2$: For all values of the *C* parameter, the RSZ grids generate low-noise simulated spectra. The MW spiral grid (Fig. 3 f) and the RSZ grids with $C = 3.4$ and $C = 4.6$ (Fig. 3 d,e) have nearly the same simulated spectra as the reference grid (Fig. 3 g). This behaviour may be explained by two reasons: (1) the RSZ grids' high homogeneity degree (small σ_r values) for the two *C* values (Fig. 2) and (2) the coincidence between the RSZ grids' main axis and the **g** matrix axial axis.
ii. $g_x = 2.0$, $g_y = g_z = 2.2$: In this axial case, the grids' main axis (z) and the **g** matrix axial axis (x) do not coincide. The RSZ grids with $C = 1.6$, 2.6, and 3.4 (Fig. 3 and Fig. 4 b-d) have close EPR behaviour to the reference grid. One reason may be the high homogeneity degree of these RSZ grids (Fig. 2). However, the RSZ grid with $C = 4.6$ and the MW grid with 578 points are also homogeneous, but their simulated spectra (Fig. 3 e,f) are quite noisy.

iii. g_x = 2.0, g_y = 2.1, g_z = 2.2: For this rhombic case, the RSZ grid with C = 3.4 (Fig. 3 d) and the MW grid (Fig. 3 f) are the closest in EPR simulations to the reference grid (Fig. 3 g). The RSZ grid with C = 1.2 generates a very noisy EPR spectrum (Fig. 3 a) and it also has a low homogeneity degree (Fig. 2).

iv. g_x = 2.0, g_y = 2.2, g_z = 2.1: The spiral grids' difference spectra with respect to the reference spectrum (Fig. 4) resemble those from case (ii) discussed above. However, now the residual contribution in difference spectra is higher for the MW grid (Fig. 4 f) and for the RSZ grids with C = 3.4 and C = 4.6 (Fig. 4 d,e) than in the (ii) case. The ordering relation $g_y > g_z$ may be a possible reason.

As has been emphasised in reference [1], the MW spiral grid is more efficient in EPR simulations when its principal axes coincide with those of the dominant anisotropic interaction of the spin system. This is also true for the RSZ grids. If an RSZ grid built around the z axis of the reference system yields a noisy simulated EPR spectrum, then the grid built around the x or y axes may enhance the spectrum's quality. For example, the axial cases (9) and (25) in Table 2 have the same principal values of the

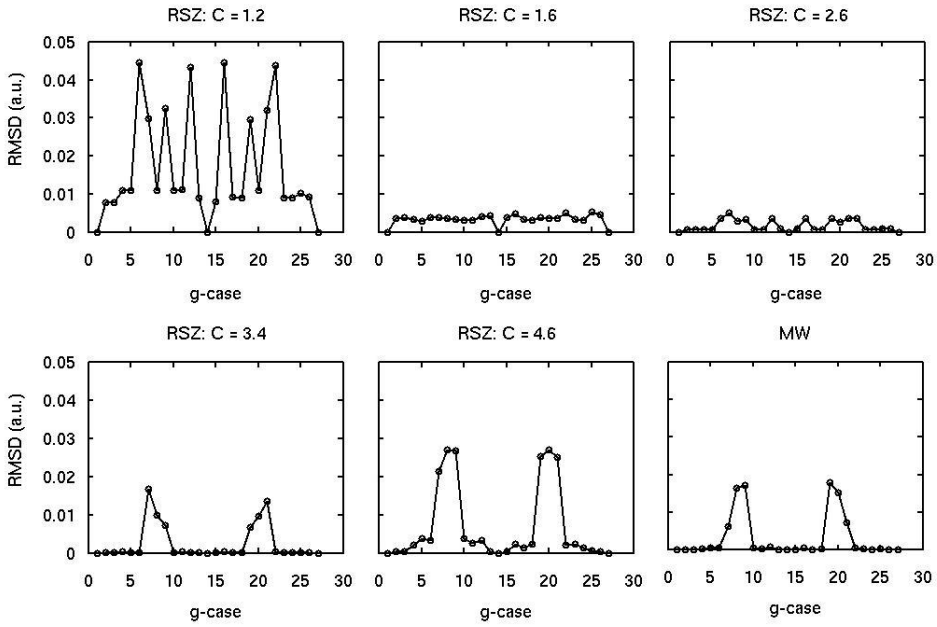

Fig. 5. The *RMSD* metric for the set of g-cases given in Table 2. The first five figures belong to the RSZ grids, with indicated C parameter, and the last figure belongs to the MW grid.

g matrix, but the g_x and g_z values are swapped. If the RSZ grid with C = 3.4 is built around the z axis, then the simulated spectrum in case (9) is noisy and that in case (25) is noise-free. Thus, using in case (9) an RSZ grid with the main axis x will produce a noise-free spectrum. A similar situation occurs in cases (8) (noisy) and (22) (noise-free), for the same RSZ grid with C = 3.4 and the main axis z.

The root-mean-square deviation (*RMSD*) was calculated between the simulated spectra of the spiral grids (578 points) and the corresponding simulated spectra of the reference MW grid (9606 points), for the g-cases given in Table 2. According to the *RMSD* metric, the simulated spectra for the RSZ grid with C = 1.2 differ the most from those of the reference grid in the rhombic g-cases (6), (12), (16), and (22), and in the axial g-cases (7), (9), (19), and (21) (Fig. 5, Table 2). For the RSZ grids with C = 1.6 and C = 2.6, *RMSD* is relatively small for all g-cases. The RSZ grids with C = 3.4 and C = 4.6 differ the most from the reference grid in the following g-cases: (7), (8), and (9), with maximal g_y value, and (19), (20), and (21), with maximal g_x value. The MW grid and the RSZ grid with C = 3.4 have close EPR behaviour for all **g** matrices considered.

CONCLUSIONS

This paper has compared the homogeneity degree and the behaviour in CW EPR powder simulations of two spiral-type grids: the grid proposed by Mombourquette and Weil (MW) and that proposed by Rakhmanov, Saff, and Zhou (RSZ). The RSZ spiral grid was generated in different variants, by means of an adjustable parameter C appearing in its analytical expression. The RSZ grid with C = 3.4 has similar characteristics with the MW grid; the RSZ grid with C = 2.6 is the most homogeneous concerning the distribution of its Voronoi cells' area; and the grids with C = 1.6, 2.6, and 3.4 generate relatively low-noise CW EPR powder spectra, for different symmetries of the gyromagnetic matrix.

REFERENCES

1. A. Ponti, *J. Magn. Reson.*, 138, 288 (1999).
2. M.J. Nilges, Ph.D. Thesis, University of Illinois, Urbana, Illinois, 1979.
3. S. Galindo, L. Gonzáles-Tovany, *J. Magn. Reson.*, 44, 250 (1981).
4. D.W. Alderman, M.S. Solum, D.M. Grant, *J. Chem. Phys.*, 84, 3717 (1986).
5. M.C.M. Gribnau, J.L.C. van Tits, E.J. Reijerse, *J. Magn. Reson.*, 90, 474 (1990).
6. A. Kreiter, J. Hüttermann, *J. Magn. Reson.*, 93, 12 (1991).
7. M.J. Mombourquette, J.A. Weil, *J. Magn. Reson.*, 99, 37 (1992).
8. D. Wang, G.R. Hanson, *J. Magn. Reson. A*, 117, 1 (1995).

9. M. Bak, N.C. Nielsen, *J. Magn. Reson.*, 125, 181 (1997).
10. S. Stoll, Ph.D. Thesis, ETH Zurich, Switzerland, 2003.
11. S. Stoll, A. Schweiger, *J. Magn. Reson.*, 178, 42 (2006).
12. C. Crăciun, *Appl. Magn. Reson.*, 38, 279 (2010).
13. C. Crăciun, *J. Magn. Reson.*, 245, 63 (2014).
14. E.A. Rakhmanov, E.B. Saff, Y.M. Zhou, *Math. Res. Letters*, 1, 647 (1994).
15. W. Habicht, B.L. van der Waerden, *Math. Ann.*, 123, 223 (1951).
16. E.B. Saff, A.B.J. Kuijlaars, *Math. Intell.*, 19, 5 (1997).
17. R.J. Renka, *ACM Trans. Math. Softw.*, 23, 416 (1997).
18. http://people.sc.fsu.edu/~jburkardt/f_src/f_src.html.
19. J.R. Pilbrow, "Transition Ion Electron Paramagnetic Resonance", Clarendon Press, Oxford, **1990**, pp. 222-229.